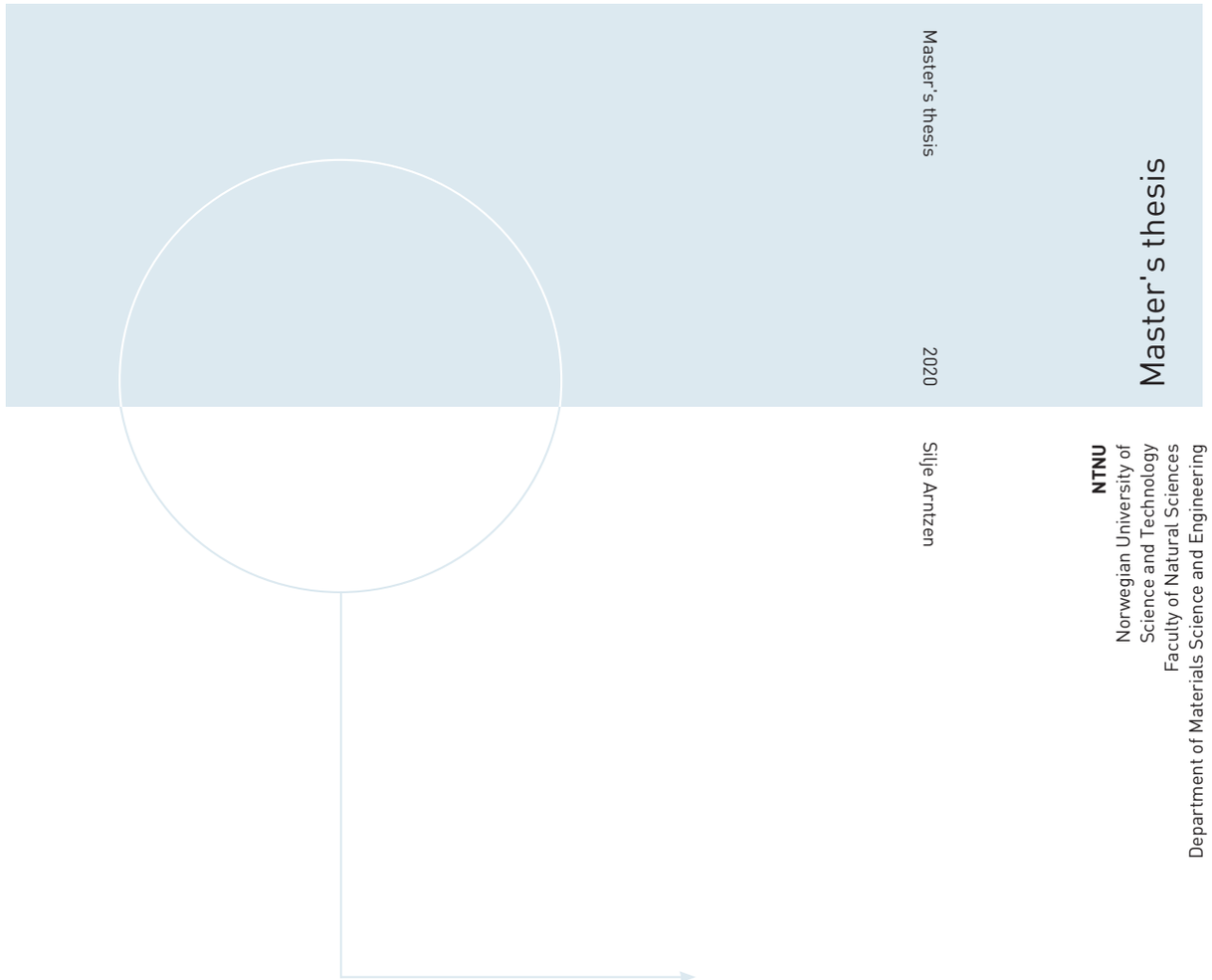

Master's thesis

2020

Silje Arntzen

NTNU
Norwegian University of
Science and Technology
Faculty of Natural Sciences
Department of Materials Science and Engineering

Silje Arntzen

Ductility investigation of extruded profiles in an AA6063 alloy

June 2020

NTNU
Norwegian University of
Science and Technology

NTNU
Norwegian University of
Science and Technology

NTNU

Norwegian University of
Science and Technology

Ductility investigation of extruded profiles in an AA6063 alloy

Silje Arntzen

Materials Science and Engineering
Submission date: June 2020
Supervisor: Bjørn Holmedal

Norwegian University of Science and Technology
Department of Materials Science and Engineering

Preface

This report is submitted to the Norwegian University of Science and Technology (NTNU) and is the final part of a Master of Science degree at the Department of Materials Science and Engineering. The research has been conducted at the Department of Materials Science and Engineering during the spring of 2020, and is a continuation of the author's project thesis from the autumn of 2019.

The work is performed in collaboration with Hydro Extruded Solutions, and the extruded profiles are provided by Hydro Extruded Solutions Tønder, Denmark. The aim of this collaboration is to investigate the ductility of one of their extruded profiles.

I would like to thank my supervisor Professor Bjørn Holmedal for his competent and patient supervision. I would also thank Chief Engineer Pål Christian Skaret for his help with machining and cutting of samples, set up and execution of experiments. Laboratory engineer Berit Vinje Kramer also deserve a thank you for helping and answering questions regarding laboratory work and sample preparation.

Finally, I would like to thank my family and friends for their support, and my fellow students for five nice years in Trondheim.

Abstract

In the automotive industry the demand for lighter, stronger and cost-efficient materials in turns of production and processing of parts is increasing. This demands more knowledge of the material's mechanical properties like strength and ductility. In this thesis the ductility of a widely used alloy in the automotive industry is studied, namely an extruded AA6063 profile. Ductility is not a very specific term and can be used in a wide perspective. In this context ductility is measured through tensile testing, where flow instability will take place in the neck and lead to diffuse and local necking.

The texture of the profile is characterized through electron backscatter diffraction in as-received condition, and tensile specimens are made and solution heat treated before testing. The specimens are water- and air quenched from the heat treatment. Half of the water- and air quenched specimens are also pre stretched 0.5% strain right after quenching. Then the specimens are tensile tested after 24 hours and 7 days at room temperature. The fracture surface is investigated in electron scanning microscope and in energy-dispersive X-ray spectroscopy.

In stress-strain curves, the cooling rate and storage time only affected the ultimate stress, and apparently have little effect on the elongation to fracture. Fracture areal measured fracture strain coincides with the observations of elongation to fracture.

The 0.5% pre stretching creates a distinct shape of the true stress-strain curve up to 0.3% true strain. The pre stretched specimens are observed to have a longer and steeper part in the beginning of the testing compared to the not stretched specimens. The ultimate stress of the pre stretched specimens are observed to be lower than in the not stretched specimens.

Investigation of the fracture surface reveals dimples and constituent particles indicating that the working fracture mechanism is nucleation, growth and coalescence of voids. Literature also indicating that the constituent particles are a major factor influencing the strain to fracture.

In March of 2020 NTNU closed due to the coronavirus, and all the ongoing experimental work had to be aborted. As a consequence, this report will contain a literature study and larger emphasis is placed on the results of previous studies.

Sammendrag

I bilindustrien jobbes det konstant mot å finne lettere, sterkere og mer kostnadseffektive materialer til produksjon og prosessering av bildeler. Dette fører til et større krav om kunnskap til materialenes mekaniske egenskaper, som styrke og duktilitet. I denne avhandlingen er duktiliteten til en mye brukt legering i bilindustrien undersøkt, nemlig en ekstrudert AA6063 legering. Duktilitet er et veldig bredt begrep og brukes om mye. I denne sammenheng brukes duktilitet i strekk testing, hvor det oppstår flyt instabilitet i "necken" som først fører til diffus necking og deretter til lokal necking.

Teksturen til profilen er karakterisert i electron backscatter diffraction, og strekkstavene er laget før de så varmebehandles. Strekkstavene er vann- og luft kjølt fra varmebehandlingen. Halvparten av de vann- og luft bråkjølte strekkstavene er for-stukket 0,5% tøyning rett etter kjøling. Etter dette er stavene lagret i romtemperatur før de strekkes etter henholdsvis 24 timer og 7 dager. Bruddflaten er undersøkt i elektronmikroskop og energy-dispersive X-ray spectroscopy.

Spenning-tøynings kurvene viser at kjølingen og lagring bare påvirker den maksimale spenningen, og ser ut til å ha liten effekt på bruddforlengelsen. Målt areal fraksjon basert bruddtøyning stemmer med tidligere observasjoner at duktiliteten er lite påvirket av kjølehastighet og lagringstid.

Ved å strekke 0,5% får spenning-tøynings kurven en spesiell form opp til 0,3% sann tøyning. De før-strekte spenning-tøynings kurvene er observert til å ha lengre og bratt stigning i starten sammenlignet med de som ikke er før-strukket, men den maksimale spenningen til de før-strekte strekkstavene er lavere enn de strekkstavene som ikke er før-strukket.

Undersøkelser av bruddflaten avslører dimpler og intermetalliske partikler, og dette indikerer at bruddmekanismen er nukleasjon, vekst og sammenvoksing av små tomrom. Litteraturen indikerer også at de intermetalliske partiklene er en stor faktor som påvirker bruddtøyningen.

I mars 2020 stengte NTNU på grunn av koronavirus, og alle pågående ekperimenter ble dermed avbrutt. Som en konsekvens vil rapporten inneholde et litteratur studie og tidligere resultater vil vektlegges mer.

Contents

1. Introduction

Aluminium exhibits properties like good formability and corrosion resistance, combined with a high load-bearing capacity and potential for recycling. This makes aluminium appealing to automotive and offshore industry. The potential of using aluminium in cars are shown in Figure 1.1a and 1.1b. According to European Aluminium the amount of aluminium in cars have tripled in weight from 50kg in 1990 to 151kg today, and experts have estimated that the amount aluminium can be 196kg in 2025[1].

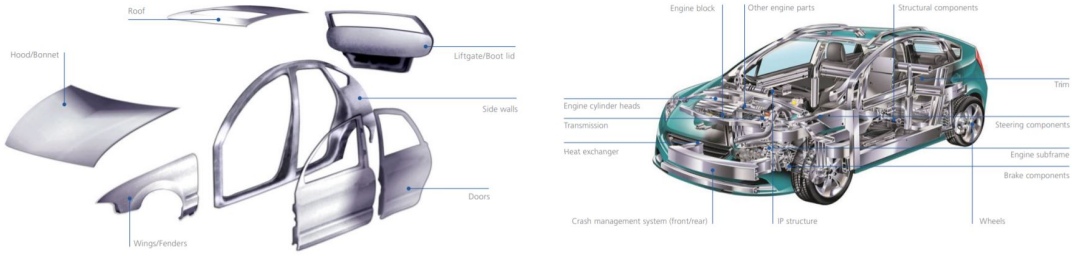

(a) (b)

Figure 1.1: Potential of using aluminium in cars are shown in (a) exterior part and (b) structural parts, from [12]

When the aluminium content in cars increase, components previously made in steel will be made in aluminium. Aluminium differs from steel in mechanical properties and response to heat treatments and forming processes. For this reason, new designs and production methods must be developed in order to switch to aluminium. The forming processes to finalize the automotive parts demand high ductility of the aluminium. The subject of this report is an extruded AA6063 profile used in the automotive industry. The extruded profile is deformed in T4 condition as a part of the forming process, which place a high demand on the ductility of the material. In this specific case the formed profiles are placed on the right and left side of the car engine, and the engine is attached to these profiles. The profiles undergo a powerful bending process in the finalizing steps before mounting in the vehicle. Because of the forming process and safety features associated with the vehicle design, the demand to ductility in T4 is high. Ductility is a diverse term, and in this context, the tensile ductility and elongation to fracture is important.

Few studies are conducted regarding elongation to fracture of an extruded AA6063 profile. The studies are conducted on flat profiles. The mentioned extruded AA6063 profile has a more complex geometrical shape, and very limited experimental work is performed on this profile. The aim of this work is to investigate the local fracture and elongation to fracture.

In March of 2020 NTNU closed due to the coronavirus, and all the ongoing experimental work had to be aborted. As a consequence, this report will be more theory based, with a literature study. The discussion part will partly be based on some of the results from the author's project thesis and the literature study to make up for the lack in experimental results in some areas. Because of the reuse of results from the author's project thesis a summary of the project thesis will be included.

2. Theory

2.1 Stress and strain

In both Subsection 2.1.1 and 2.1.2 stress and strain are defined for an ideal tensile specimen subjected to uniform strain. The stress tensor will be introduced in Subsection 2.1.3.

2.1.1 Stress

A bar is subjected to an axial tensile load, and strained. A free-body diagram of the bar is shown in Figure 2.1.

Figure 2.1: Free body diagram of an axial tensile load.

From Figure 2.1 the external load P is balanced with $\int \sigma dA$. σ is the normal stress component of the cutting plane and A is the cross-section area of the bar. If the stress is distributed uniformly over the area A, the stress is defined as[15]:

$$\sigma = \frac{P}{A} \tag{2.1}$$

where P is the force and A is the area. The stress defined in Equation 2.1 is the true stress, as the area changes with deformation. The engineering stress is defined as:

$$s = \frac{P}{A_0} \tag{2.2}$$

where P is the force and A_0 is the area before deformation. In the rest of the report σ and s are used for true stress and engineering stress, respectively.

2.1.2 Strain

Strains arise from change in length and thickness of a material. The engineering strain is defined by Equation 2.3.

$$e = \frac{L - L_0}{L_0} \tag{2.3}$$

Equation 2.3 is a simple way to calculate the strain and is used in tensile testing. L_0 is the initial extensometer length, and L is the instantaneous extensometer length. The engineering strain, e, is only "valid" for small strains. The equation is based entirely on the dimensions of the original specimen, but these dimensions will change during a tensile test. To compensate for this true strain can be applied, and the true strain is based on instantaneous gauge length contributions[15]. Further in this report ϵ and e are used for true strain and engineering strain, respectively. The true strain equation is given below

$$\epsilon = \int_{L_0}^{L} \frac{dL}{L} = ln\frac{L}{L_0} \tag{2.4}$$

2.1.3 Stress- and strain tensor

In Equations 2.1-2.4 stress and strain are only defined as one component, but the stress can be divided into nine components acting on one cubic volume element as illustrated in Figure 2.2. The stress state of any internal point of the volume element is given by Equation 2.5.

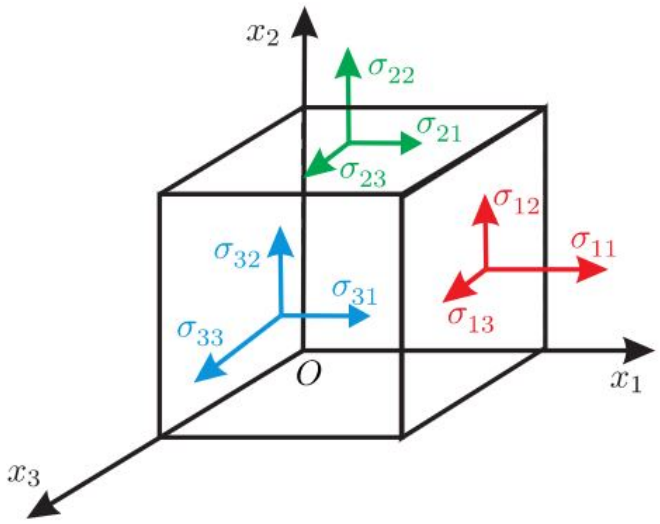

Figure 2.2: Stress components acting on a volume element of material, from [50].

$$\sigma_{ij} = \begin{bmatrix} \sigma_{11} & \sigma_{12} & \sigma_{13} \\ \sigma_{21} & \sigma_{22} & \sigma_{23} \\ \sigma_{31} & \sigma_{32} & \sigma_{33} \end{bmatrix} \tag{2.5}$$

In the stress tensor the first subscript, i, indicates that the stress acts on a plane normal to the x_i axis. The second subscript, j, describes which direction the stress acts. Stresses with two equal subscripts are called normal stresses. The other stresses in the tensor are called shear stresses, and are denoted τ_{ij}. Due to moment balance of the element, $\tau_{ij} = \tau_{ji}$. This gives the tensor in Equation 2.6.

$$\sigma_{ij} = \begin{bmatrix} \sigma_{11} & \tau_{12} & \tau_{13} \\ \tau_{12} & \sigma_{22} & \tau_{23} \\ \tau_{13} & \tau_{23} & \sigma_{33} \end{bmatrix} \tag{2.6}$$

Shear strain

A deformation can result in a change in the angle between two lines. This is called the simple shear strain, and is illustrated in Figure 2.3.

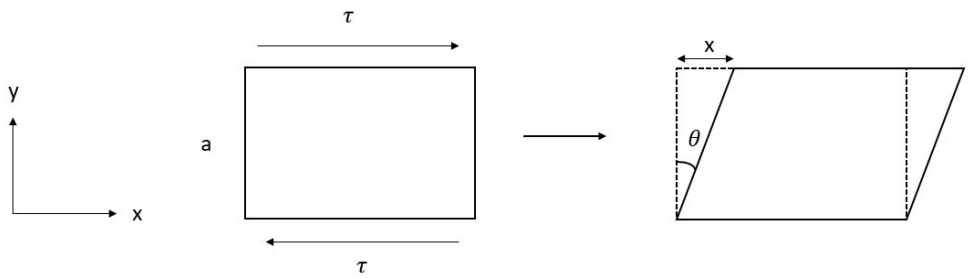

Figure 2.3: Simple shear strain.

The engineering shear strain is defined in Equation 2.7. For small angles θ, the shear strain can be approximated to the angle itself.

$$\gamma = tan\theta = \frac{x}{a} \approx \theta \tag{2.7}$$

The engineering strain is not symmetrical and a pure rotation will be counted as a strain according to Equation 2.7. This makes the engineering strain a less optimal measurement for deformation. The true shear strain on the other hand, is symmetrical and a pure rotation will be ignored. The true shear strain can be found by splitting the shape change from deformation into a pure rotation term and a pure deformation term, as illustrated in Figure 2.4. From this figure the true shear strain components $\epsilon_{12} = \epsilon_{21} = \frac{\gamma}{2}$ can be found[15].

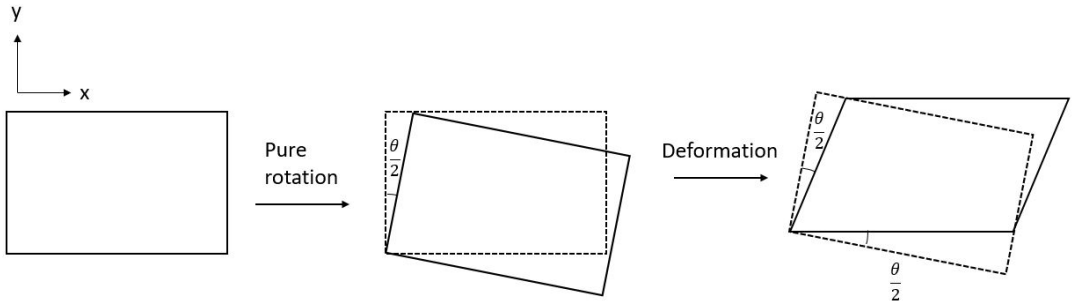

Figure 2.4: True shear strain.

2.2 Deformation by slip in single crystals

A slip system consists of a crystallographic plane and a direction in this plane. A dislocation can glide in the slip system. In fcc single crystals the slip systems consist of {111} planes and ⟨110⟩ directions. Slip begins when the critical resolved shear stress is obtained in the slip plane and the slip direction. Schmid[15] was the first to recognize that different tensile loads are required to produce slip in single crystals of different orientation. The critical resolved shear stress can be found by considering a cylindrical single crystal, as shown in Figure 2.5. From Figure 2.5 the area of the slip plane will be $A/\cos\phi$, and the axial load in the slip plane in the slip direction is $P\cos\lambda$. The critical resolved shear stress is given by Equation 2.8, but is only valid for an ideal single crystal tensile specimen.

$$\tau_R = \frac{P\cos\lambda}{A/\cos\phi} = \sigma\sin\phi\cos\lambda = \sigma m \tag{2.8}$$

m in Equation 2.8 is called the Schmid factor, and slip will first occur in the slip system with the largest Schmid factor.

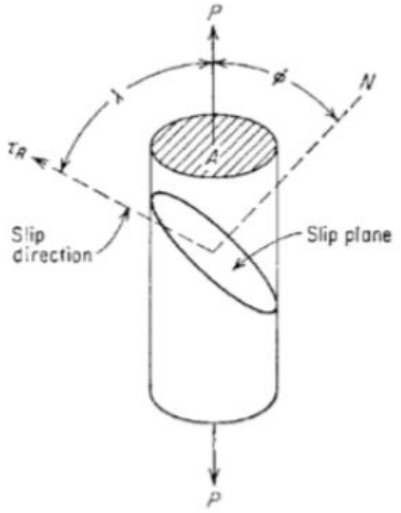

Figure 2.5: Diagram for calculating critical resolved shear stress from [15]. A is the cross-section area, ϕ is the angle between the normal of the slip plane and the tensile axis and λ is the angle the slip direction makes with the tensile axis.

2.3 Dislocation movement

Dislocations are line defects in a crystal structure. Screw- and edge dislocations are two special cases of dislocations. In general, a dislocation will have both screw and edge character.

2.3.1 Cross slip

Dislocations can glide in the slip plane, but only a pure screw dislocation can glide onto another plane by cross slip. In Figure 2.6 a dislocation loop of mixed character is gliding in the (111) plane. The b) situation illustrates a shear stress causing the dislocation loop to expand towards the $(1\bar{1}1)$ plane. The pure screw component of the dislocation loop can move onto the $(1\bar{1}1)$ plane, this is illustrated in situation c). Only the screw component of the loop that can move on the cross-slip plane, the $(1\bar{1}1)$ plane in this case[15]. In the d) situation in Figure 2.6 the loop glides back onto the original (111) plane and this is called double cross slip[15].

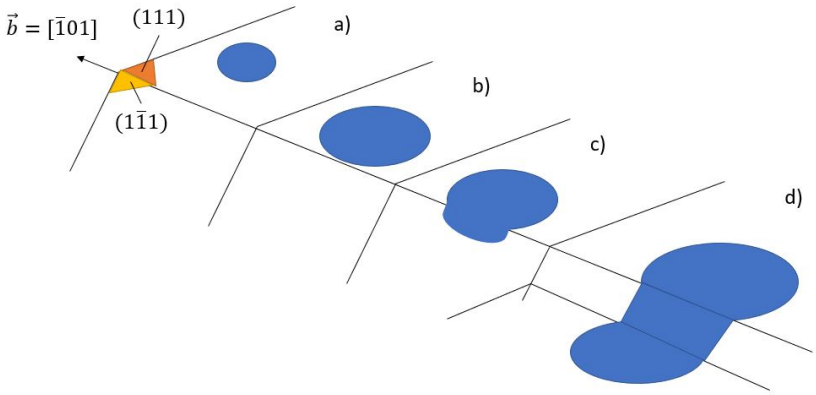

Figure 2.6: Cross slip in a fcc crystal.

2.3.2 Dislocation climb

An edge component of the dislocation cannot cross glide, since it only can glide in a slip plane containing the dislocation line and its Burgers vector. An edge dislocation can however move onto a parallel plane above or below the slip plane by dislocation climb, as illustrated in Figure 2.7. In a positive climb an extra half plane moves up one atom spacing because atoms are removed from the extra half plane of atoms at a positive edge dislocation. In negative climb the dislocation line moves down one atom spacing, by adding an extra half plane below.

Climb occurs by diffusion of vacancies or interstitial atoms, and the usual mechanism for positive climb is vacancy diffusion to the dislocation. Climb is a nonconservative movement, and since climb is diffusion-controlled it will occur more rapidly with elevated temperatures[15].

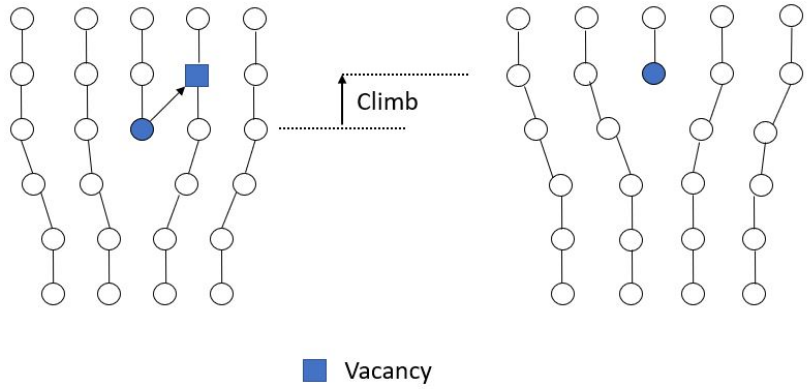

Figure 2.7: Dislocation climb.

2.3.3 Dislocation intersections

A crystal may contain many dislocations, and frequently moving dislocations in its slip plane will interact with other dislocation crossing the slip plane. The intersection of two dislocations will produce a sharp break in the dislocation line. These breaks can be characterized as a kink or a jog. In a kink the sharp break will be created in the current dislocation plane[15]. In a jog the dislocation is moving out of the slip plane and create a sharp break[15].

The most important dislocation intersection, in a plastic deformation point of view, is the intersection of two screw dislocations[15]. This process is illustrated in Figure 2.8. When the two screw dislocations meet they will produce jogs of edge character in both dislocations. For the jog to move it has to climb, and this will create vacancies as illustrated in Figure 2.8. Climb is a thermally activated process, and the motion of screw dislocations will be temperature dependent[15]. At low temperatures, where climb cannot occur, the screw dislocation will be impeded by jogs[15].

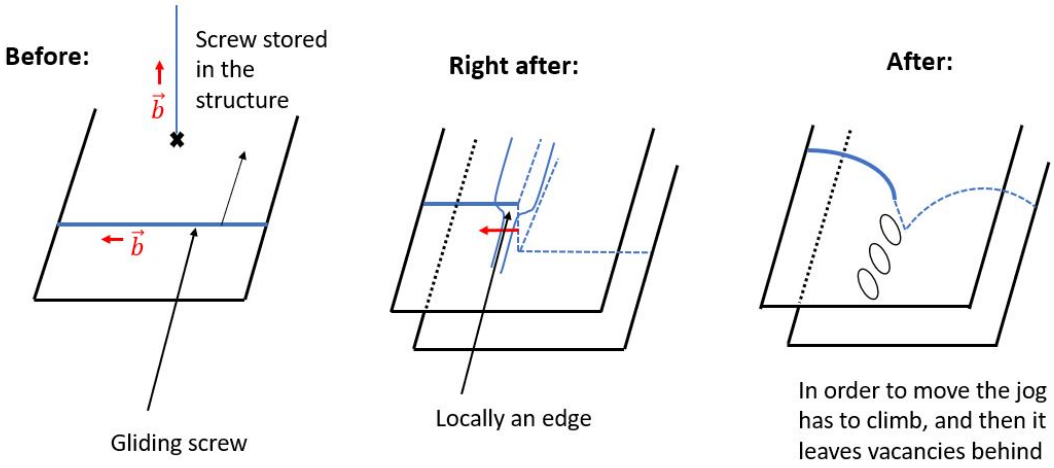

Figure 2.8: Intersection of two screw dislocations.

2.4 Strain hardening of polycrystals

An schematic illustration of a flow curve for fcc polycrystal is plotted in Figure 2.9. Strain hardening, θ, is defined as:

$$\theta = \frac{d\sigma}{d\epsilon} \tag{2.9}$$

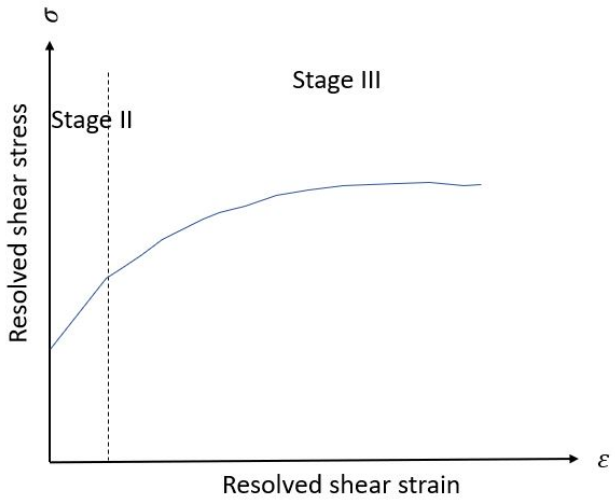

Figure 2.9: Illustration of a flow curve for fcc polycrystals. Stage II is significant larger than an experimental aluminium flow curve. The larger dimensions are chosen to highlight stage II.

The strain hardening at a specific strain is given by the slope of the true stress-strain curve at the specific strain. The stress-strain curve of a single crystal fcc can be divided into three stages. In stage I slip occurs in only one slip system. In polycrystals it is assumed that multiple slip systems get activated in every grain, and thereby stage I will not exist in polycrystals. For metals with high stacking fault, like aluminium, the flow curve usually shows a small stage II region because deformation at room temperature easily occurs by cross slip[15].

Stage II starts when more than one slip system gets activated. Stage II is characterized by

a large linear increase in stress with increasing deformation. By Equation 2.9 this gives large strain hardening. In this stage slip occur on more than one slip system, and as a result of several active slip systems lattice irregularities are formed[15]. During stage II the ratio of the strain hardening coefficient to shear modulus is nearly independent of stress and temperature, and approximately independent of crystal orientation and purity[15]. The main strain mechanism is assumed to be piled-up groups of dislocations, and the fact that the slop of the curve is nearly independent of temperature agrees with this theory[15]. With increasing strain more Lomer-Cottrell barriers are formed. The Lomer-Cottrell locks cannot be overcome by successive dislocations. These will be caught up in the locks in the crystal and get immobilized, but the dislocations will contribute to further increase of the internal stresses[16]. This leads to a larger activity of secondary slip systems[16]. During stage II a rapid increase of dislocation density will take place. The increase is caused by immobilized dislocations from the Lomer-Cottrell locks. For each of the immobilized dislocations another mobile dislocation must be generated to maintain the imposed strain rate[16]. This will lead to increasing dislocation density. The mobile dislocations can be generated through Frank-Read sources. The strain hardening, θ, is approximately independent of stress and temperature in stage II, indicating that annihilation processes are not dominating.

Stage III is often called dynamic recovery, and the region is characterized by a decreasing hardening rate. The main reason for the decrease is cross slip of screw dislocations[16], as explained in Section 2.3.1. In stage III the Schmid-factor of the cross slip plane is smaller than for the primarily slip plane. An adequate shear stress is therefore necessary to make the dislocation move onto the cross slip plane[16]. At the high stresses in stage III the dislocations can take part in processes that are suppressed at lower stresses[15]. The stresses indicating the beginning of stage III are strongly temperature dependent. Therefore a crystal strained at stage III is much more temperature dependent than the crystal strained at stage II[15]. This temperature dependency indicates that the intersection of forests of dislocations are the main strain hardening mechanism in stage III[15].

2.5 Texture

Texture refers to the tendency of preferred crystallographic orientations. The texture evolves during all stages of metal manufacturing, and give solidification textures, deformations textures and annealing textures. In metals which undergo large amounts of deformation, crystallographic planes tend to develop deformation texture. This are a result of crystallographic constraints and external constraints. The preferred orientation is strongly dependent on the slip and twining systems used in the deformation[15], and will be further explained in the section below. Annealing texture can be a recrystallization texture, which consists of nucleation of new grains. The new grains grow at the expense of the deformed surrounding structure. The recrystallization texture is different and sometimes stronger than the existing deformation texture[15], and is further explained in Section 2.5.2.

2.5.1 Rolling texture

The rolling texture in fcc metals depend on the stacking fault energy, and the different texture types within fcc rolling textures are represented by their strongest texture components. Fcc metals with high stacking fault, like aluminium and copper, have S, Cu and brass texture[22]. Metals with low stacking fault, like brass, silver, gold and fcc stainless steel, have brass and goss textures[22]. The miller indices of the texture components are given in Table 2.1. In this context the high stacking fault texture components are more relevant than the low stacking fault components.

Notation	Miller indices
High stacking fault	
S	$\{123\}\langle 41\bar{2}\rangle$
Cu	$\{112\}\langle 11\bar{1}\rangle$
Brass	$\{110\}\langle 1\bar{1}2\rangle$
(Low stacking fault)	
(Brass)	$(\{110\}\langle 112\rangle)$
(Goss)	$(\{110\}\langle 001\rangle)$

Table 2.1: Summary of rolling textures in fcc metals with high and low stacking fault, from [22].

2.5.2 Recrystallization textures

Recrystallization texture develop when deformed metals are annealed, and different recrystallization textures and their Miller indices are given in Table 2.2. The resulting recrystallization texture depend on the texture produced by the deformation. An experiment is illustrated in Figure 2.10. The temperature T is given, and tensile test are performed at different holding times, t, to give the curve in Figure 2.10. The curves starts as rolled, and in the first stage it will experience recovery, where the dislocations inside the subgrains will anneal and the subgrains will grow. This leads to decrease in strength, but very small texture change[22]. In the recrystallization phase new grains nucleate, and the nuclei grow at the expense of the surrounding grainstructure. The nucleation first occurs at the grain boundaries at the old deformation structure, and the preferential orientation of the nuclei depend on the deformation texture. The recrystallization texture depends on the preferential orientation of the nuclei. For this reason the recrystallization depends on the deformation texture[15].

Notation	Miller indices
Cube	$\{001\}\langle 100\rangle$
-	$\{236\}\langle 385\rangle$
Goss(G)	$\{011\}\langle 100\rangle$
S	$\{123\}\langle 634\rangle$
P	$\{011\}\langle 122\rangle$
Q	$\{013\}\langle 231\rangle$
R	$\{124\}\langle 211\rangle$

Table 2.2: Recrystallization textures in fcc metals, from [42]

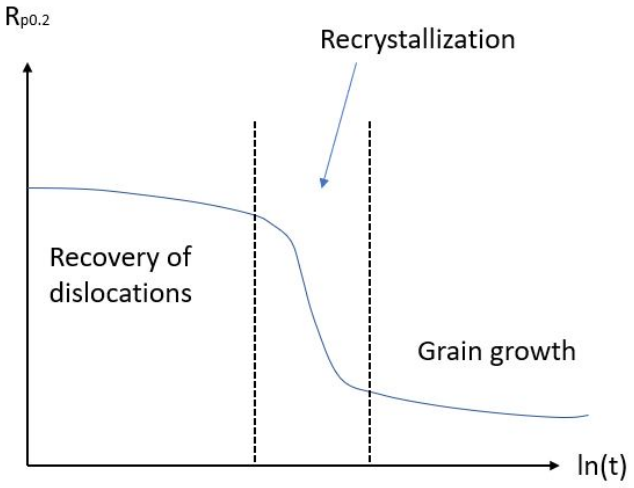

Figure 2.10: Illustration of an tensile specimen experiment. The temperature T is given, and tensile test are performed at different holding times, t. This give the $R_{p0.2}$ of the tensile specimens.

When deformed single phase aluminium metal gets annealed, a characteristic cube structure develops in the material[42]. The origin of the cube texture in fcc metals can be difficult to explain because a significant $\{001\}\langle 100\rangle$ cube component is generally not indicated in pole figures or ODF data of cooled rolled material[42]. Two different models have been suggested to explain the origin, the Transition Band Model and Cube-Band Model. Meanwhile the Cube-Band Model is most seen for commercial aluminium alloys[42].

Cube-Band Model

Cube-oriented elements of the previous deformed structure have maintained long ribbon-like bands (Cube bands). According to this model, the cube bands are the origin to cube grains in the recrystallized texture after hot deformation[42]. Strain-induced boundary migration(SIBM) at the boundaries of cube oriented regions is the mechanism in recrystallization from cube bands[42, 51]. The SIBM mechanism is illustrated in Figure 2.11. In SIBM a part of the grain boundary bulges out. The region behind the bulging part has a lower density of dislocations and creates a subgrain.

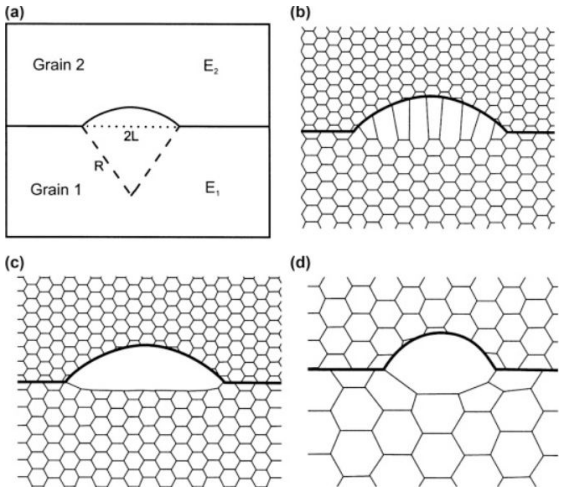

Figure 2.11: The SIBM mechanism: (a) The low stored energy(E_1) Grain 1 and higher stored energy (E_2) grain 2 is separated by a grain boundary (b) by SIBM the dislocation structure is dragged behind the migrating boundary (c) the migrating boundary is free of the dislocation structure (d) SIBM creating a single large subgrain.

2.5.3 Modeling of stress and strain in different textures

A tensile test with two different textures is schematically illustrated in Figure 2.12, and a derivation of stress and strain in the textures follows. The polycrystalline stress-strain curve is described by Equation 2.10-2.12

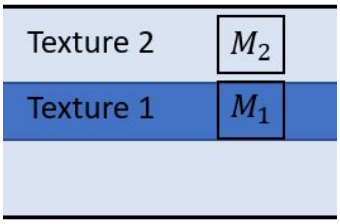

Figure 2.12: A tensile specimen with two different textures, one texture in the middle and another in the surface, and two different Taylor factors, M_1 and M_2.

$$\tau = K\gamma^n \tag{2.10}$$

$$\sigma = M\tau \tag{2.11}$$

$$\epsilon = \frac{\gamma}{M} \tag{2.12}$$

where τ is the critical resolved shear stress, K is a constant, γ is the shear strain, n is the strain hardening coefficient, σ is the stress, M is the Taylor factor and ϵ is the strain. The validity of Equation 2.10-2.12 is commented by Kocks[32]. The stresses from the two different textures in Figure 2.12 are given by Equation 2.11. By substitution of Equation 2.10 and 2.12 into Equation 2.11, an new expression of the stress is obtained in Equation 2.13 and 2.14.

$$\sigma_1 = M_1\tau_1 = M_1K(M_1\epsilon)^n = M_1^{1+n}K\epsilon^n \tag{2.13}$$

$$\sigma_2 = M_2^{1+n} K \epsilon^n \tag{2.14}$$

By combining Equation 2.13 and 2.14, the stress relationship between the two textures are revealed in Equation 2.15.

$$\sigma_2 = (\frac{M_2}{M_1})^{1+n} \sigma_1 \tag{2.15}$$

If texture 2 in Figure 2.12 referrers to random texture and texture 1 referrers to cube texture, which is similar to AA6063 extrusion textures. Then $M_2 = 3.1$ and $M_1 = 2.5$ according to full constraint(FC) Taylor model[32]. The Considère criterion, given in Equation 2.16, signifies the point at necking in a true stress-strain curve.

$$\frac{d\sigma}{d\epsilon} = \sigma \tag{2.16}$$

By the Considère criterion, the strain hardening coefficient n is equal to the uniform strain, ϵ_u. From the project thesis, a crude estimation of ϵ_u is 0.20 in the investigated AA6063. This give $n = \epsilon_u \approx 0.2$. If the value of the Taylor factors and the strain hardening coefficient are put into Equation 2.15, the stress relationship will be:

$$\sigma_2 \approx 1.29\sigma_1 \tag{2.17}$$

The approximation of n is crude and the value might rage from 0.15 to 0.25. This approximation will not greatly influence the resulting stress relationship. If $n = 0.15$ this will result in $\sigma_2 = 1.28\sigma_1$, and if $n = 0.25$ this will results in $\sigma_2 = 1.31\sigma_1$. The results will range from 1.31 to 1.28 and result in a difference of $\Delta = 1.31 - 1.28 = 0.03$. This is possible error of 2.3% of the approximated value $1.29\sigma_1$.

By using Equation 2.16, the Considère criterion, a relationship between the uniform strain of the two textures can be established. Equation 2.13 and 2.14 combined with Equation 2.16 give:

$$\frac{d\sigma_1}{d\epsilon} = \sigma_1 \Rightarrow n = \epsilon_u \tag{2.18}$$

$$\frac{d\sigma_2}{d\epsilon} = \sigma_2 \Rightarrow n = \epsilon_u \tag{2.19}$$

Both textures will give the same uniform strain, and the uniform strain seems independent of the texture. This is also illustrated in Figure 2.13.

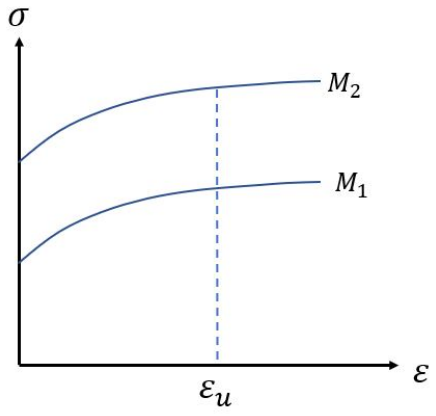

Figure 2.13: The uniform strain is independent of texture, both texture 1 and texture 2 will have the same uniform strain.

The derivation above is only valid for a tensile specimen, and the M values in Equation 2.10-2.12 are found by FC Taylor model. This model is a statistical model, and the basic simplifying

assumption for this model is that the shear stress is the same in all the slip systems[47]. For a tensile test this can be a reasonably approximation. Meanwhile the grain shape and the interactions between the grains are not accounted for in the FC Taylor model. One approach to account for this is to use the crystal plasticity model with the finite element method (CPFEM). CPFEM is used in K. Zhang et al.[53] to find new reference values for the Taylor factor. Zhang, K et al.[53] concluded with a new reference value for fcc metals with a Taylor factor of 2.7 for random texture. This is a much smaller value than the reference value based on the FC Taylor model.

2.6 Strain ageing

2.6.1 Lüders band

Low-carbon steel is used to explain the concept of Lüders band and strain ageing. Low-carbon steel differ from aluminium in the fact that gases are more involved in steel, than aluminum. This gives a short range diffusion, which is not the case in aluminum. The Lüders band phenomenon seen in Figure 2.14 is caused by interstitially dissolved carbon and nitrogen atoms, which diffuse to edge dislocations. The yield point, A, in Figure 2.14 coincident with the formation of a Lüders band, which is a region of stable local deformation. The Lüders band is created 45°to the direction of loading. The formation of a Lüders band is followed by a sudden drop in stress where the Lüders band will increase in size with deformation and propagate trough the entire gauge length of the tensile specimen.

At point A in Figure 2.14 the dislocations (how earlier diffused to carbon and nitrogen) are freed from the carbon and nitrogen atoms. A high stress is required for the release of the dislocations and this creates a large yield stress. The drop in stress after point A is caused because less energy is needed to move the dislocations than to break them free. This result in a plateau between B and C[23]. Global plastic deformation of the tensile specimen starts after the Lüders bands have propagated through the specimen, and the material undergoes conventional plastic deformation until fracture.

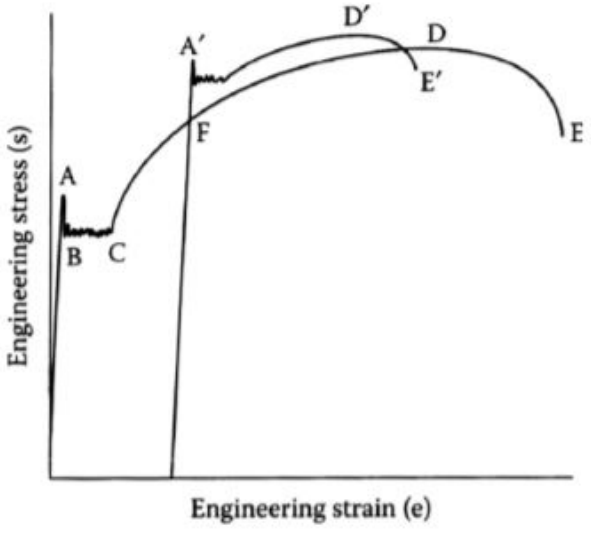

Figure 2.14: Tensile stress-strain curve of low-carbon steel, from [23].

2.6.2 Dynamic strain ageing

Serrated stress-strain curves, where sudden load drops correspond to bursts of plastic deformation and stretcher strains indicate dynamic strain ageing. Dynamic strain ageing (DSA) is a result of attraction of solute atoms to dislocations. The source is similar to Lüders band, a greater force is needed to initiate plastic deformation by freeing the dislocations than to move the free dislocations[23]. DSA differ from traditional strain ageing because temperature and a strain rate allows the solute atoms to pin the dislocations while the material is deforming. In DSA the tensile specimen is not unloaded and reloaded.

2.6.3 Aluminium

In tensile testing some aluminium alloys will give serrated tensile curves because of DSA. Bands of localised plastic deformation, also called Portevin-Le Chatelier(PLC) effect, is a consequence of DSA. Regarding AA6xxx alloys Mg and Si atoms cause DSA. During deformation, the rate of speed of the dislocations are slower than the diffuse rate of the Mg and Si atoms at room temperature[15]. This leads to magnesium atoms diffusing to the dislocations and lock them[15]. In a tensile specimen load must be increased in order to tear the dislocations away from the solute atoms. This increases the stress level for a brief period to break the PLC bands, and then the stress level drops again[15]. This is a repetitive phenomenon and gives rise to the serrated yielding in Figure 2.15. AA5xxx alloys are often subjected to DSA, and the negative strain-rate sensitivity caused by DSA can lead to reduced ductility[29]. In this context ductility is strain corresponding to maximum true stress attained[29].

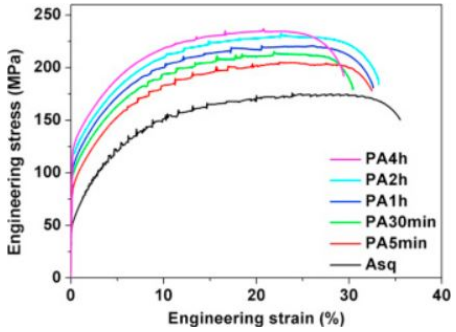

Figure 2.15: Example of tensile curves from an AA6xxx alloy investigated by Zhong et al. [54]. The curves experience dynamic strain ageing in the form of Portevin-Le Chatelier effect.

2.7 Experimental methods and supplementary information on the experimental work

In this section background material on some of the experimental techniques and mathematical relations related to post processing of the results are presented. Additional information of experimental techniques are attached since the report also has an industrial aspect.

2.7.1 Mathematical relations in post processing of data

The area fraction fracture strain is an interesting measurement in the context of ductility. It is given by Equation 2.20

$$\epsilon_f = \ln \frac{A_0}{A_f} \tag{2.20}$$

Where A_0 is the original cross-section area and A_f is the cross-section area at fracture.

2.7.2 EBSD

Electron backscatter diffraction (EBSD) is a method to provide information about crystallographic orientations in a section of the microstructure[37]. In the vacuum chamber of the SEM the sample is tilted 70°, and a stationary beam of high energy electrons hit the sample. The high energy electrons interact with the sample surface and create backscattered electrons. The backscattered electrons create a Kikuchi pattern, on a phosphor screen[44]. A setup is illustrated in Figure 2.16. A Kikuchi pattern is caused by Bragg reflections, and the pattern is a regular arrangement of parallel bright bands on a continuous background[44]. The bands represent different atom planes in the lattice, and the width of the bands are related to Bragg's law. This information makes it possible to find the crystal's orientation,

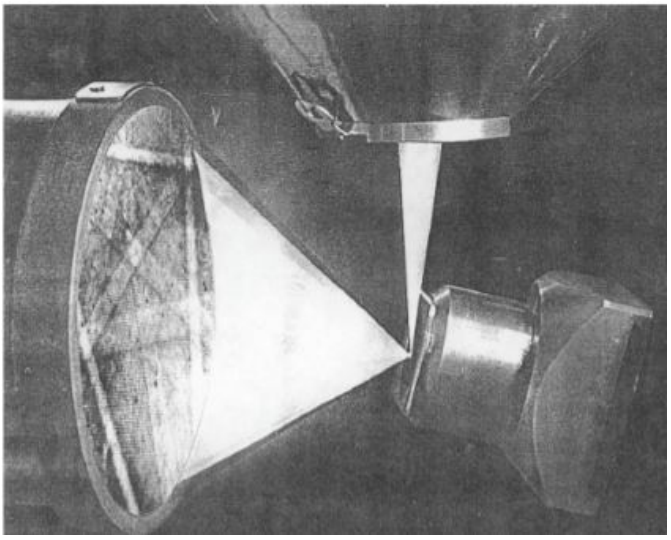

Figure 2.16: Illustration of a SEM vacuum chamber during an EBSD analysis. The sample (to the right) is tilted 70°, and a Kikuchi pattern is shown on the phosphor screen to the left[20].

By scanning an area, different crystal orientations will be identified. The program TSL OIM Analysis 7 is used to present the results from the EBSD scan. The program can generate pole figures, orientation maps, ODF's and plot of grain structures. This can be used to find information about grain orientations, texture, point-to-point orientation correlations, and phase identification and distributions[44].

TSL OIM data collection 7 is used in the post processing process. In this process each EBSD pattern must be indexed. In the indexing, measured interplanar angles (angles between Kikuchi bands) and interplanar spacing (Kikuchi band widths) are compared to theoretical values for a known crystal structure, aluminium in this case[44]. CI, confidence index, is a measurement of the probability that the correct solution has been found. CI is calculated by comparing measured interplanar angles and spacing to the theoretical, and will be a value between 0 and 1. CI is calculated by using the relationship between the highest number of indexed bands and the number of bands used for indexing the pattern[44]. In the indexing process in TSL OIM data collection 7, 5 calibration images are tuned to get the best indexing, preferably CI above 0.8.

Inverse pole figure map

Inverse pole figures (IPF) show the crystallographic poles aligned with a specific sample direction[37]. The construction of an inverse pole figure is quite similar to the construction of a normal pole figure. In a normal pole figure a crystallographic pole is projected, by stereographic projection, onto a plane determined by the sample geometry. Inverse pole figure on the other hand is constructed by projecting the vector pointing along a given sample direction, onto planes

determined by the local crystallographic orientation[37]. The inverse pole figure is completed by plotting all the projection together. IPFs for cube-, copper- and brass texture are given in Figure 2.17. Figure 2.17a, 2.17c and 2.17e contain 24 stereographic triangles, and each triangle contains the same orientation information. The standard stereographic triangle is shown in Figure 2.17a, 2.17c and 2.17e with bold lines. The standard triangle contains crystallographic directions, $\{hkl\}$, with $l \geq h \geq k \geq 0$.

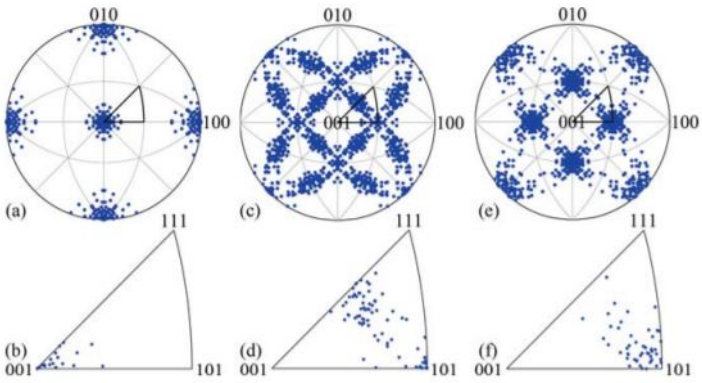

Figure 2.17: Inverse pole figures for Cube texture(a), Copper texture(c) and Brass texture(e) in the normal-direction. From [37].

In the context of EBSD, an inverse pole figure map (IPF map) can be used to investigate the texture of a sample. This is illustrated in Figure 2.18. The IPF map is used qualitatively to find dominating orientations or texture in a sample. In Figure 2.18 red is dominating, this indicate cube texture of the aluminium sample.

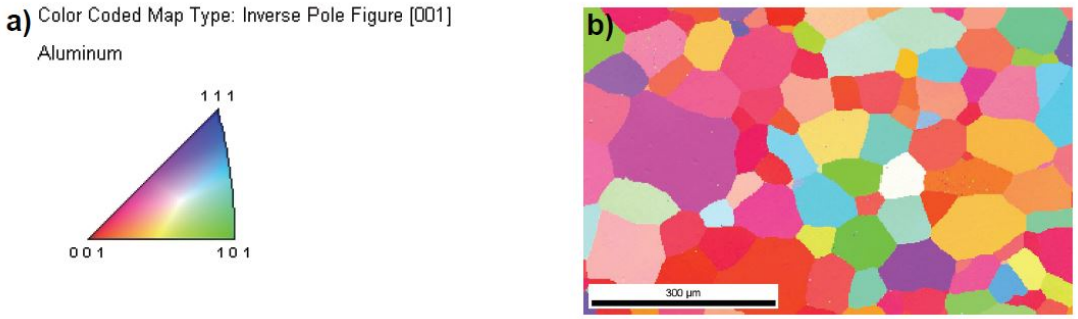

Figure 2.18: An inverse pole figure map of an aluminium sample and the associated stereographic triangle with the crystal direction parallel with the sample normal, TD. IPF map corresponds to cube texture in the aluminium sample. From [45].

2.7.3 EDS

The electrons in the atom are at discrete energy levels, and primary electrons with enough energy can excite the atom. The atom retrieves it ground state by electrons from shells further out filling the shells closer to the atom nucleus. To maintain the energy balance, photons with discrete energy are emitted when electrons fall down to fill empty electron positions closer to the nucleus[21]. This is illustrated in Figure 2.19.

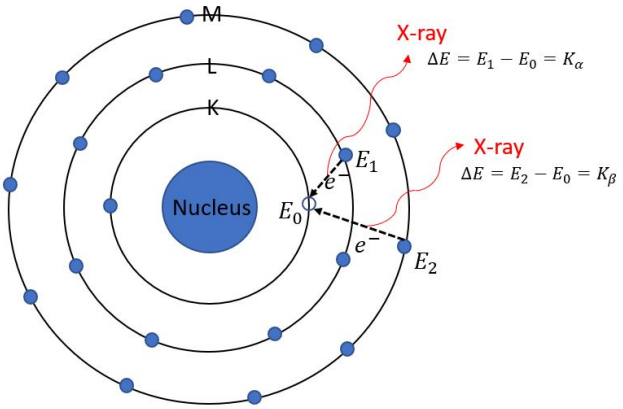

Figure 2.19: Illustration of the process then the atom emits photons with discrete energy levels

In energy-dispersive X-ray spectroscopy (EDS) the phenomenon described above is utilized. The wavelength and energy of the photon are characteristic for the atom number. In the microscope, electrons from the microscope interact with the electrons in the atom and characteristic photons are formed[21]. An intensity specter is made, and from the positions of the intensity peaks it is possible to identify the elements in the sample.

To quantify the result in EDS the ZAF method is used. The ZAF method is derived by Castaing in 1951[21]. In ZAF the measured intensity peaks are compared to the intensity peaks of a pure sample or a reference[21]. In addition, three correction factors are calculated in the analysis: Atom number effect (Z), absorption (A) and fluorescence(F). All the correction factors are the ratio between the measured sample and the reference sample[21]. The ZAF analysis is summarized in the equation below

$$C_i = (ZAF)_i \frac{I_i}{I_{(i)}} \tag{2.21}$$

where C_i is the concentration of element i in the sample, I_i is the measured intensity in the sample, $I_{(i)}$ is the measured intensity in the reference sample and ZAF stands for the correction factors mentioned above. This analysis is performed automatically by the data processing program[21].

2.7.4 Uniaxial tensile testing

In tensile testing, uniaxial force is applied to a tensile specimen. The deformation of a specimen during the applied load is quantitative measured by force-extension data. The force-extension data can be used to provide several mechanical properties, which are listed below[28]:

- Elastic deformation properties, like Young's modulus and Poisson's ratio
- Yield strength and ultimate tensile strength
- Elongation and reduction in area
- Strain hardening characteristics

Stress measuring

Equation 2.1 is used for measuring the stress, because the area is decreasing during the test. After necking, the stress required for deformation is lower than predicted by Equation 2.1, due to hydrostatic pressure in the centre of the neck[28].

Strain measurement

The deformation, or strain, of the specimen can be measured by an extensometer. The extensometer can be clip-on, directly-mounted strain gauges and optical devices. The length of the extensometer can affect the strain measurement, for example the ϵ_f value. A small extensometer can give larger values for ϵ_f than a larger extensometer. This is discussed in the author's project work, an excerpt of this discussion is given in appendix A.

Necking

During deformation in tensile testing, the tensile specimen will experience necking, and there are a distinction between local necking and diffuse necking. The point of flow instability marks the start of diffuse necking at the maximum load (ultimate tensile strength). For a material obeying the power law hardening, $\sigma = K\overline{\epsilon^n}$, the strain at diffuse neck can be derived by using the Considere criterion, $\frac{d\sigma}{d\epsilon} = \sigma$. Combining the power law and Considere criterion (Equation 2.16) to Equation 2.22:

$$Kn\epsilon_1^{n-1} = K\epsilon^n \tag{2.22}$$

where K is a constant, n is the strain hardening and ϵ is the strain. Equation 2.22 turns into Equation 2.23:

$$\epsilon_1^* = n \tag{2.23}$$

and the diffuse necking will start at $\epsilon^* = n$. The diffuse neck is followed by contraction strains in width and thickness directions, and the local neck can only form when $dF = 0$[24]. F can be expressed as σA, and this give Equation 2.24.

$$\sigma_1 dA + Ad\sigma_1 = 0 \tag{2.24}$$

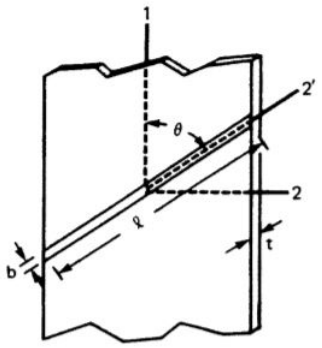

Figure 2.20: Development of necking in a tensile specimen, from [24]

The further derivation is based on constants and variables found in Figure 2.20. $\frac{dA'}{A'} = \frac{dt}{t} = d\epsilon_3$, A' is the cross-section area of the neck, and can be expressed $A' = lt$[24]. l is constant and thereby the relation $\frac{dA'}{A'} = \frac{dt}{t} = d\epsilon_3$ can be established. A is the area perpendicular to the 1-axis, and expressed $A = A'sin\theta$, but θ is constant and gives[24]:

$$\frac{dA}{A} = \frac{dA'}{A'} = d\epsilon_3 \tag{2.25}$$

Equation 2.25 is used to give the relation below:

$$\frac{d\sigma_1}{\sigma_1} = -\frac{dA}{A} = -\epsilon_3 \tag{2.26}$$

For uniaxial tension in the 1-direction, the flow rules for an isotropic material predict[24]:

$$d\epsilon_2 = -\frac{d\epsilon_1}{2} = \epsilon_3 \tag{2.27}$$

Equation 2.26 combined with Equation 2.27 gives:

$$\frac{d\sigma_1}{\sigma_1} = \frac{d\epsilon_1}{2} \tag{2.28}$$

By using the power law, $\sigma = K\epsilon^n$ for uniaxial tension, $d\sigma_1 = nK\epsilon_1^{n-1}d\epsilon_1$. This put into Equation 2.28 gives:

$$\frac{nK\epsilon_1^{n-1}d\epsilon_1}{\sigma_1} = \frac{d\epsilon_1}{2} \tag{2.29}$$

this is simplified to:

$$\epsilon_1^* = 2n \tag{2.30}$$

$2n$ is the critical strain for localized necking in uniaxial tension, in comparison the critical strain for diffuse necking is $\epsilon_1^* = n$.

3. Literature study

This chapter will give an overview of some central concepts related to fracture and ductility and the stress-strain curve in AA6xxx unless another alloy is mentioned. Regarding tensile directions, all directions are given with respect to ED. The chapter will be based on published articles within the areas of bendability, texture, anisotropy, work hardening and fracture. The various topics will be discussed on a general basis in the following sections, but all topics are all related to the specific extruded AA6063. The relation to the experimental results will be discussed further in the discussion chapter.

3.1 Definition of ductility

The topic of this report is a ductility investigation, but ductility is a widely used concept and is not a very specific term. Ductility can be used in the context of necking in tensile testing, shear band formation during bending and total failure in vulnerable points in the structure e.g. a weld. Initially during tensile testing the deformation is uniform and upon flow instability a diffuse neck starts to form, followed by a localized neck and fracture. Ductility in this case can both be measured by elongation or area fraction, and the neck will be the center of both measurements. Ductility in the context of bending do not experience the same flow instability as the tensile specimen. The bending specimens experience a larger quantity of strain than the tensile specimens, and the fracture starts just beneath the surface. The focus of the ductility investigation in this report will be the tensile testing, and the main part of the literature study will be focused on ductility through tensile testing. Since bendability is involved in the further shaping of the automotive parts the next section will comment on bendability.

3.2 Bendability

Bending processes are often involved in the further shaping of many automotive parts, including the investigated profile AA6063. Due to this bending process, certain demands to strength and fracture strain are put on the profile. This section is included to enlighten areas that affect the bendability. It is also important for a deeper understanding of how texture, precipitation particles and grain size will affect both tensile testing and bending.

During bending microscopic shear bands will develop at the surface of an aluminium sheet at a certain stage during plastic deformation. The bands will then spread into the sheet thickness, leading to failure of the material[26]. According to Ikawa et al.[26] the bendability of aluminium alloys are reported to depend on amounts of solute atoms[2, 38], population of precipitation particles[3] and texture[25, 33].

Kuroda and Tvergaard[33] found, through crystal plasticity simulations of different textures in polycrystalline aluminium, that crystal orientation influence the bendability. Cube texture was found to be advantageous for preventing the shear band development, which limits the bendability[33]. Ikawa et al.[26] investigated the effect of crystal orientation on the bendability on AA6061-T4. In Ikawa et al.[26] a finite element analysis with a crystal plasticity model was used to simulate single crystal specimens, and this was combined with experimental work. In the experimental work an rolled AA6061-T4 alloy sheet with clear areas of cube and Goss texture was used. The bending specimens were cut from the areas of pure cube and Goss areas. Experimentally in Ikawa et al.[26], the cube specimen showed good bendability without any surface waviness and no breakage for both 0°, 45°and 90°to the rolling direction. The experimentally tested Goss specimens were strongly dependent on direction, where 0°experienced good bendability. Meanwhile 45°and 90°to the rolling direction showed poor bendability [26]. The simulated results in Ikawa et al.[26] were consistent with the experimental, even though the simulated results were based on single crystal specimen. The results from the cube specimen

corresponded well to the simulations of Kuroda and Tvergaard[33]. The physical reasons for the observations have not yet been clarified[26], but the mechanisms for formation of shear bands have been investigated by Hill[18], Hill and Hutchinson[19] and Asaro et al.[4].

Minoda et al.[38] documented the effect of iron on the bendability of an AA6016-T4 alloy rolled sheet. Meanwhile almost no iron solves in aluminium solid solution, and as a result this study is a study of the effect of constituent particles. Minoda et al.[38] observed a decrease in bendability in T4 with iron. Minoda et al.[38] concluded that the decrease in bendability were a combined effect of increase in $\beta - AlFeSi$ particles and shear bands, which increase with iron content. Minoda et al.[38] observed the worst bendability at 0.5mass% iron, and above 0.8mass% the bendability stayed the same or improved. Minoda et al.[38] suggested the lack of decrease in bendability was caused by decrease in shear band formation.

Asano et al.[2] documented the effect of copper on an Al-Mg-Si alloy rolled sheet in T4 condition. Copper solve much better in aluminium than iron, and this study will consider copper in solid solution. Asano et al.[2] also observed a decrease in bendability in T4 with increased copper content. Asano et al.[2] considered that the decrease in bendability with increasing copper was caused by increased formation of shear bands. Cracks easily form along shear bands during the bending and cause failure. In Asano et al.[2] the 1mm thick specimens were solution heat treatment (SHT) in salt bath at 550°C, for 15s, 45s, 75s and 300s. By solution heat treatment of 75s, Asano et al.[2] found that the size distribution of the precipitation particles did not depend on the copper content. Thereby they concluded that only the shear bands contributed to decreasing the bendability.

Stagnation and improvement of bendability above 0.8mass% is observed in Minoda et al.[38] (tested iron), and not observed in Asano et al.[2] (tested copper). Copper and iron also have two different effects with aluminium. Iron affect the aluminium as constituent particles and copper is in solid solution. These two different effect in aluminium can be some of the reason to the observed stagnation and improvement above 0.8mass% iron.

Asano et al.[2] also observed an effect of SHT time on the bendability of Al-Mg-Si alloy containing 0.8mass% Cu. The maximum crack depth caused by cracks during bending increased with SHT up to 75 sec, and then decreased over 75 sec[2]. It was also observed an increase in the formation of shear bands and a decrease in precipitation particles with increased SHT time[2]. From these observations Asano et al.[2] concluded that the occurrence and propagation of cracks by bending are caused by the combined effect of: (1)Shear band formation across grains and (2)precipitation particles where micro-voids form. The observation by Asano et al.[2] of occurrence and propagation of cracks, correspond with a previous study by Asano, Uchida and Yoshida[3].

3.3 Texture

The texture is usually considered to be the main and often only source to plastic anisotropy in Al alloys[30]. Since the next sections will feature anisotropy, fracture and strain rate, this section contains additional information to support the next sections.

Figure 3.1 show similar alloys, but from two different articles, Khadyko et al.[30] and Ryen[43]. Both Khadyko et al.[30] and Ryen[43] investigated AA6063 in as extruded condition. The EBSD maps in Figure 3.1 are shown in two different ways. The map from Ryen[43] in Figure 3.1a is drawn with an algorithm that will give the grains almost random colors, but neighboring grains will not have the same color. The EBSD map from Khadyko et al.[30] in Figure 3.1b is given as an inverse pole figure map (IPF map), with TD as the IPF axis. The red colored grain in Figure 3.1b indicate cube texture and the green/yellow grains in Figure 3.1b indicate Goss texture. Two neighboring grains in this map can have the same color, unlike Figure3.1a. The profiles in Figure 3.1 are the same flat profile having a width of 205mm and a thickness of 3mm. Both subfigures show the characteristic extrusion grain structure for recrystallized alloys. The layer

of larger grains closer to the surface, often Goss grains, seems larger in 3.1a than 3.1b. The homogenization treatment is approximately the same in both articles, but in Khadyko[30] the billets are extruded at ram speed 20mm/s, and in Ryen[43] the ram speed is 15mm/s. Based on the very similar production route of the two profiles, the larger layer of larger grains/Goss grains can be caused by natural variations. The scanning area of the 3.1b profile clearly is larger than the 3.1a profile, and with a larger scanning area the natural variation is more clear.

ODF results from Ryen[43] reveal cube orientation ({001}) in the small grains in the middle of Figure 3.1a, followed by Goss orientation ({101}) in the larger grains. Shear texture or weak texture is found in the surface of Figure 3.1a. This correspond well to the texture in Figure 3.1b.

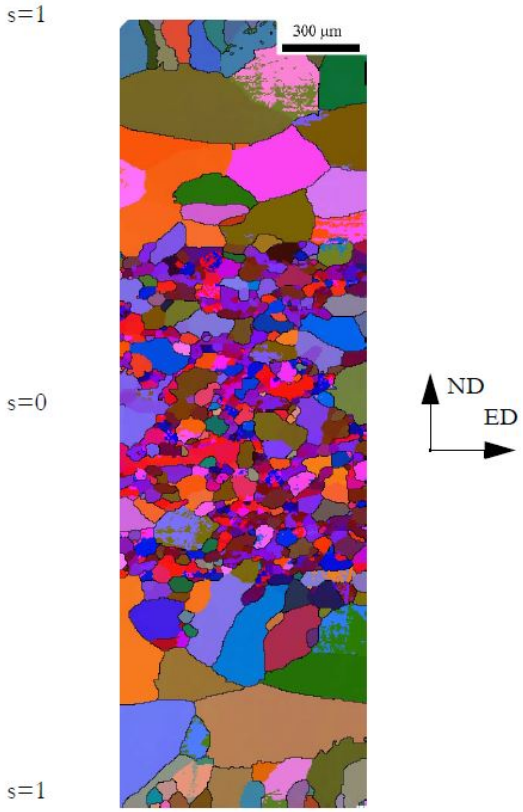

(a)

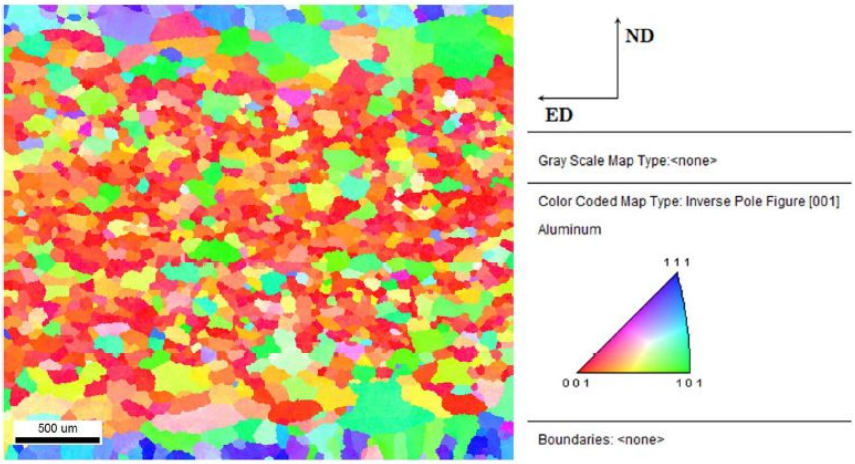

(b)

Figure 3.1: (a) EBSD map showing grain structure of a flat AA6063 profile, through thickness. TD is used as the projection axis, from Ryen[43]. (b) IPF map of AA6063, TD as the IPF axis, from Khadyko et al.[30].

3.4 Precipitation structure

In Khadyko et al.[30] and a newer article Khadyko et al.[31], AA6063 in T1, T6, T7 and O tempers are investigated. Both T6 and T7 contain needle-like precipitates[30]. These precipitates have a very strong effect on the strength, and the flow stress anisotropy in the tempers is expected to be affected by precipitates[30]. T7 has the largest precipitates and a large percentage are

expected to be non-shearable[30]. O temper contain large plate-like precipitates, and the flow stress anisotropy of both O and T1 are expected to be little affected of precipitates[30]. PFZ were also observed in T6 and T7, where T7 had a zone twice as big as T6[30]. T1 was not investigated in TEM by Khadyko et al.[30] because T1 contain mostly clusters and GP-zones. After the extrusion, the profile is stretched 0.5-1% strain in T1, as a part of the standard procedure. Ekström et al.[10] observed a significant number of dislocations in T1 condition after the production, and this may have an influence on the plastic anisotropy[30].

Ryen[43] tested two types of tensile specimens of the extruded AA6063-W tensile specimen and the extruded AA7030-W tensile specimen. The two types have the same specimen geometry, but different thickness. One type is a "fat" specimen and the other type is a "thinned" specimen. In the "fat" specimen no alternations is performed to the original thickness of the profile. An AA6063-W "fat" specimens will contain the same structure as shown in Figure 3.1a. The cube texture is located in the middle followed by Goss texture and shear texture in the surface of Figure 3.1a. In the "thinned" specimens layers of shear texture and Goss texture are removed by polishing, and the tensile specimen will only consist of the cube texture.

Ryen[43] studied the development of dislocations during tensile testing of "thinned" AA7030-W specimens. The initial microstructure in both 0°and 90°to ED are similar. After 8% straining in the 0°direction dislocation structure has developed in some grains, while other remain dislocation free[43]. After 8% straining in the 90°direction the development of the dislocation structure is much more diffuse than in 0°direction, and more homogeneous distributed in the grains. The 0°specimen failed right after 8% strain, and the 90°specimen was strained to 15% strain. After 15% strain the 90°specimen experienced a dislocation structure more similar to the dislocation structure in the 0°specimen at 8% strain. The dislocation structure in 90°specimen after 15% straining was more homogeneously distributed than in the 0°specimen at 8% strain. EBSD measurements revealed small changes in texture during straining in both directions. In the 0°direction an increase of ED rotated cube was observed, meanwhile in 90°direction a decrease in this component was observed. This will be further discussed in Section 3.6.

3.5 Anisotropy

As mention earlier crystallographic texture is seen as the main contribution to plastic anisotropy of extruded and rolled aluminium alloys[31]. In this section strength anisotropy in the work of Chen et al.[7], Khadyko et al.[30] and Khadyko et al.[31] will be compared. This is followed by a discussion of anisotropy in the case of strain ratio and flow stress ratio. The anisotropic plasticity can change the stress state and the plastic flow of the material. This may lead to fracture anisotropy, which is analyzed in the last subsection.

Chen et al.[7] investigated the recrystallized alloy AA6060-T6, which showed slightly strength anisotropy. The 90°direction experienced a larger yield strength than the 0°and 45°direction. Khadyko et al.[30] tested extruded AA6063 in T1, T6, T7 and O in five directions, 0°, 22.5°, 45°, 67.5°and 90°. AA6063-T6 in Khadyko et al.[30] experienced the highest yield strength in the 45°direction. Khadyko et al.[30] experienced more anisotropy in AA6063-T6 than AA6060-T6 from Chen et al.[7]. In comparison tested Chen et al.[7] three directions. Since Khadyko et al.[30] tested two more directions than Chen et al.[7], the strength anisotropy in Chen et al.[7] can be underestimated. As the 22.5°direction in Khadyko et al.[30] seemed noticeable lower in strength than the other directions.

All the tested tempers in Khadyko et al.[30] showed the largest yield strength in the 45°direction, and the other directions follows in descending yield strength, 67.5°, 0°, 90°and 22.5°. All the tested tempers in Khadyko et al.[30] show approximately the same strength anisotropy. During the heat treatments to achieve the tempers the texture will not change. Texture is the main contribution to anisotropy, and this correspond well to the observations of the same strength anisotropy in the tempers. Because of this it is reasonably to assume that the observations of Khadyko et al.[30] and Chen et al.[7] also hold for T4.

Khadyko et al.[30] tested flow stress ratio, which is defined as $\sigma_\varphi/\sigma_{90^\circ}$, where φ is the chosen direction. Flow stress ratio was used to signify strength anisotropy for different tempers, and the results are replotted in Figure 3.2a. In Figure3.2a the tempers produce significant variations between the 0°and 22.5°directions, and some variation after 22.5°[30]. As mentioned in Section 3.4 T6 and T7 have a very different precipitation structure than O and T1, and T6 and T7 were expected to be more influenced by precipitates regarding flow stress. In Figure 3.2a the T6 and T7 temper are close to each other, as expected since T6 and T7 experience very similar precipitation structure.

The plastic flow anisotropy can be described by strain ratio. The strain ratio is expressed as $q = -\frac{d\epsilon_y}{d\epsilon_x}$. By assuming negligibly small elastic strains and plastic incompressibility, a relation between q and r can derived.

$$r = \frac{q}{1-q} \tag{3.1}$$

The strain ratio has been investigated by Khadyko et al.[30] for different tensile directions and heat treatments in AA6063. The results are replotted in Figure 3.2b. The variations in tensile direction and temper are small compared to flow stress ratio[30] described in the section above. Meanwhile the 45°direction marked significant variation in strain ratio to temper. In Ryen[43], r-value is used to express the strain ratio. The material used in Ryen[43] is an extruded AA6063 alloy in W temper. When comparing the r-values in [43] to calculated r-values from Khadyko et al.[30] (through Equation 3.1). The results coincide very well. This strengthens the observations of a plastic anisotropy more independent of temper.

Choi et al.[8] investigated a recrystallized binary Al-3 wt pct Cu alloy and observed that the flow stress ratio was less affected by the precipitates than the strain ratio. For all directions the strain ratio in Khadyko et al.[30] (AA6063), except the 45°direction, showed the same behaviour independent on precipitation content or heat treatment (Figure 3.2b). This is unlike the observation for the recrystallized binary Al-3 wt pct Cu alloy in Choi et al.[8]. Al-3 wt pct Cu alloy contain {100} platelet shaped precipitates, while AA6063 contain needle shaped precipitates. This can contribute to the dissimilar observed flow stress behaviour. All tempers in Khadyko et al.[30] (T1, T6, T7, O) experience similar plastic anisotropy, but not identical (Figure 3.2b). Khadyko et al.[30] concluded that the small differences existed due to the different heat treatments. These differences cannot alone be explained by the presence or absence of precipitates, as in AA2xxx and AA7xxx alloys[30].

The experimental values for strain ratio in Khadyko et al.[30] differ from the values predicted by a crystal plasticity finite element model (CP-FEM) for the tensile testing. The CP-FEM is mainly texture-based, and managed to predict the overall variations. Depending on tensile direction the quantitative accuracy varies, and the experimental values differ from the modelled. Since the texture-based model can describe the experimental behaviour to a certain accuracy, heat treatments must affect the plastic anisotropy. Khadyko et al.[30] concluded that the developed microstructure trough the heat treatments (not just limited to precipitates) affected the plastic anisotropy. This conclusion was based on TEM and mechanical testing.

Ryen[43], by using the Taylor-RC model, predicted the r-values of AA6063-W with good accuracy. On the other hand, the model clearly overpredicts the r-value in the 90°direction[43]. Ryen[43] suggested that the strong Goss structure, described in Section 3.3 and Figure 3.1a, gave very high calculated r-values by the Taylor RC-model. The Taylor-RC model suggests three independent slip systems necessary to achieve plastic deformation[43]. The Taylor FC-model suggests five slip systems, but in Ryen[43] it overpredicted the maxima in at the 0°and the 90°directions for AA6063. Ryen[43] found the same observations as Iveland[27], Søreng[46] and Fjeldly[49] in AA7xxx alloys. Iveland[27] reported underpredicted r-values by the Sachs model, which uses two independent slip systems necessary to achieve plastic deformation. Based on this Ryen[43] assumed two or three slip systems are activated during tensile deformation.

3.5.1 Fracture anisotropy

In Figure 3.2c the fracture anisotropy of Khadyko et al.[31] is replotted. The observed fracture anisotropy in AA6063 is independent of the heat treatment. The fracture strain was measured as the average logarithmic strains in the locally neck area onset of fracture in tensile testing, using a DIC method. Specimens used in the tensile testing were of a "dog-bone" type with a gauge cross section of 3mm x 8mm and length of 35mm. Both ends were bolted during tensile testing. The fracture strain observed in Khadyko et al.[31] was largest in the 90°direction and observed to be lowest in the 45°direction. The T1 and T6 temper were also reported to have a local minimum for the 0°direction[31] (Figure 3.2c).

A strong linear trend between the average logarithmic tensile strain in the neck area at fracture and the true stress onset of necking, was observed by Khadyko et al.[31]. Larger true stress gives decrease in average logarithmic tensile strain. Heat treatments will change the precipitation content, as seen in Section 3.4, and either increase or decrease the stress at necking. By the linear relation the change in precipitation content will lead to decease or increase of the average logarithmic fracture strain, by increase or decrease the stress onset of necking.

Khadyko et al.[31] observed a complex behaviour for the 0°direction, and the 0°direction will be described in more detail in Section 3.6. Khadyko et al.[31] assumed primary particles had no effect on the fracture anisotropy, since primary particles were not found to form stringer structure. Thereby Khadyko et al.[31] concluded that the fracture anisotropy is mainly governed by the plastic anisotropy introduced by the extrusion process and the recrystallization.

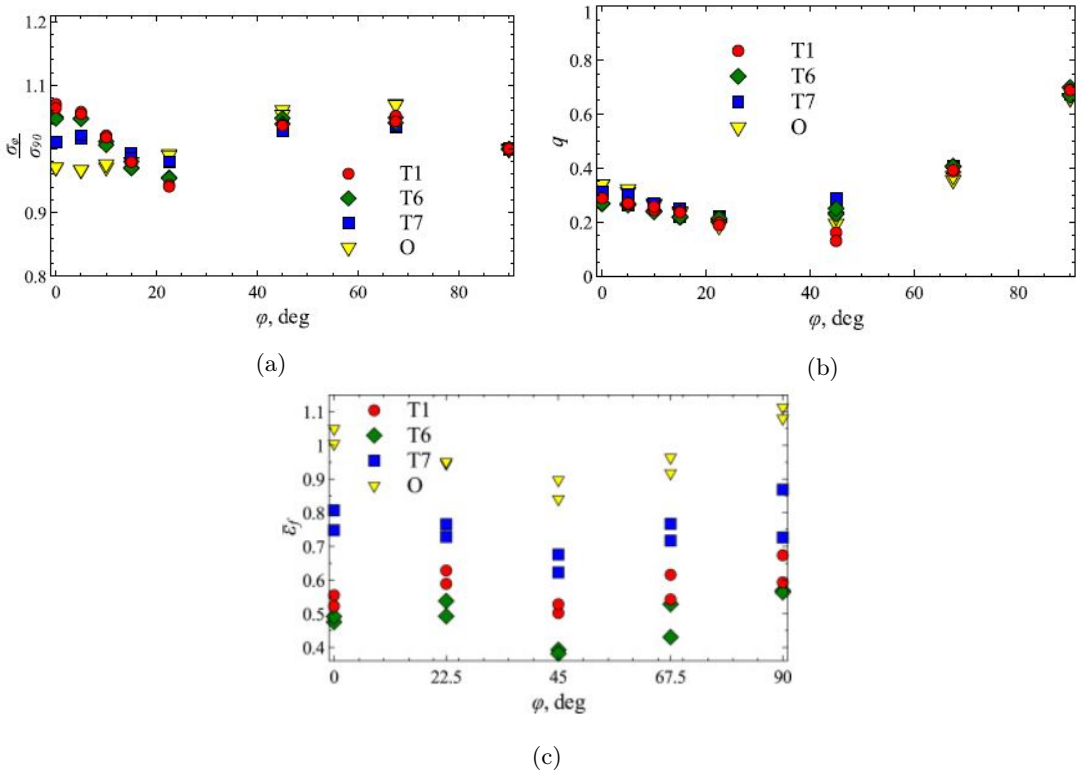

Figure 3.2: The subfigures are replotted from Khadyko et al.[30]. (a) shows the flow stress ratio $\sigma_\varphi/\sigma_{90}$ plotted against tensile direction. (b) shows the strain ratio $q = -\frac{d\epsilon_y}{d\epsilon_x}$ plotted against tensile direction. (c) shows the average logarithmic tensile strain in the neck area at fracture plotted against the tensile direction.

Fracture anisotropy was observed in AA6063 tensile tests for all tempers in Khadyko et al.[31]

(Figure 3.2c). In Chen et al.[6] extruded AA6060-T6, AA6082-T6, AA7003-T6 and AA7108-T6 were investigated through tensile testing and instrumented Charpy V-notch testing. Fracture strains in the tensile testing are measured as logarithmic fracture strain, $\epsilon_f = \ln(A_0/A_f)$, measurements are obtained through microscope. In the instrumented Charpy V-notch testing, the impact load is measured at the tip of the striker and by cemented strain gauges. Both a force-displacement and an energy-displacement curve is calculated from the measurement. Directional dependency for tensile fracture strain is found for AA6060-T6, but a similar directional dependency in the max force per unite thickness in Charpy test result was not found. Chen et al.[6] concluded that the reason for the lack of directional dependency was that the energy absorption per thickness is approximately the same for all the tested directions (AA6060-T6) by the Charpy testing.

3.6 Work hardening

Ryen[43] observed variations in work hardening of the recrystallized alloys AA6063 and AA7030 in W temper, compared the fibrous AA6082 and AA7108 also in W temper. The observed variations of work hardening in Ryen[43] are replotted in Figure 3.3. Large variations in hardening rates with tensile directions are observed in AA6063-W (Figure 3.3a) and AA7030-W (Figure 3.3b). In both alloys the 0°stands out with rapid hardening up to 5% strain in the stress-strain curve, and then flattens out to low hardening. This is not observed in AA6082 and AA7108. This can remind of an anisotropy in strain hardening, and as mentioned earlier texture is often the considered the main contribution to plastic anisotropy. The definition of "thinned" and "fat" specimens are explained in detail in Section 3.4. The "fat" tensile specimens contain the original thickness of the profile, and the "thinned" specimens only contain the cube texture. In Ryen[43] "thinned" specimens were made in order to get tensile specimens only containing the cube texture. This gave the samples a much more homogeneous microstructure, but it did not cause any significant changes to the strange shape of the 0°curve and the strength of the alloy. This can indicate that the texture is not the main cause to the distinct behaviour of the 0°direction. Reduction of thickness leads to reduced elongation in 0°and 45°for both alloys, as seen in Figure 3.4.

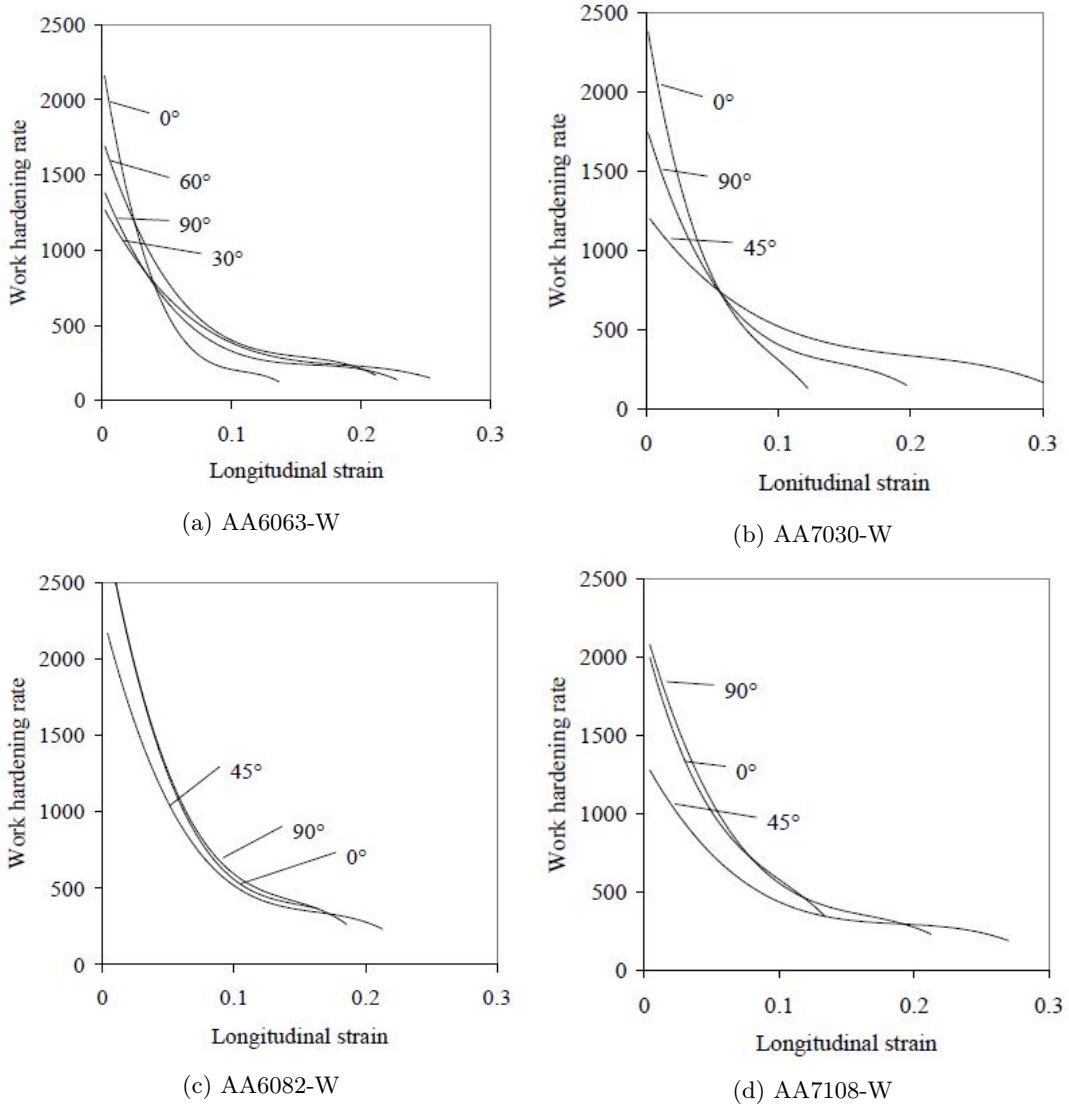

(a) AA6063-W

(b) AA7030-W

(c) AA6082-W

(d) AA7108-W

Figure 3.3: Work hardening rates in 0°, 45°and 90°direction, from [43].

The Taylor FC and RC model were used in Ryen[43] to predict M-values (Taylor factors), and the results were compared to the experimental results. M refers to Taylor factor in this context, defined as the ratio between the shear strain increments on the slip systems and the global strain increment on the crystal[43]:

$$M = \frac{\sum_s |\dot{\gamma}^s|}{\dot{\epsilon}} = \frac{\sigma}{\tau_c} \tag{3.2}$$

where $\dot{\gamma}^s$ is the slip rate on slip system s, $\dot{\epsilon}$ is the strain rate, σ is the applied stress and τ_c is the critical shear strain[43]. In the comparison to experimental data all values were normalized to either 0°or 90°, and the best fit was achieved when normalized to 90°. Ryen[43] concluded that this was partly due to the distinct behaviour of the 0°direction. Because of the better fit to 90°, at that point in time the mathematical models were assumed to not be capable of accurately describe the behaviour of the 0°direction. After straining "thinned " AA7030-W specimens in the 0°direction, the grains that exhibit the most distinct substructure are oriented off the cube orientation. This is not observed in the 90°direction and can be one of the reasons for the differences seen between the 0°and 90°directions.

Stress-strain curves of "thinned" and "fat" AA6063-W and AA7030-W specimens are given in

Figure 3.4. The stress-strain behaviour of the "thinned" and "fat" specimens are quite similar despite removal of Goss and shear layers to get more homogeneous texture. This indicates that other factors than the texture may affect the directionality of the properties. Ryen[43] explained the strong hardening in the 0°direction by concentrated slip activity presented as rapidly developed microbands during tensile testing. This is also observed in AA7030 by Søreng[46]. Ryen[43] discussed the possibility for anisotropic solid solution hardening. The anisotropy of strength is approximately unaffected by the solution heat treatment, unless the precipitates create a directionality of properties that are equal to the directionality of the solutes create. This is however not very likely.

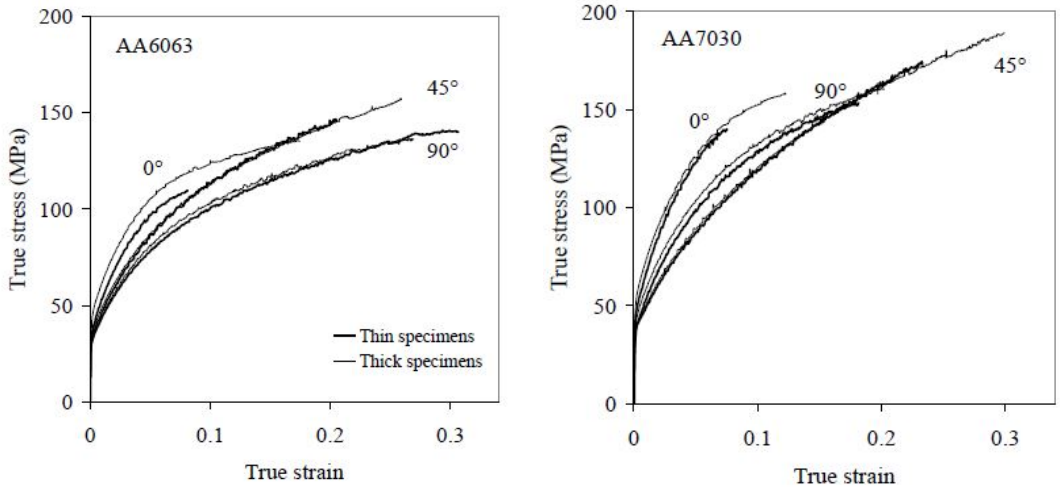

(a) AA6063-W

(b) AA7030-W

Figure 3.4: Stress and strain curves of thick and thin specimens in 0°, 45°and 90°direction, from [43]

3.7 Fracture

One fracture mode observed in aluminium is ductile failure mode, which is governed by necking and rupture[39]. Two of the theories used to describe ductile fracture in aluminium alloys are the damage accumulation theory and the nano-void theory[39].

Damage accumulation is based on nucleation, growth and coalescence of micro-voids[39]. Inclusions and second phase particles, like precipitates, constituent particles and dispersoids, already exist in the matrix. These are favorable sites for damage initiation through nucleation of micro-voids[39]. The micro-voids nucleate heterogeneously at the favorable sites in the matrix[39]. By plastic deformation and induced stress triaxiality the micro-voids will grow in size. At a stage in the plastic deformation local necking instabilities are promoted by a concentration of plastic strain along a sheet of voids[39]. This trigger void coalescence, which lead to formation of macroscopic cracks and failure[39].

The nano-void theory is based on generation of point defects, nano-void formation and growth[39]. In this theory point defects are generated dynamically with deformation[39]. The point defects are generated within the mean volume element of an associated nano-void nuclei, and the nuclei grow with the accumulation of the point defects[39]. Nano-void nuclei is formed at grown-in nano particles[39]. The nano-voids continue growing with deformation, and leads to coalescence of nano-voids and failure[39].

Muhammad et al.[39] purposed a constitutive model that extended the nano-void theory to precipitation hardened aluminium alloys. The model was able to predict fracture strain from

tensile loading. AA6061-T6 rolled sheet, extruded AA6063-T6 and AA6082-T6 profiles are subjected to tensile testing to calibrate and validate the proposed model. Effects of dynamic microstructure evolution due to the deformation and precipitation induced cellular dislocation substructure have been incorporated in the model by Muhammad et al.[39]. The purposed model has been successful in predicting fracture strain in ED, TD and 45°in rolled AA6061-T6, and extruded AA6082-T6 and AA6063-T6. The modelled results correspond well to the experimental results with an error less than 7%[39], even though all alloys have very various starting microstructures.

The nano-void coalescence, which lead to failure, is dependent on the rate at which point defects are being generated. The volume fraction of deformation induced point defects C_v, for an arbitrary shear strain interval between γ_1 and γ_2, is expressed in Muhammad et al.[39] as:

$$C_v = \frac{X}{N_0 b^3}\left(\frac{P}{4A}\right)(2+\beta)\frac{\gamma^2}{2}\Big|_{\gamma_2}^{\gamma_1} \tag{3.3}$$

where X is a function of the crystallographic texture, N_0 is $6.026 \times 10^{28} m^{-3}$ for polycrystalline aluminium, b is burgers vector, P/A and β are microstructural parameters determined from stress-strain data and γ is the shear strain[39]. By using Equation 3.3 the volume fraction of point defects along different loading directions can be calculated, and this is performed in Muhammad et al.[39]. In AA6061-T6 the production rate of point defects is highest in TD and lowest in 45°, and this corresponds to highest fracture strain in 45°and lowest in TD. AA6082-T6 and AA6063-T6 both have the highest rate of point defects in ED. AA6082-T6 had the lowest in 45°, which gave highest fracture strain in 45°and lowest in ED[39]. AA6063-T6 was not tested in the 45°direction in Muhammad et al.[39], and this gave highest fracture strain in TD and lowest in ED. The result of AA6063-T6 correlate with the results by Khadyko et al.[31] (seen in Figure 3.2c). Equation 3.3 is based on a model, and the volume fraction of point defects is very difficult to measure. This makes the equation difficult to validate.

3.7.1 Fracture surface

Ductile fracture of commercial aluminium alloys is controlled by the primary- and the secondary voids, which can be nucleated at cracked constituent particles, at decohered dispersoid or inclusions[35]. Ductile fractures are characterized by dimples, and dimples are found during investigation of the fracture surface in the discussed AA6063 (T1, T6, T7, O) in Khadyko et al.[31], and in AA6060-T6 in Chen et al.[6]. The fracture surface of the different heat treatments in Khadyko et al.[31] have different dimple sizes. O temper experiences the highest fracture strain (Figure 3.2c) and show the largest dimples. While T1, T6 and T7 are more similar in dimple size[31]. The fracture surface of T6 and T7 differ from T1 by flat areas, where the grains are separated along the grain boundaries. This is probably caused by the precipitate free zones in T6 and T7. Even though T6 and T7 have proven to have very similar fracture surface, they experience quite different fracture strain. T1 and T6 are closer in fracture strain than T6 and T7 (Figure 3.2c), but T1 and T6 have a more dissimilar fracture surface than T6 and T7.

The shape of the fracture surface cross-section is a result of the materials plastic anisotropy[31], and the intensity of the cross-section varied with temper in Khadyko et al.[31]. In Khadyko et al.[31] the portion between the width and thickness of the fracture surface was largely influenced by the strain ratio. As seen in Khadyko et al.[31], the strain ratio varies with tensile direction (Figure 3.2b). Regarding features in the fracture surface, the different directions to ED were all quite similar in Khadyko et al.[31].

In Chen et al.[6] AA6060-T6 was investigated using an instrumented Charpy test machine and V-notch specimens. More details of Chen et al.[6] are given at the end of Section 3.5.1. The fracture surface of AA6060-T6 was similar to the T6 fracture surface in Khadyko et al.[31]. Chen et al.[6] also found, using Charpy V-notch, that direction to ED did not impact the result of the recrystallized alloy, like Khadyko et al.[31] found using tensile testing. Meanwhile in the fibrous alloys in Chen et al.[6], solid horizontal fracture lines through the fracture surface are observed

in the 90°direction and not in the 0°direction. In the 0°direction the V-notch in the specimens and thus the crack growth is normal to ED, and a solid horizontal fracture lines are therefore not visible. The recrystallized alloy in Chen et al.[6] has equiaxed grain structure, and thereby show little variation in fracture surface to different directions (regarding Charpy V-notch testing).

3.7.2 Constituent particles contribution in fracture

Constituent particles are assumed to play an important role in determining ductility in aluminium alloys[48]. Both the volume fraction and size distribution of constituent particles are the major factors influencing the strain to failure[48]. In Thomesen et al.[48] stress-strain behaviour and fracture mechanisms were investigated in extruded AA6061, AA6063 and AA6110 in T6 temper. The tensile testing in Thomesen et al.[48] is performed with circular "dog bone" type specimens, and the fracture strain is calculated after failure by logarithmic strain defined by $\epsilon = \ln(A_0/A_f)$. Both AA6110-T6 and AA6061-T6 are characterized as high strength aluminium alloy and AA6063-T6 is characterized as medium strength aluminium alloy. As explained early in Section 3.5.1 Khadyko et al.[31] reported a linear relation between the yield stress and the failure strain of different aluminium alloy. This is also reported in [35, 36, 52]. Both AA6110-T6 and AA6061-T6 are high strength, with the yield strength at the same level. It is expected that the measured logarithmic fracture strain is at the same level, but this is not the case in Thomesen et al.[48]. AA6061-T6 experiences fracture strain at the same level as medium strength aluminium alloy AA6063-T6[48]. Thomesen et al.[48] concluded that this larger fracture strain was achieved because AA6061-T6 contain constituent particles of a smaller size than AA6110-T6. The measurement of constituent particles are based on area measurements. The particle fraction of constituent particles are lower in both AA6063-T6 and AA6061-T6 compared to AA6110-T6[48]. The size of the constituent particles are also smaller for AA6061-T6 compared to the other two alloys. The sizes and fractions of constituent particles in Thomesen et al.[48] are obtained through image processing of backscattered electron micrographs.

Almost twice as large grains are observed in AA6061-T6 in Thomesen et al.[48] compared to the other two alloys. Larger grains are expected to have a bad influence on fracture strain[48]. The lower particle fraction and size of the constituent particles in AA6061-T6 seams to compensate for the larger grains. In addition the constituent particles also contribute to better fracture strain than expected based on the yield strength[48]. Hannard et al.[17] has reported similar results regarding constituent particles and fracture strain as Thomesen et al.[48].

3.8 Strain rate dependency of 6xxx alloys

The elongation to fracture of AA6xxx alloys are observed to be dependent on strain rate at temperatures of 250-350°C[34]. The tensile testing in this report is performed at room temperature and Cavusoglu et al.[5] investigated the dependency of strain rate in AA6xxx alloys at room temperature. AA6061-T4 and AA6019-T4 rolled sheet materials were subjected to tensile testing at room temperature with strain rates: $0.3\,s^{-1}$, $0.03\,s^{-1}$, $0.003\,s^{-1}$, $0.0003\,s^{-1}$, $0.00003\,s^{-1}$. The tensile specimens were prepared according to ASTM E517, with a "dog-bone" type specimen geometry. Both AA6061-T4 and AA6019-T4 are recrystallized (confirmed through light optical investigations), but a texture analysis is not performed in Cavusoglu et al.[5].

The yield strength, tensile strength and elongation were obtained from stress-strain curves in Cavusoglu et al.[5]. The lowest value of yield and tensile strength are obtained at the lowest strain rate ($0.00003\,s^{-1}$) for both AA6061-T4 and AA6019-T4. The yield and tensile strength slightly in both alloys increase with strain rate[5].

In Figure 3.5 the results of Cavusoglu et al.[5] are replotted. In this figure different behaviours are observed for AA6061-T4 and AA6019-T4. Elongation of AA6019-T4 is unaffected by the changes in the range of strain rates: $0.3\,s^{-1} - 0.0003\,s^{-1}$. Meanwhile for strain rate $0.00003\,s^{-1}$ AA6019-T4 experiences a minimum value. According to Cavusoglu et al.[5] AA6061-T4 experienced a negative trend in elongation with increasing strain rate. The difference in elongation level

between the two alloys is caused by a higher yield strength in AA6019-T4[5]. Cavusoglu et al.[5] concluded that the AA6061-T4 and AA6019-T4 rolled sheets are insensitive to strain rate, because of a narrow exchanged rate of the elongation and the plane anisotropy.

An extruded AA6063-T4 profile is the objective of this report, and the texture of this profile is assumed to be different than the rolling texture of AA6061-T4 and AA6019-T4 (texture of these profiles were not investigated). Extruded AA6060-T6, AA6061-T6 and AA6082-T6 are also reported to be approximately insensitive to strain rate[7, 9, 14]. The rolling texture in T4 was not affected by the strain rate, neither were the extrusions textures in T6. Strain rate is more dependent on temper than alloy, and based on this it can be reasonably to assume that the extruded AA6063-T4 also is approximately insensitive to strain rate.

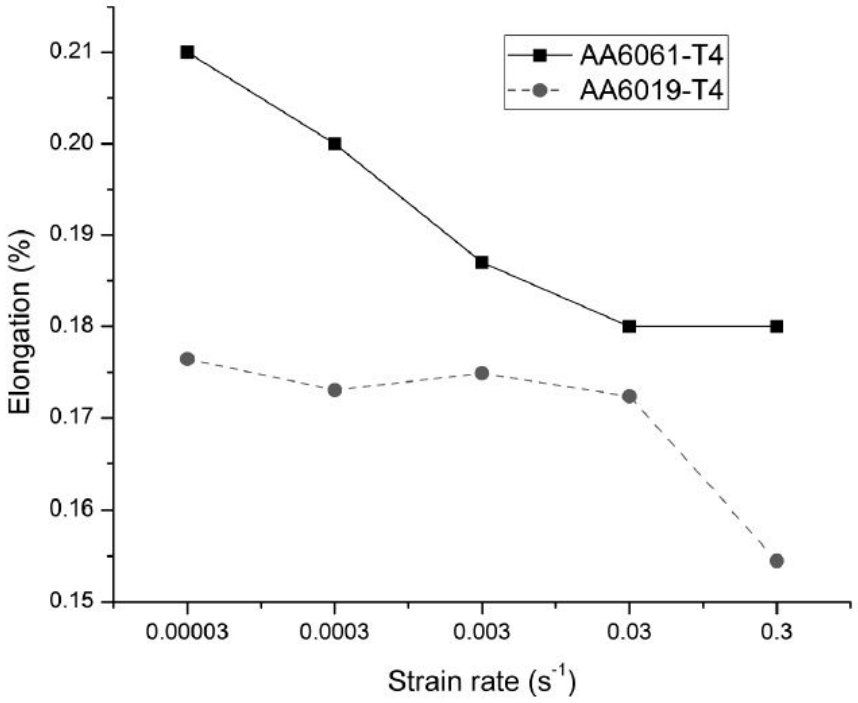

Figure 3.5: Strain rate vs. elongation in AA6019-T4 and AA6061-T4 from [5].

4. Method

The experimental work is a continuation of the author's project thesis from the autumn of 2019. In the project thesis extruded AA6063 samples were solution heat treated (SHT) and then quenched with four different cooling rates: Water, air, oil and cooling between two Al-plates. The SHT consisted of heating the received material at 550°C for 20 minutes in a salt bath. In the further experimental work water, oil and air cooling will be continued. In this chapter all started experimental work is described, also the aborted work, due to the outbreak of the coronavirus and the closing of NTNU.

4.1 Material and extruded profile

The material used in this report is the aluminium alloy AA6063 it is the same as the material used in the author's project thesis. The exact chemical composition and measurements of the material can't be given due to confidentiality. The material is supplied by Hydro and extruded at Hydro Extruded Solutions Tønder, Denmark. The extruded profile is illustrated in Figure 4.1a. The orientations of the profile are also defined, which are referred to in further experimental work. All the samples used in the experimental work are taken in the position indicated in Figure 4.1a. For practical reasons in the experimental work, a system for addressing the sample is defined in Figure 4.1c.

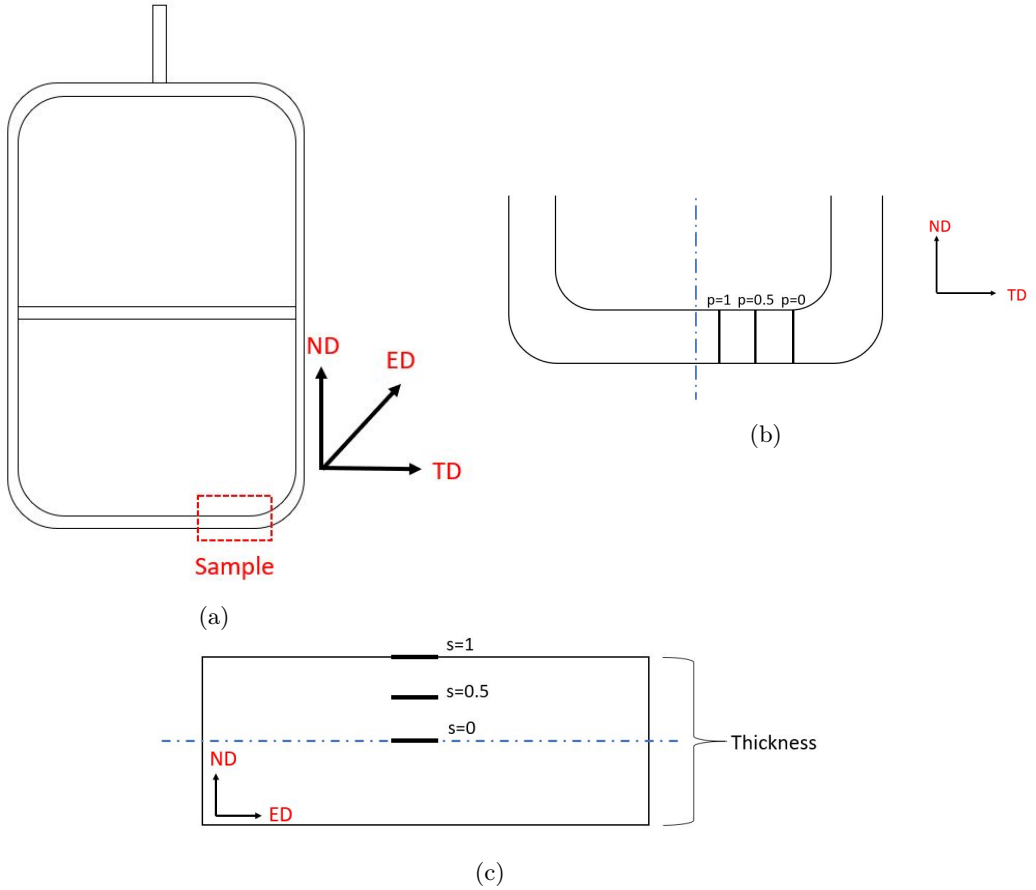

Figure 4.1: Systems for defining orientations and positions in: (a) the extruded profile, (b) the sample in ND-TD plane and (c) the sample in ND-ED plane. In (b) p is used to define positions in the TD-ND plane of the sample. p=0 close to the corner of the profile, p=0.5 approximately midway between corner and central axis and p=1 close to the central axis of the profile. In (c) t is used to define positions in the ND-TD plane of the sample, t=1 refers to the surface and t=0 refers to a position along the central axis.

4.1.1 Measuring of cooling rates

The cooling rates are measured from solution heat treatment at 550°C to room temperature. The temperature data are logged by dataTaker DT80, with a logging interval of 200ms. The temperature is measured by a k-type thermocouple, and the thermocouple setup is shown in Figure 4.2. Because of the chemical composition of the thermocouple it cannot be welded to the sample. That would have created a different alloy in the weld and the temperature would not be measured correctly.

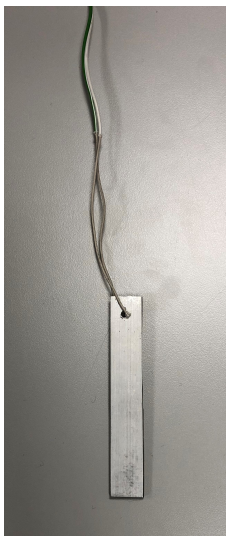

Figure 4.2: setup of thermocouple to measure cooling rates, the two threads in the thermocouple is welded together through a hole in the sample.

4.2 Tensile testing

Tensile testing of specimens subjected to water and air quenching from the SHT were performed in the author's project thesis in autumn of 2019. Just after quenching half of the tensile specimens were stretched 0.5% plastic strain and then stored at room temperature for 24 hour and 7 days before tensile testing in T4 condition. These tensile specimens will further in this report be referred to as pre stretched. The rest of the tensile specimens were not stretched 0.5% plastic strain after quenching, and these specimens will be referred to as not-stretched.

Measuring and calculation of the area based fracture strain

The fracture surface area of the tensile specimens are measured (in the spring of 2020) after tensile testing in the autumn of 2019. The area after fracture is impossible to measure by the extensometer during tensile testing, because it is hard to predict exact position of the fracture and the fracture shape is not symmetrical. The fracture area is measured by image processing. High resolution images of the fracture surface are taken with Leitz Wild Photomakroskop M400 using software ZEN 2 core v2.4 in free examination mode. The images are taken with the normal of the fracture surface parallel to the tensile axis. A Matlab script, given in appendix B, is used to measure the projected area by counting pixels within the fracture surface area, A_f. Equation 2.20 is used for calculation of the area based fracture strain.

4.2.1 Strain rate in tensile testing

To investigate strain rate sensitivity, tensile testing with five strain rates was planned. The specimen geometry used in the tensile testing is given in Figure 4.3. The specimen geometry is different from the one used in the author's project thesis. The specimen geometry from the project thesis proved to be challenging in getting stable testing results regarding breaking within the extensometer. To try to avoid this problem in the present tensile testing, a specimen geometry with a gauge length more similar to the extensometer length is chosen. The tensile testing is performed on a MTS 810 tensile testing machine, and with the strain rate of $10^{-5}s^{-1}$, $10^{-4}s^{-1}$, $10^{-3}s^{-1}$, $10^{-2}s^{-1}$ and $10^{-1}s^{-1}$. Before testing, the specimens were SHT for 20 minutes at 550°C in a salt bath and stored at room temperature for approximately 24 hours after cooling. Due to the outbreak of the coronavirus and the closing of NTNU this work was never finished. The specimens were machined, but never tested.

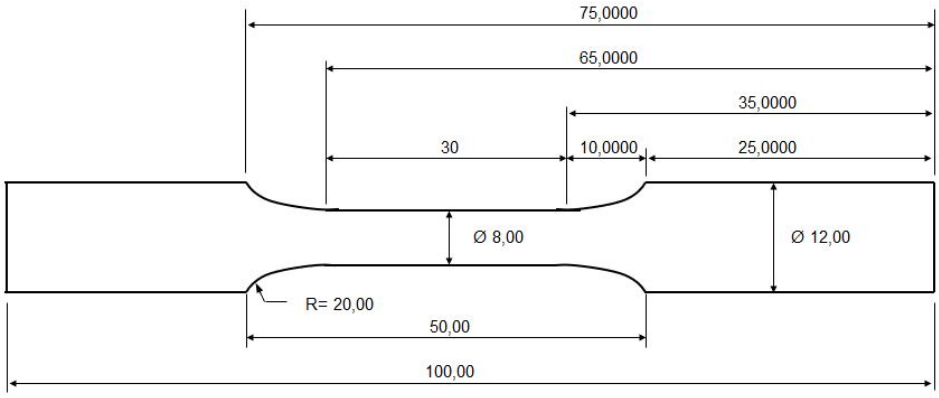

Figure 4.3: Specimen geometry for tensile testing, measurements given in mm.

4.3 SEM

The FESEM Zeiss Ultra 55 limited edition scanning electron microscope (SEM) is used for investigating fracture surfaces and texture. Preparation for texture investigations involved casting the samples in EpoFix, and grinding and polishing down to 1μm. Then the samples are vibration polished in Buehler Vibramet 2 with an amplitude of 70% for one hour. No sample preparation was performed regarding the fracture area samples, they were only put in a chamber for degassing prior to the investigation.

4.3.1 Fracture surface from previous tensile testing

The tensile specimens from Section 4.2 were investigated in the scanning electron microscope. All analyzes are performed in high current mode and with an acceleration voltage of 10kV. Images of the fracture surface are taken with the Zeiss secondary electron detector (SE detector). The aperture is set to 30μm and a working distance of approximating 25 mm is used. Images are taken at magnification 200X, 500X and 2000X.

Material characterization of particles found in the fracture surface is performed by energy-dispersive X-ray spectroscopy (EDS) with a Bruker AXS XFlash Detector 4010. In these analyzes the aperture is set to 60μm and the working distance of approximately 10 mm is used. For better accuracy a high magnification of approximately 2000X is used. The data processing is performed in Bruker AXS Esprit 1.9 data program.

4.3.2 EBSD analysis

The extruded material in as-received condition is subjected to texture- and microstructure analyzes by EBSD. The SEM used and sample preparation are explained earlier in section 4.3. The samples are cut out in the ND-TD plane in the "sample position" in Figure 4.1a on Labotom-5. The EBSD scan is performed through thickness of the profile and in the p=0.5 position in Figure 4.1b. One through thickness scan is performed at the start of one profile, called sample S1. Another scan is performed 5cm into the profile in the ED-direction, in the same position as the first scan, and this scan is called S2. The purpose is to be able to compare the scans.

The settings used during the EBSD analyzes are given in Table 4.1. The Kikuchi pattern is detected by an Nordif EBSD detector. TSL OIM data Collection 7 is used for indexing the pattern in retro spect, and TSL OIM Analysis 7 is used for post processing of the results from the indexing.

Acceleration voltage	20keV
Aperture	$300\mu m$
"beam current"	High current mode
Magnification	200X
Tilt angle	70°
Working distance	Approximate $26mm$

Table 4.1: Settings used in EBSD with Nordif EBSD detector at the Zeiss Ultra 55 limited edition FESEM.

Sample S1 is scanned through thickness with 4 EBSD scans. An area of 380×410 is scanned in each scan, with a step size $3\mu m$. Sample S2 is scanned through thickness with 4 EBSD scans. The scans are performed with a step size $3\mu m$. The sample is cast in epoxy, and since the epoxy does not electrically conductive, the first and end scan are started approximately $0.5mm$ from the epoxy to avoid disturbances in the SEM image.

4.4 Natural ageing curves

The samples used to make the NA curves are cut on Labotom-5 according to Figure 4.4 and in the "sample position" from Figure 4.1a. The hardness indents are taken where p=0.5 and s=0 positions cross, as indicated in Figure 4.4. The indents will be taken in a line along s=0. In order to get good indents from the hardness measurements, the samples were grinded and polished before heat treatment.

The heat treatment consisted of heating the sample at 550°C in a salt bath for 20 minutes. Water, air and oil are used to quench the samples, and then the samples are stored at room temperature. Hardness indents are performed according to table 4.2, and along the s=0 position. Hardness is measured by Zwick ZHV10-A. The sample are divided into 6 different zones and one indent is made in each zone every measurement time (table 4.2). This is done in order to minimize statistical error and get a systematic hardness indent taking. This work also had to be aborted due to hardness machine breakdown, and was never redone due to closing of NTNU.

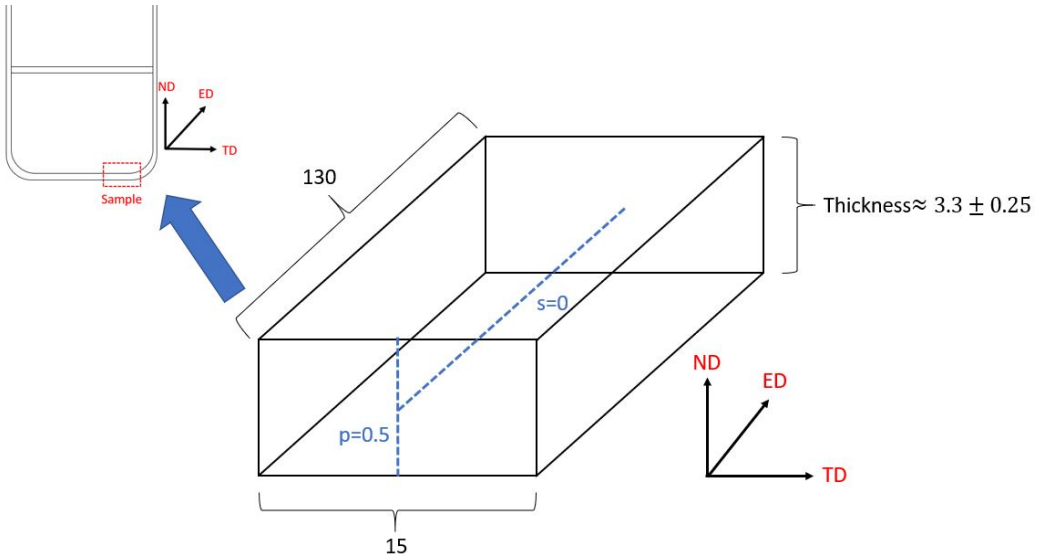

Figure 4.4: Measurements of sample used for making NA curves, p=0.5 position comes from Figure 4.1b and s=0 comes from Figure 4.1c. Measurements are given in mm. The NA sample is taken in the position of extruded profile as indicated in the left corner of the Figure.

Time after cooling[h:min]
0:15
0:40
1:30
06:00
12:00
31:00
79:00
119:00
151:00

Table 4.2: Timetable to create the NA curves.

5. Results

5.1 Cooling curves

The cooling curves are measured in Figure 5.1. As expected, water has the fastest quenching, and the temperature is below 250°C in about 1 second. Oil has the second-best quenching with reaching a temperature below 250°C in 50 seconds. Air has the slowest and reach a temperature below 250°C in 1 minute and 38 seconds.

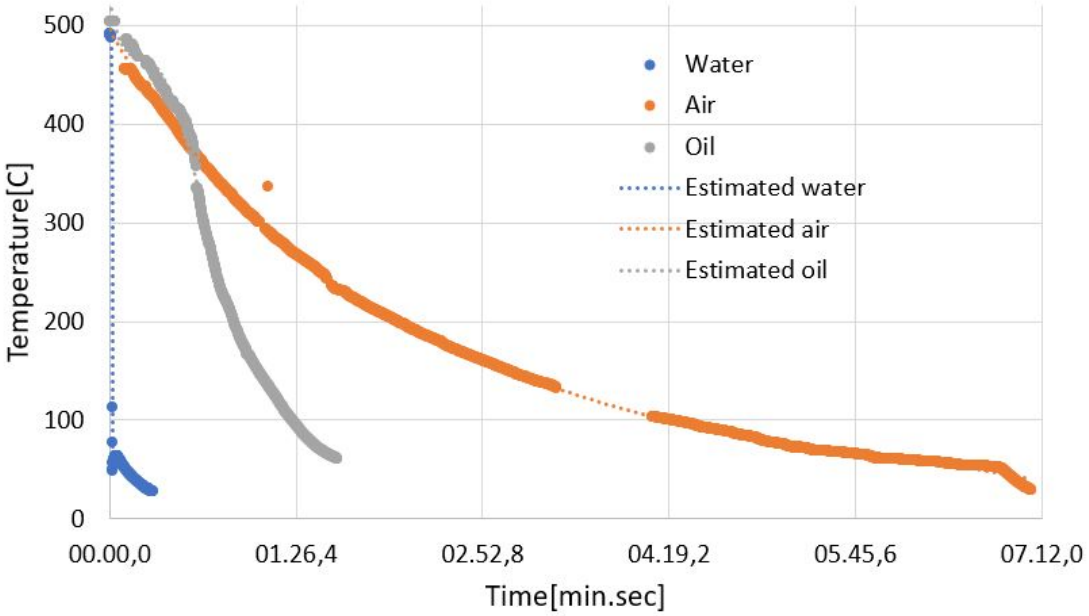

Figure 5.1: Cooling curves of SHT samples quenched in water, oil and air. SHT samples were heat treated at 550°C for 20 minutes in a salt bath before quenching.

5.2 Fracture strain by area fraction

The area fraction fracture strain of the tensile specimens used in the author's project thesis are calculated by Equation 2.20, and the procedure is explained in Section 4.2. The fracture area of a pre stretched air cooled tensile specimen stored for 24 hours at room temperature is shown in Figure 5.2. The area fraction fracture strain is measured to 1.039 in this figure. Fracture strain from the rest of the tensile specimens are found in Table 5.1.

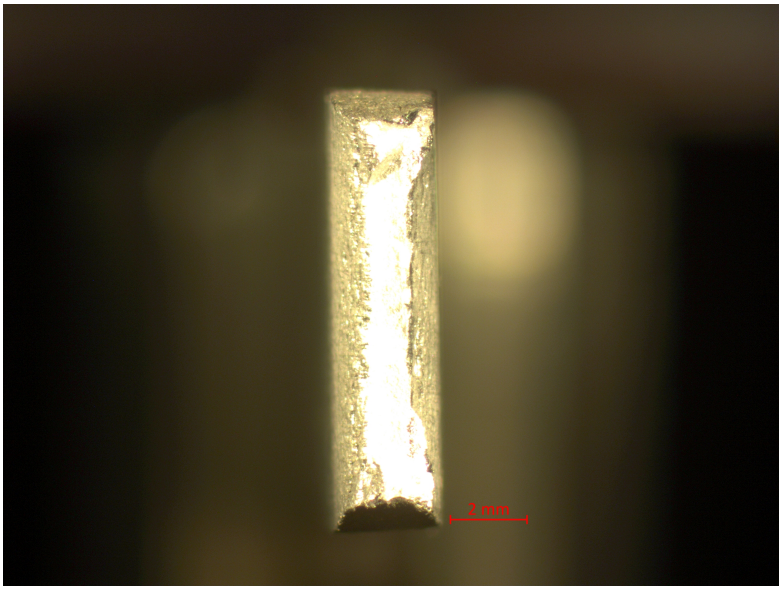

Figure 5.2: Maroscope image of the fracture area of an air cooled pre stretched tensile specimen with 24 hours storage at room temperature.

Sample	ϵ_f	Average	Difference between max value and min value
24h_A_1	0.979		
24h_A_2	1.262		
24h_A_3	1.039	1.093	0.283
24h_W_1	1.182		
24h_W_2	1.144		
24h_W_3	1.223	1.183	0.079
24h_AS_1	1.039		
24h_AS_2	1.044		
24h_AS_3	1.119	1.067	0.08
24h_WS_1	1.167		
24h_WS_2	1.021		
24h_WS_3	1.105	1.097	0,146
7d_A_1	0.914		
7d_A_2	1.025		
7d_A_3	1.013	0.984	0,111
7d_W_1	1.047		
7d_W_2	1.048		
7d_W_3	1.094	1.063	0.047
7d_AS_1	1.024		
7d_AS_2	1.008		
7d_AS_3	0.990	1.007	0.034
7d_WS_1	1.068		
7d_WS_2	1.104		
7d_WS_3	1.135	1.103	0.067

Table 5.1: Area fraction fracture strain of the tensile specimens from the author's project thesis. 24h in the first column refers to 24 hours of storage. 7d refers to 7 days of storage. A refers to air cooling without pre stretching. AS refers to air cooling with pre stretching. W refers to water cooling without pre stretching. WS refers to water cooling with pre stretching and the number at the end refers to the parallel.

5.3 Fracture surfaces

Figure 5.3 and 5.4 show SEM images of the fracture surface of the water cooled tensile tests from the author's project work. Only the water cooled tensile tests are presented in this section. The complete selection of fracture surfaces including the air cooled tests can be found in appendix C. The air cooled tests are included in the appendix because of large similarities to the water cooled samples. Figure 5.3 show the tensile tests stored for 24 hours. Both the not-stretched fracture surface and the pre stretched fracture surfaces show dimples, indicating a ductile fracture. All of the tensile specimens, both water cooled and air cooled, contain a mixture of dimples and flat areas. The pre stretched water cooled tensile specimen (Figure 5.3c and 5.3d) show more dimples than the not-stretched water cooled tensile specimen (Figure 5.3a and 5.3b). This is only observed in the water cooled tensile specimens stored at room temperature for 24 hours (Figure 5.3).

Particles are observed at the bottom of some of the dimples in all of the water cooled and air cooled fracture surfaces. The particles can also be in the opposite dimple at the matching fracture surface and therefore not observed in all dimples. These particles can come from the casting process or they can be pollution elements. This can be determine by an EDS analysis, and this is done in Section 5.4. Some cracked particles are also observed in the dimples of all the water cooled and air cooled fracture surfaces.

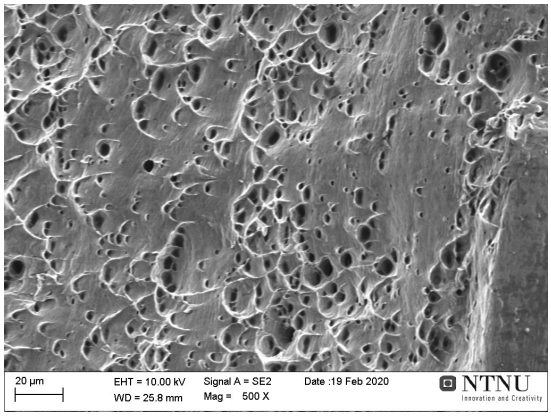

(a) 500x magnification, not-stretched.

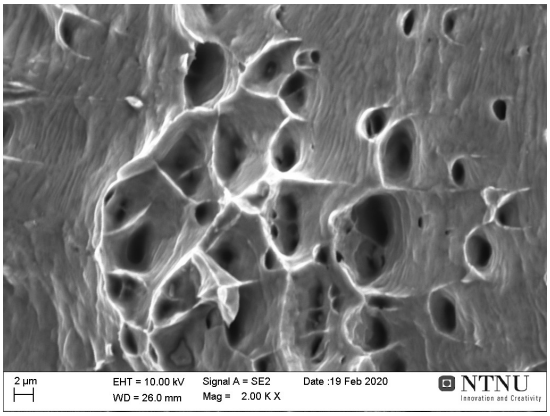

(b) 2000x magnification, not-stretched.

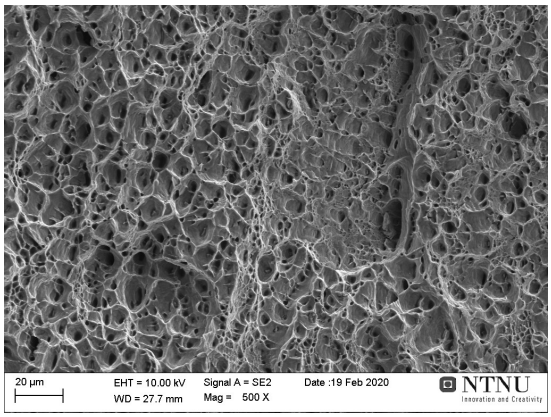

(c) 500x magnification, pre stretched 0.5%.

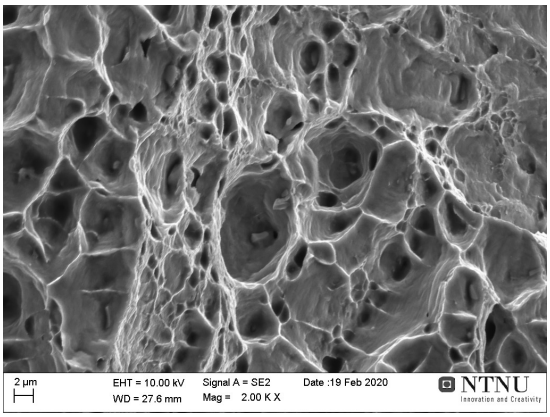

(d) 2000x magnification, pre stretched 0.5%.

Figure 5.3: Fracture surface of water cooled tensile specimens stored for 24 hour at room temperature before testing. Figure 5.3a and 5.3b are not-stretched and Figure 5.3c and 5.3d are pre stretched 0.5% after water cooling.

In Figure 5.4 the water cooled tensile tests are stored for 7 days. Like the water cooled tensile

specimens stored for 24 hours, dimples are observed in all the water cooled tensile specimens stored for 7 days (Figure 5.4). Unlike the specimens stored for 24 hours, there is not a large difference in the magnitude of dimples in the not-stretched sample(figure 5.4a) and the pre stretched sample(Figure 5.4c). In the SEM images with 2000x magnitude (Figure 5.4b and 5.4d) there are observed both cracked and uncracked particles in the dimples. This is similar to the particles found in the water cooled specimens stored for 24 hours.

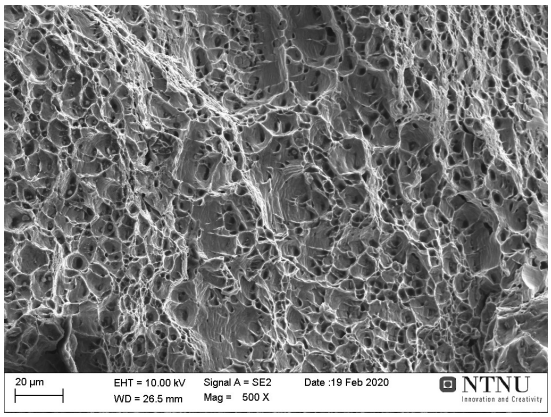

(a) 500x magnification, not-stretched.

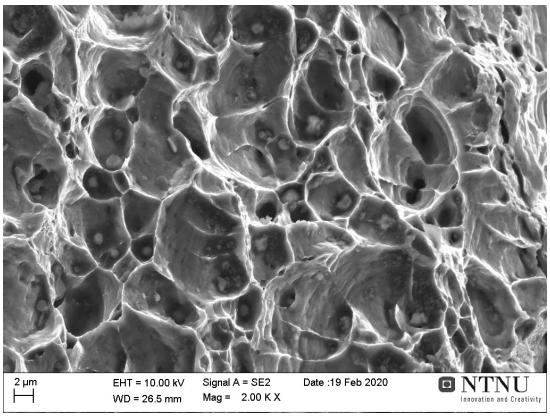

(b) 2000x magnification, not-stretched.

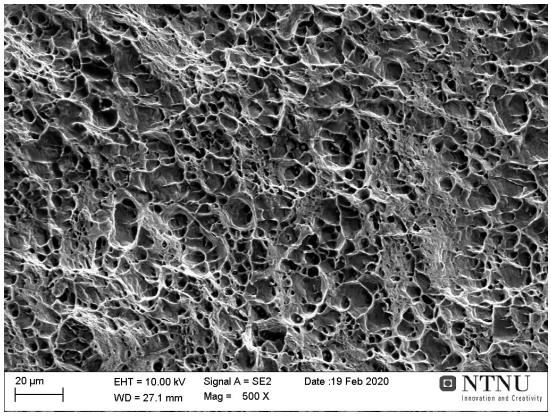

(c) 500x magnification, pre stretched 0.5%.

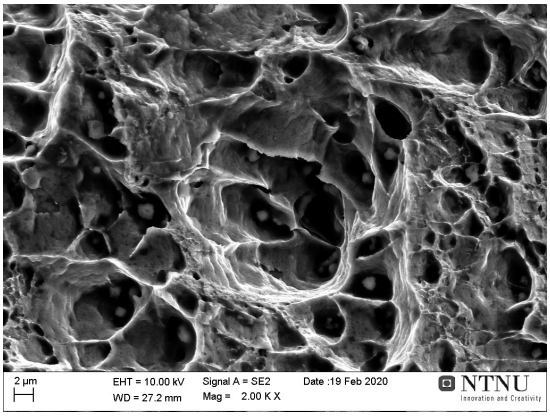

(d) 2000x magnification, pre stretched 0.5%.

Figure 5.4: Fracture surface of water cooled tensile specimens stored for 7 days at room temperature before testing. Figure 5.4a and 5.4b are not-stretched and Figure 5.4c and 5.4d are pre stretched 0.5% after water cooling.

5.4 EDS of fracture surface of tensile tests

Figure 5.5-5.11 show SEM images of fracture surfaces and the associated chemical composition to points in the SEM images. The chemical composition is obtained by EDS. The fracture surfaces are the same broken tensile tests as investigated in Section 5.2 and 5.3. A selection of the EDS results are presented in this section, the complete results are given in appendix D. All the associated intensity spectra are also given in appendix D.

5.4.1 Air cooled tensile tests

Figure 5.5 and 5.6 show the fracture surface of air cooled tensile tests stored for 24 hours. Figure 5.5 is not-stretched and Figure 5.6 is pre stretched 0.5% after cooling. The EDS result from all the air cooled tensile test were quite similar. Therefore only a selection of tensile specimens stored for 24 hours at room temperature are shown in this section. The complete collection of

the air cooled tensile tests are found in appendix D.

The EDS analyzes of the particles labelled 49, 50 and 51 in Figure 5.5a show that the particles have similar chemical composition, and they consist mainly of aluminium and smaller parts of iron, manganese and potassium. The morphology and chemical composition indicate that these particles are constituent particles. Point 52 is a reference point of the matrix.

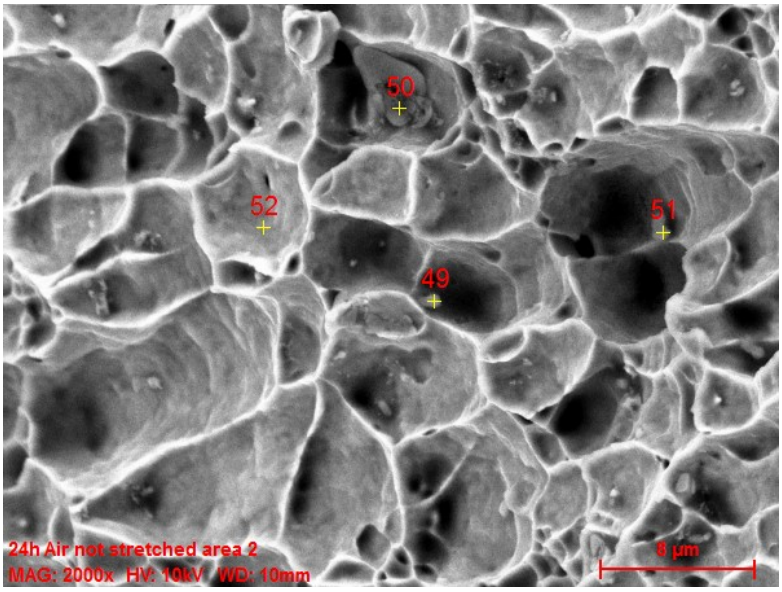

(a) SEM image of fracture area 2 in a not-stretched air cooled tensile specimen stored for 24 hours at room temperature.

Element given in $[wt\%]$	Al	O	Mg	Ti	Fe	Mn	Si	K	S	Ca	Na	C	Cl
49	77.47	0	1.62	2.40	6.04	4.31	0	4.33	0.27	2.74	0.80	0.01	0
50	75.99	0	1.35	1.76	4.86	3.22	0	7.64	0.08	1.40	0.67	0.14	2.88
51	71.66	0	1.20	0.02	11.94	9.14	0	2.32	0.04	3.44	0.24	0	0
52	95.37	1.52	1.43	0.02	0.03	0	0.68	0.08	0.05	0.12	0.38	0.33	0

Figure 5.5: SEM image of fracture area 2 in a not-stretched air cooled specimen stored for 24 hours. Chemical analysis as nominative chemical composition of points in the SEM image is given in the table below, obtained by EDS.

The particles labelled 60 and 61 in Figure 5.6a are probably constituent particles, based on chemical composition and morphology. Particle 60 is a constituent particle containing aluminium, iron and manganese, and particle 61 contain silicon in addition to the mentioned elements. Point 62 is a reference point.

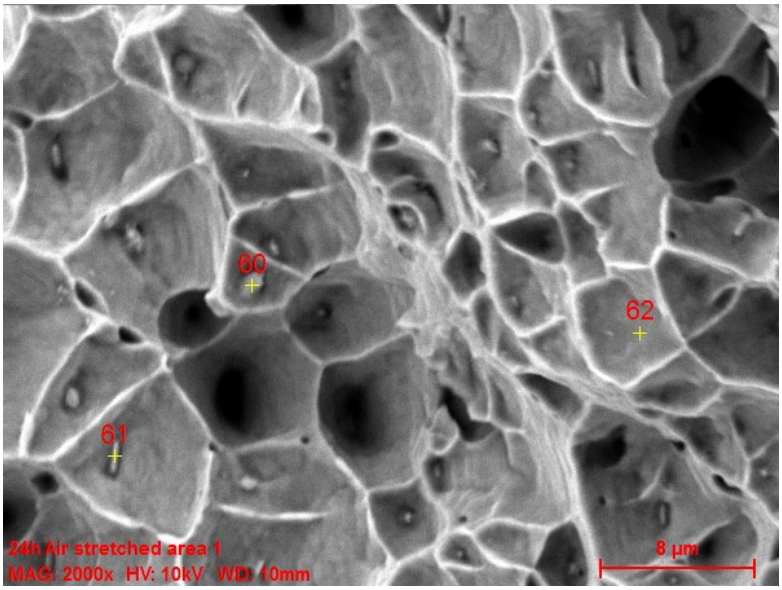

(a) SEM image of fracture area 1 in a pre-stretched air cooled tensile specimen stored for 24 hours at room temperature.

Element given in $[wt\%]$	Al	O	Mg	Ti	Fe	Mn	Si	K	S	Ca	Na	C	Cl
60	65.92	0	1.01	0.82	26.01	4.85	0.53	0.14	0	0.41	0.32	0	0
61	75.16	0.40	1.10	0.23	16.84	2.89	3.08	0.04	0	0	0.25	0	0
62	96.96	0.49	1.38	0.03	0.40	0	0.46	0	0	0	0.28	0	0

Figure 5.6: SEM image of fracture area 1 in a pre stretched air cooled specimen stored for 24 hours. Chemical analysis as nominative chemical composition of points in the SEM image is given in the table below, obtained by EDS.

5.4.2 Water cooled tensile tests

Figure 5.7-5.9 show SEM images of fracture surfaces of tensile specimens cooled in water. Figure 5.7 and Figure 5.8 are stored for 24 hours at room temperature, and respectively not-stretched and pre stretched 0.5%. Figure 5.9 is stored for 7 days at room temperature and not-stretched. Like the air cooled specimens, all of the water cooled specimens are quite similar, and the complete selection can be found in appendix D.

The EDS result of particle labelled 53 in Figure 5.7a indicate that the particle can be a constituent particle containing small parts of iron and manganese in addition to aluminium. Particle 54 contain smaller parts of carbon, chloride and oxygen in addition to aluminium. These elements are not expected based on the AA6063 composition, and it is suspected that this particle is a pollution particle. Particle 55 is high in potassium and this is also a suspected pollution particle.

The fracture surface in Figure 5.7a, an area of smaller and shallower dimples are also seen. These dimples do not contain particles.

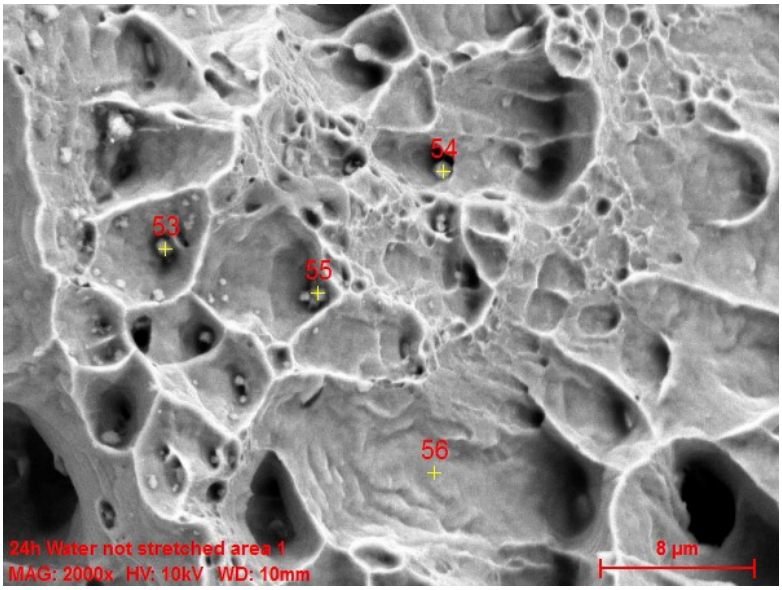

(a) SEM image of fracture area 1 in a not-stretched water cooled tensile specimen stored for 24 hours at room temperature.

Element given in $[wt\%]$	Al	O	Mg	Ti	Fe	Mn	Si	K	S	Ca	Na	C	Cl
53	86.31	0.09	1.43	1.35	3.21	3.07	0	1.81	0.08	1.08	0.46	0	1.12
54	75.93	5.10	1.36	0.01	0	0	0.92	1.91	0.22	0.97	1.07	9.07	3.46
55	71.59	0.10	1.46	1.25	3.15	2.69	0	11.66	0.03	1.57	0.61	0.11	5.77
56	96.79	0.79	1.37	0	0.03	0.15	0.56	0.01	0.05	0	0.25	0	0.01

Figure 5.7: SEM image of fracture area 1 in a not-stretched water cooled tensile specimen stored for 24 hours at room temperature. Chemical analysis as as nominative chemical composition of points in the SEM image is given in the table below, obtained by EDS.

In Figure 5.8a the particles labelled 71, 72 and 74 are clearly constituent particles. This is seen from the chemical composition and the morphology of the particle. Particle 71 and 72 are AlFeSi constituent particles, meanwhile particle 74 is a AlFeMn constituent particle.

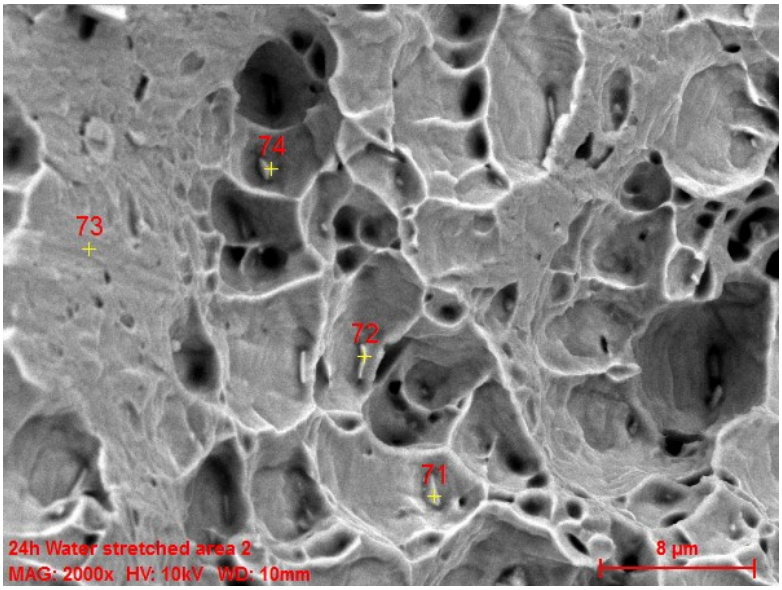

(a) SEM image of fracture area 2 in a pre stretched water cooled tensile specimen sample stored for 24 hours at room temperature.

Element given in $[wt\%]$	Al	O	Mg	Ti	Fe	Mn	Si	K	S	Ca	Na	C	Cl
71	65.96	0.93	0.98	0	22.40	3.02	6.23	0	0	0.07	0.41	0	0
72	83.78	0.47	1.30	0.05	9.36	1.88	2.84	0.03	0	0	0.23	0	0.05
73	95.93	1.23	1.62	0.05	0.27	0	0.52	0.04	0.03	0.02	0.28	0	0
74	61.16	0	0.40	0	27.89	10.29	0	0.04	0	0.18	0	0	0.04

Figure 5.8: SEM image of fracture area 2 in a pre stretched water cooled tensile specimen stored for 24 hours at room temperature. Chemical analysis as nominative chemical composition of points in the SEM image is given in the table below, obtained by EDS.

The labelled particle 39 and 41 in Figure 5.6 were expected to be constituent particles by the morphology of the particles, but the particles are very similar in chemical composition to the reference point 40. This can indicate that there are large level differences in the specimen, and the x-ray went through some of the matrix material in order to get to the particles. The x-ray will give the chemical composition of the first material it encounters. In this case the x-ray might give the chemical composition of the matrix material, instead of the particle.

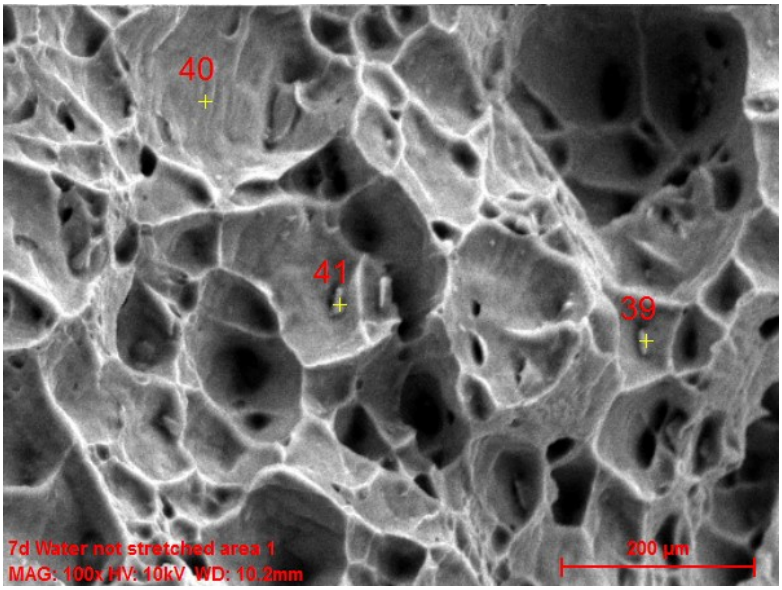

(a) SEM image of fracture area 1 in a not-stretched water cooled tensile specimens stored for 7 days at room temperature.

Element given in $[wt\%]$	Al	O	Mg	Ti	Fe	Mn	Si	K	S	Ca	Na	C	Cl
39	95.46	0.64	1.31	0	0.37	0.01	1.91	0	0	0.03	0.28	0	0
40	97.30	0.65	1.30	0.03	0	0	0.41	0.02	0.01	0.06	0.20	0	0.02
41	96.43	1.05	1.28	0.13	0	0	0.63	0	0	0.24	0.23	0	0

Figure 5.9: SEM image of fracture area in a not-stretched water cooled tensile specimen stored for 7 days at room temperature. Chemical analysis as nominative chemical composition of points in the SEM image is given in the table below, obtained by EDS.

5.4.3 Pollution particles

In some cases, the EDS revealed high values of potassium, sulfur, calcium, sodium and chloride. This indicates that the specimens have been exposed to some pollution. Figure 5.10 and 5.11 show both fracture surfaces containing pollution elements. The morphology of the pollution particles is differ more from the constituent particles. The pollution particles are more circular and not that "baked into" the matrix as the casting particles. The source of the pollution can be the production or casting process, but also the sample preparation can be a source of pollution.

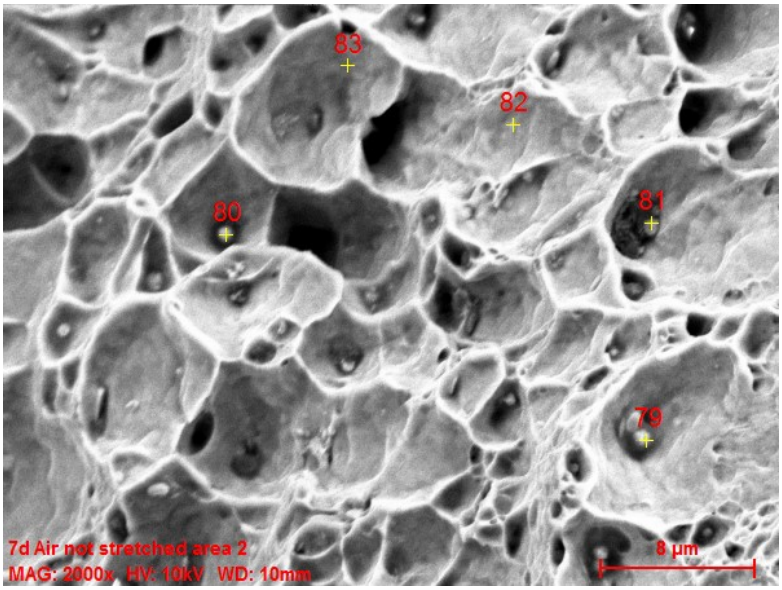

(a) SEM image of fracture area 2 in a not-stretched air cooled tensile specimens stored for 7days at room temperature.

Element given in $[wt\%]$	Al	O	Mg	Ti	Fe	Mn	Si	K	S	Ca	Na	C	Cl
79	38.50	12.45	1.01	0	0.01	0.11	0.62	20.37	0.51	0.84	2.95	6.53	16.10
80	61.38	6.94	1.32	0	0.02	0.41	0	11.17	0.83	3.08	2.16	3.85	8.83
81	62.67	11.68	1.23	0	0.62	0.22	0.57	1.22	0.15	16.34	0.66	3.89	0.74
82	97.64	0.40	1.37	0	0	0	0.30	0	0.01	0.03	0.22	0	0.02
83	94.09	0.06	1.40	0.65	1.56	1.33	0	0.23	0.01	0.31	0.29	0	0.08

Figure 5.10: SEM image of fracture area 2 in a not-stretched air cooled tensile specimens stored for 7 days at room temperature. Chemical analysis as nominative chemical composition of points in the SEM image is given in the table below, obtained by EDS.

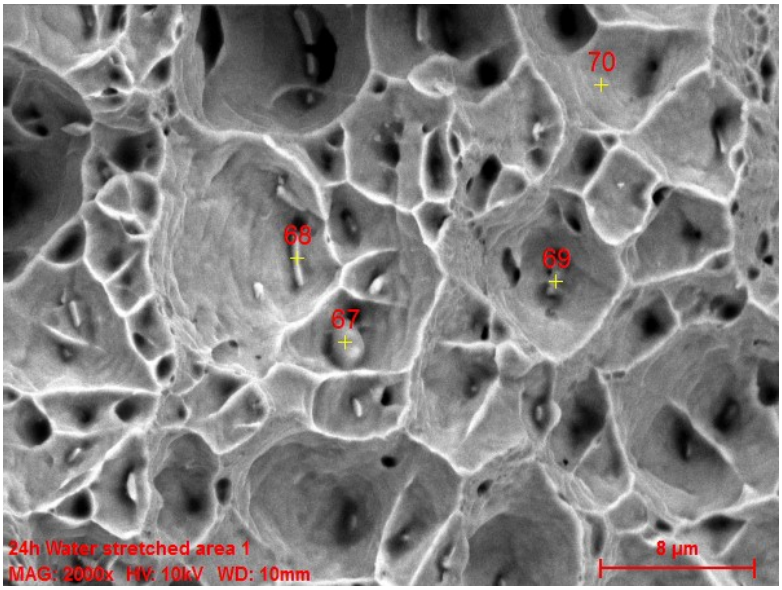

(a) SEM image of fracture area 1 in a pre stretched water cooled tensile specimens stored for 24 hours at room temperature.

Element given in $[wt\%]$	Al	O	Mg	Ti	Fe	Mn	Si	K	S	Ca	Na	C	Cl
67	45.00	17.45	1.02	0	0.50	0	1.16	2.55	0.55	0.23	1.42	26.27	3.86
68	97.24	0.24	1.31	0.01	0.42	0	0.50	0	0.04	0	0.23	0	0
69	95.40	1.86	1.50	0.05	0.01	0	0.28	0.13	0.12	0.23	0.31	0	0.10
70	96.69	0.64	1.43	0.01	0.07	0.11	0.65	0	0.07	0	0.31	0	0.02

Figure 5.11: SEM image of fracture area 1 in a pre stretched water cooled tensile specimens stored for 24 hours at room temperature. Chemical analysis as nominative chemical composition of points in the SEM image is given in the table below, obtained by EDS.

5.5 Material characterization with EBSD

EBSD scans are performed as explained in Section 4.3.2. The preparation method used was the same used in the project thesis, but the quality of the EBSD scans were very poor. Initially two areas in the profile were scanned (more details of areas in Section 4.3.2), both scans experienced poor image quality. The poor quality made it hard to index the images, and fault in the indexing called "snow in the image" is seen in Figure 5.12b. The quality of one of the scanned areas was so bad that it was not possible to get a reasonably indexing. For this reason, only one IPF map is presented.

The vibration polishing step in the preparation was suspected to be the cause of the poor image quality. A re-preparation of the samples was planned, but was never finished due to the coronavirus outbreak and closing of NTNU.

The EBSD scan in Figure 5.12 show a similar grain structure to the EBSD scan performed in the project thesis (can be seen in the next chapter). The texture seen in Figure 5.12 is uncertain because of the poor image quality and indexing (CI below 0.3 in the indexing). The IPF map probably contain multiple wrong indexing. Based on this the EBSD scans are not used in further discussion.

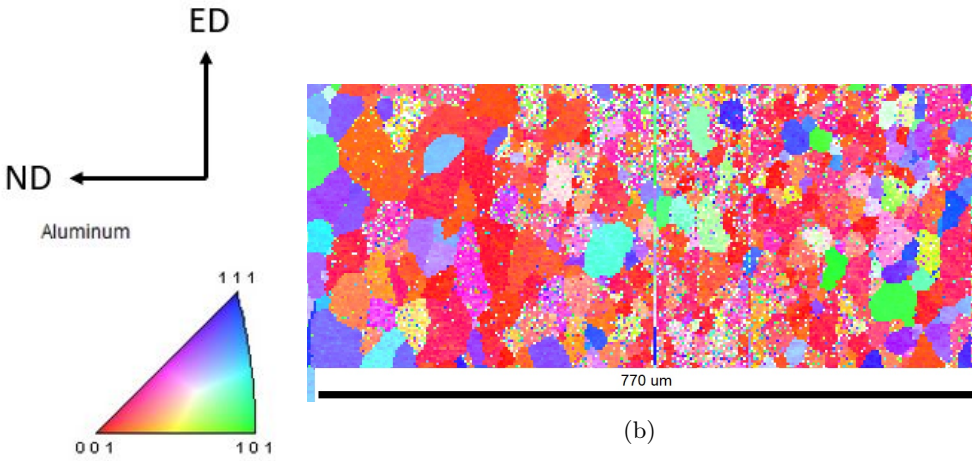

(a) (b)

Figure 5.12: IPF map through thickness in approximately the p=0.5 position in the profile (Figure 4.1b). a) is the associated stereographic triangle, and b) is the IPF map. TD is the IPF axis

5.6 Natural aging

The work of making NA curves were aborted, and for that reason the curves in Figure 5.13 are not finished. The water cooling in Figure 5.13 is higher in hardness than the other two coolants in the starting phase. Air and oil cooling are very similar in hardness, and they are both within each other's uncertainty bars during the staring phase. Since the experiment never was finish, there is not possible to predict if air and oil cooling would approach water. Since the curve is unfinished this NA curve will not be a part in the discussion chapter. However a brief discussion and commenting will follow in this section.

The water cooling is much faster than the other two coolants and therefore higher in hardness. This is caused by the fast cooling, which give a higher level of supersaturation of vacancies and solute atoms. This will result in larger strength during aging at room temperature, and give a higher hardness for water. Some of the largest weakness in using hardness is that the method uses a small part of the surface of the material. This is a disadvantage if the material is very heterogeneous. Earlier investigations in the project thesis indicate that the NA specimens used are heterogeneous, where the centre of the sample differ much from surface. The investigations also indicated that the surface itself can be very different from area to area. This will give large uncertainties in the hardness test results.

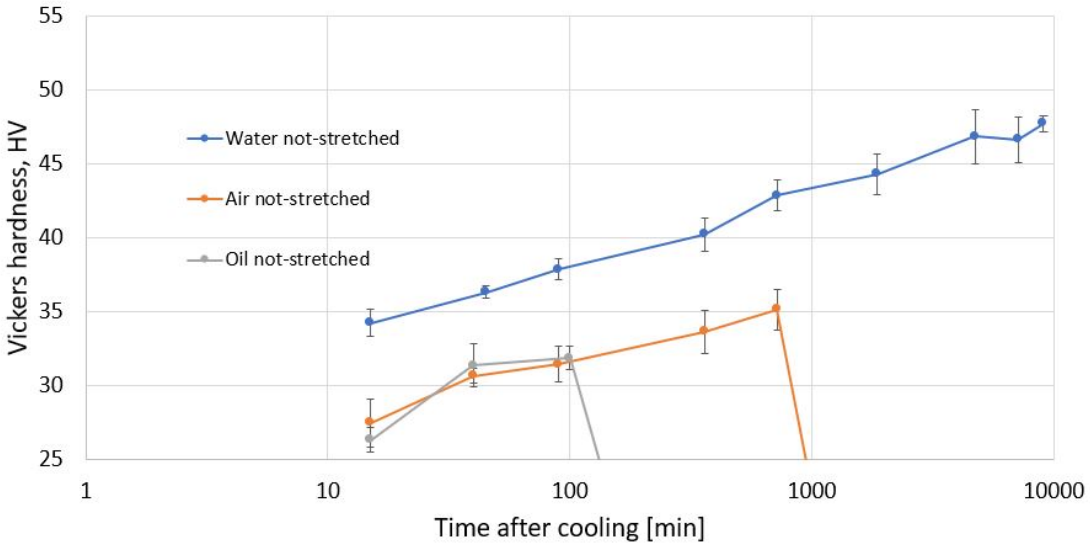

Figure 5.13: Hardness curves of water-, oil- and air cooled specimens. All specimens are not-stretched and solution heat treated at 550°C for 20 minutes in a salt bath.

6. Recap of experimental results from project thesis

6.1 Texture

The IPF map of the as-received material is shown in Figure 6.1. The scan is taken approximately in the p=0.5 position of the profile (Figure 4.1b). Figure 6.1 show a typical recrystallized extrusion texture. A random oriented layer is observed in the surface, followed by a Goss layer and a cube oriented layer in the middle. In this case the cube layer seems shifted to the negative ND.

Figure 6.1: IPF map through the thickness from the author's project thesis. Scan is parallel to the TD axis.

6.2 Natural aging

Natural aging in the project thesis is performed at room temperature after a 20 minutes solution heat treatment (SHT) in salt bath at 550°. After the SHT the samples are quenched in water, oil and air. One parallel is pre stretched 0.5% plastic strain just after quenching, and the other parallel is not-stretched. The natural aging performed in the project thesis is given in Figure 6.2. The natural ageing in Figure 6.2 indicate very heterogeneous surface and large error bars. In the dashed water NA curve in Figure 6.2, the hardness indenter broke during the measurements. The water results are therefore unreliable. Water 2 in Figure 6.2a is a reproduced water NA curve with a fixed hardness indenter, and a representative NA curve. Due to limited time this was only performed for the not-stretched specimens. An aging effect in room temperature is observed in both the not-stretched (Figure 6.2a) and pre stretched specimens (Figure 6.2b).

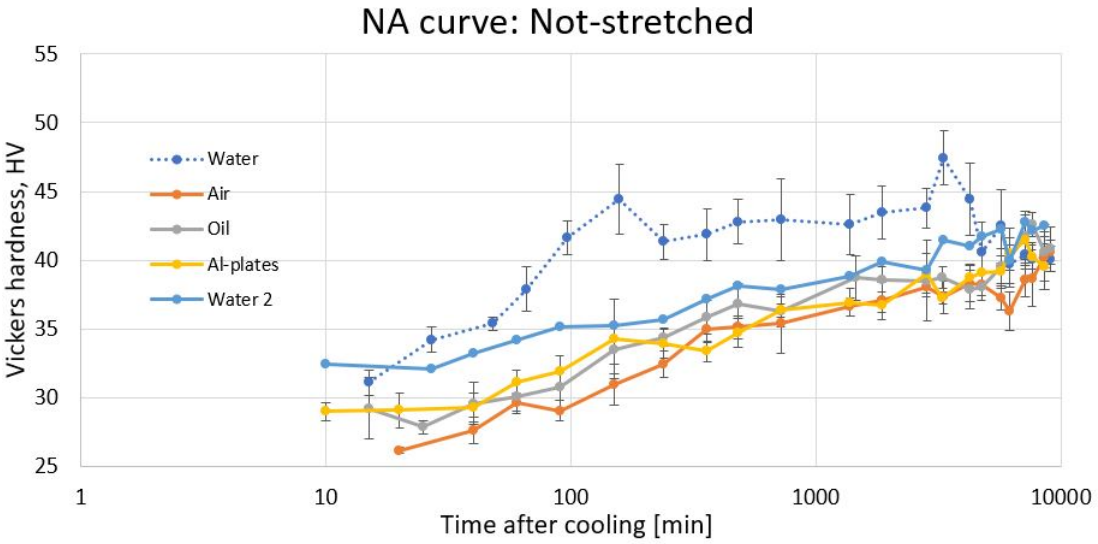

(a)

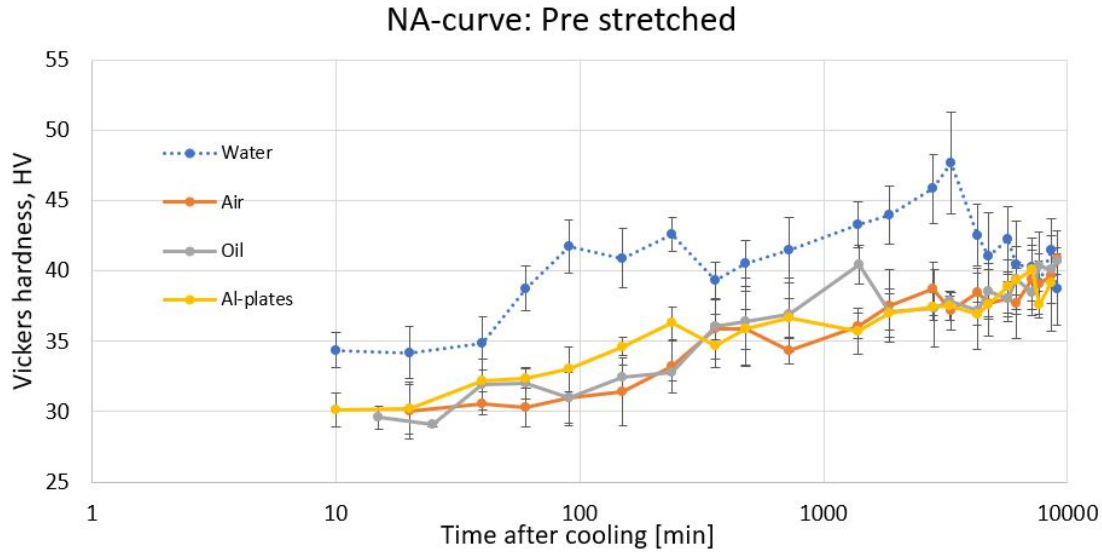

(b)

Figure 6.2: Recap of NA curves from the author's project thesis, a) is not-stretched after quenching from SHT. b) is pre stretched 0.5% just after quenching from SHT.

6.3 Tensile testing

The tensile testing is performed after the same SHT as in the previous section, and the stress-strain curves are given in Figure 6.3. The tensile specimens are stored at room temperature between the SHT and testing, and the specimens are stored for 24 hours or 7 days.

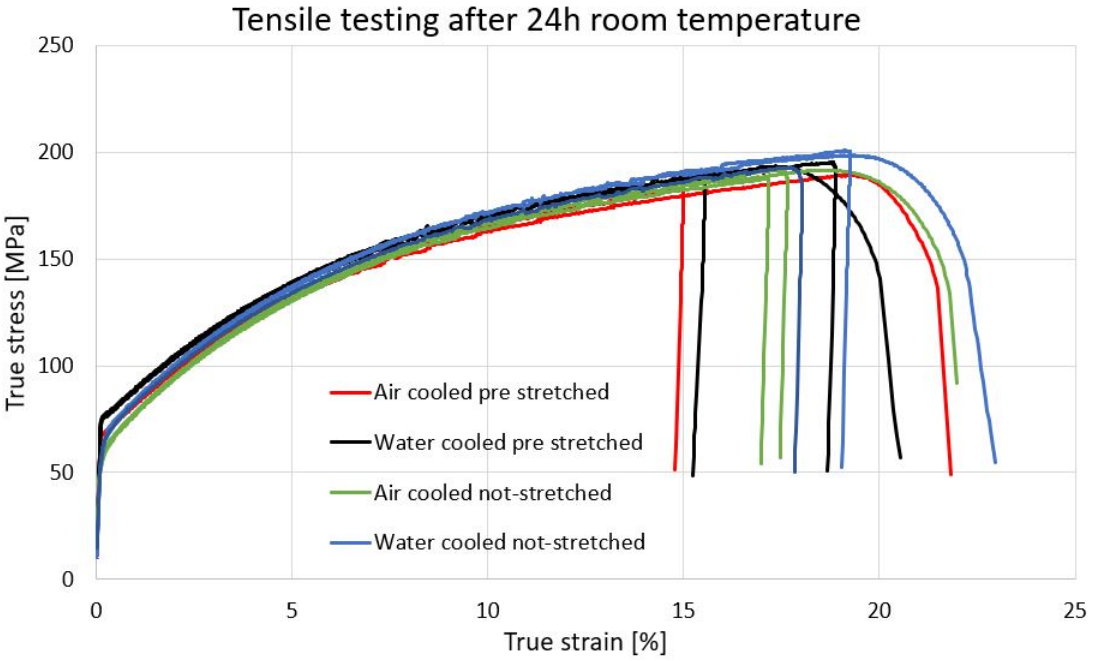

(a)

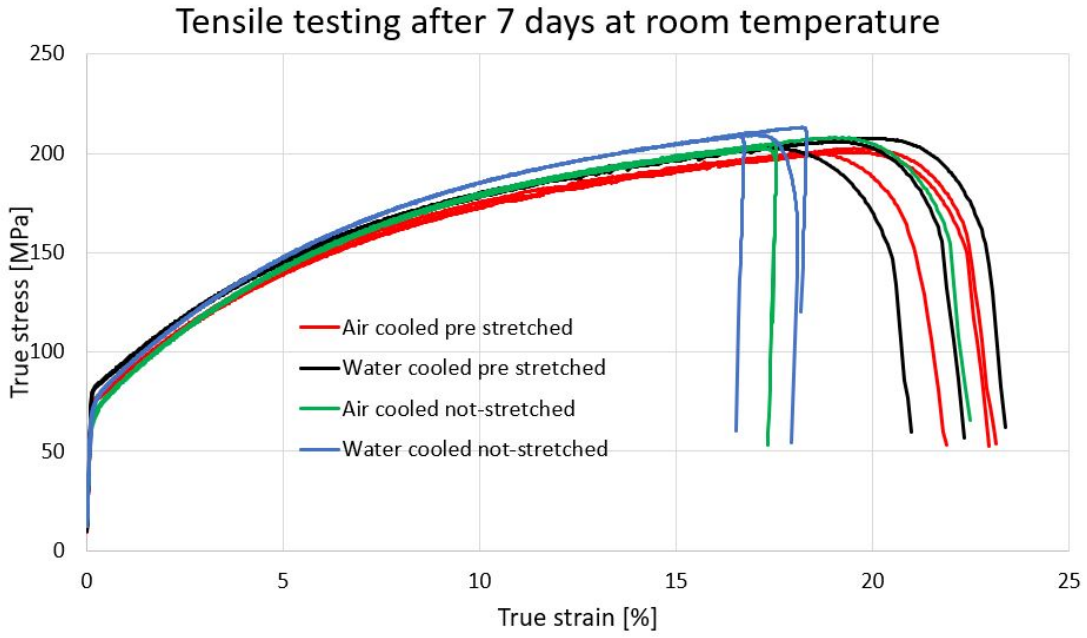

(b)

Figure 6.3: Tensile testing results from the author's project thesis. The tensile specimens are stored for (a) 24 hours and (b) 7 days after SHT. Pre stretched samples are stretched 0.5% plastic strain just after SHT. Testing is performed in T4 condition.

7. Discussion

7.1 Method and source of error

This section includes a discussion of the measuring method of the cooling rates and the measuring of area fraction based fracture strain. Both of these measurement methods are specially developed for this project. For this reason some comments are included regarding the source of error.

7.1.1 Cooling rate measurements

The temperature measurement setup is a possible source of error. The thermocouple measures the temperature at the first material it gets in contact with. In the setup there is a possibility that the thermocouple can move, and if it moves the thermocouple can lose the contact with the material. In the periods of lost contact, the dataTaker will not register any temperature and lead to a discontinuous temperature curve. This is clearly observed in the air temperature curve in Figure 5.1. To minimize the loss of temperature information during the periods without material contact, the logging range is set to 0.2 second. This produce a large quantity of measuring points, and a better base for estimating the temperature curves in periods of lost contact, as shown in the estimated curves in Figure 5.1. The possibility of the thermocouple measuring the coolant is removed by a setup where the thermocouple never got in touch with the coolant, and the thermocouple does not measure air temperature.

7.1.2 Calculation of area fraction based fracture strain after tensile testing

Calculation of fracture strain based on area fraction is acceptable on an average base for cylindrical specimens, but planar specimens are dependent on a well-defined fracture surface. In this work the fracture surface had a rectangular shape, and accurate measurements were possible with the right light setting in the macro scope. In the matlab script used in the image measuring, the fracture surface area is drawn up manually. Therefore it will always be a small uncertainty connected to this. Meanwhile an average basis this method is expected to give reasonably accurate results.

7.2 Cooling rate effect on the stress-strain behaviour

Stress-strain curves from the author's project thesis have been replotted in Figure 6.3. From this figure it is clearly seen that the cooling rate has affected the ultimate stress, σ_{UTS}. Regarding cooling rates (Figure 5.1), approximately 250°C is the critical temperature to reach. In the approximately temperature range 250°-400°, β-particles or Mg_2Si can precipitate. These brittle particles are disadvantageous for the aging potential. It is important to have a fast cooling rate in this interval to avoid precipitation of β-particles. Below 250°C favourable precipitation particles are precipitated, and the cooling rate is not of critical importance. According to Figure 5.1 water quenched the metal to a temperature below 250°C in approximately 1 second, and air quenched below 250°C in 1 minute and 38 seconds. The faster water quenching results in a higher level of supersaturated vacancies and solute atoms, than air quenching does. This gives a strength contribution through natural ageing, which is confirmed in hardness curves (Figure 6.2) from earlier investigations. The strength will increase with time during natural ageing, and this correspond with the observed ultimate stress behaviour in Figure 6.3b. A more detailed investigation of the natural ageing behaviour was in progress, but aborted due to the coronavirus outbreak and closing of NTNU.

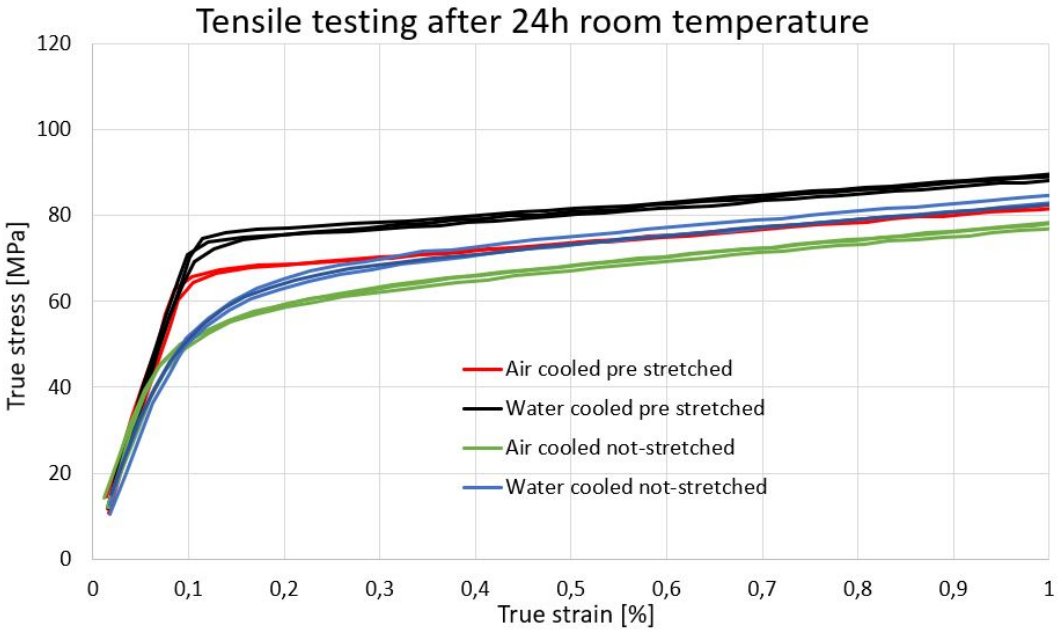

(a)

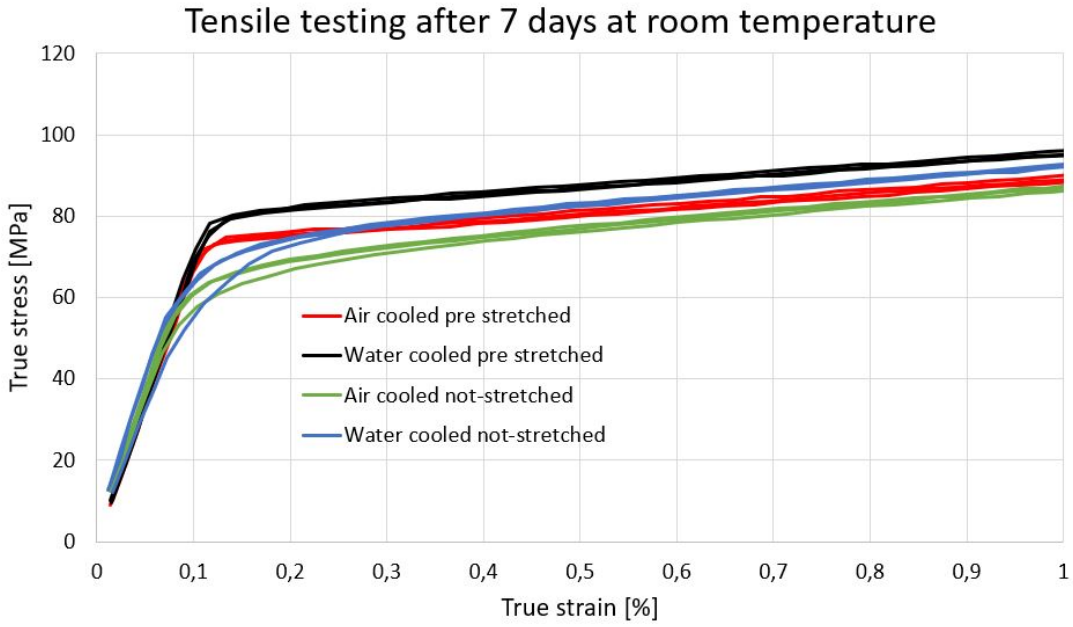

(b)

Figure 7.1: A close-up of the tensile testing curve from 0-1% true strain, (a) is stored for 24 hours and (b) is stored for 7 days, and tested in T4 condition. The pre stretched specimens are pre stretched 0.5% plastic strain after quenching to room temperature

In the tensile specimens in Figure 6.3 the pre stretching seemed to affect the strength of the tensile specimens in T4 condition. A general trend observed in the true stress-strain curves (Figure 6.3), is lower strength in the pre stretched curve than in the corresponding not-stretched curve. The strength difference between pre stretched and not-stretched tensile specimens increase with storage time. The shape at the beginning of the stress-strain curve is also distinct for the pre stretched parallel, as observed in the close-ups in Figure 7.1. During the pre stretching some grains in the polycrystal starts deforming plastic, while other grains are deformed elastic.

This can physically be described as a composite effect, where gradually more grains become plastic during the elastic-plastic transition and this result in a rounded transition. When the pre stretched specimens are tested after 24 hours or 7 days, most of the grains switch from elastic to plastic at the same stress. By analysing both the pre stretched and the not-stretched specimens, all the grains in the polycrystal are deforming plasticly at approximately 0.3% true strain. Due to less composite effect in the pre stretched specimens, these specimens will deform plastic earlier after approximately 0.12% true strain and give the distinct shape of the curve. It should be emphasized that in this context the pre stretching is performed in the same direction as the tensile testing. If the composite effect is the reason to the distinct shape, it can be confirmed if the pre stretching is performed in another direction. This will result in the same amount of composite effect in the tensile direction of both pre stretched and not-stretched tensile specimen, and the stress-strain curve will not get the distinct shape.

After 7 days it is a marked difference in the elastic-plastic transition of the stress-strain curves from the 24 hours curves (Figure 7.1). The difference between the pre stretched and not-stretched curves is smaller after 7 days than 24 hours. The pre stretched curves in Figure 7.1b show a slight more experimental spread than the stretched curves in Figure 7.1a. At approximately 0.2% true strain in Figure 7.1b one of the three specimens in both the water- and air pre stretched curves drops down sooner than the other two. Such irregularities can be caused by a skew mounted specimen in the tensile machine or if the specimen gets a slight bend during the SHT or handling. The smaller difference between the pre stretched and the not-stretched curves after 7 days, is an effect not observed in any read publications. Also limited research is performed on the area of pre stretched tensile specimens. For this reasons it is difficult to predict the reason why the difference between pre stretched and not-stretched specimens is less after 7 days. One possible explanation can be relaxation of stress during time. Solidification shrinkage of aluminium can be up to 6-8%[11], and during the quenching the aluminium will contract. Based on previous discussions in the literature study, AA6063 seems quite isotropic, this means that the grains contract approximately equally everywhere. The alteration in the shape of the grains during the contracting cause internal stress evenly distributed throughout the alloy. These stresses can be relaxed differently in the pre stretched and not-stretched specimens with time and cause the less difference between pre stretched and not-stretched specimens after 7 days. This is only a possible hypothesis and more research is needed in this area to be able to draw any conclusions.

7.2.1 Strain

Two measurements are used for ductility in the context of tensile testing and necking. They are the fracture strain measured from the extensometer (called elongation fracture strain), and fracture strain calculated from the fracture surface area on the fractured specimens after tensile testing (called area fraction fracture strain). Further in this discussion these measurements will be referred to as elongation fracture strain and area fraction fracture strain. Elongation fracture strain is a measurement of elongation through the extensometer. This measurement will be affected by the length of the extensometer, a longer extensometer gives a shorter elongation fraction strain, as discussed in the author's project thesis (excerpt given in appendix A). In tensile testing of thin flat specimens, flow instability including local necking happens before damage and fracture. The elongation based fracture strain measured through the extensometer correlates strongly with the onset of necking, e.g. with the uniform strain. The elongation fracture strain is therefore strongly affected by the specimen geometry and extensometer, where as area fraction fracture strain is closer to a material property. The area fraction fracture strain gives reasonably accurate average results. Unlike elongation fracture strain, the area fraction fracture strain is not dependent on the length of the extensometer. Since the area fraction fracture strain is based on a ratio between original area and fracture surface, it is a more universal measurement and can be compared to other published results with other sample geometries and extensometer lengths.

The main challenge during tensile testing is that the fractures developed outside the extensometer, as seen in Figure 6.3. When only a few tests breaking within the extensometer, this lead to a small statistical basis and made it challenging to observe any trends in elongation

fracture strain. When the tensile specimens fracture outside the extensometer, the stress will stop at the uniform stress, ϵ_u, and the stress-strain curve will be incomplete. In cooling parallels with more than one correctly measured test, a spread in elongation fracture strain can often be observed e.g. the water cooled pre stretched tests in Figure 6.3b. Meanwhile smaller spread is observed in air cooled pre stretched tests in Figure 6.3b. None of the cooling rates stand out regarding elongation fracture strain, as seen for strength. Based on a possibility of large experimental spread in elongation fracture strain, it can't be concluded whether cooling rate affects the elongation fracture strain or not.

The area fraction fracture strain listed in Table 5.1 is in agreement with the elongation fracture strain from the stress-strain curves, and don't show a relation between cooling rate and area fraction fracture strain. There neither seems to be a relation between the area fraction fracture strain and pre stretching or not-stretching, nor time of storage between SHT and testing. On the other hand, storage time and stretching seems to affect the stress level, as discussed earlier in this section. Khadyko et al.[31] observed a strong linear trend that relates the true stress onset of necking level and the area fraction fracture strain. This linear trend is not seen in the results in this work. A reasonably explanation can be the difference in testing strength range in the results obtained in this report compared to Khadyko et al.[31]. In this report the tensile specimens are only tested in T4 condition, but Khadyko et al.[31] tested in T1, T6, T7 and O condition. In a larger stress onset of necking range a linear relation will be more clear, than in a narrow range.

7.3 Relations between fracture surface and fracture strain

Both cooling rates showed similar fracture surface with a mix of dimples and flat areas, but with a large overweight of dimples in most cases. The observed dimples are a strong indication of ductile fracture. This is also is confirmed by the large elongation fracture strains observed in the true stress-strain curves and in the area fraction fracture strains. A different fracture mechanism is working in the flat areas than the fracture mechanism in dimples. In Figure 5.3a and 5.3b water cooled not-stretched tensile specimens are shown. The tensile specimens are stored for 24 hours at room temperature before testing and referred to as W24h.

The fracture surface of W24h stands out compared to the investigated fracture surfaces of the other tensile specimens. The proportion of flat areas is larger in the W24h compared to the other investigated fracture surfaces. The fracture mechanism operating in the flat areas can be similar to the fracture mechanism in the dimples, because the fracture strain of W24h is equal to the other specimens with more dimples. The large work hardening and fracture strain observed in the tensile curves of W24h (Figure 6.3a) clearly indicate ductile fracture, even though noticeable less dimples are observed. The stress-strain curve of W24h is similar to the stress-strain curves of the other investigated tensile specimens stored for 24 hours at room temperature (Figure 6.3a). Because of this, energy required to failure in the tensile specimens stored for 24 hours are very similar. The ratio of the flat areas are larger in W24h, but the energy to failure is similar to the other fracture surfaces with a larger ratio of dimples. For this reason the fracture mechanism operation in the flat areas, possibly requires similar energy as the mechanism in the dimples.

Dimples of different sizes are observed in all the fracture surfaces, but they are all evenly distributed. There is not found an area with high density of fine dimples without particles. The fine dimples can be caused by several mechanisms e.g. voids can be created in the junction points of interacting slip planes[40]. Areas of intercrystalline fracture connected to small dimples are not seen, and this is probably due to the T4 condition of the material and thereby not containing PFZ. Because of the possibility that the small dimples are nucleated at grain boundary precipitates and grow by void growth within the PEZ[13].

7.3.1 Casting particles in the fracture surface

In the fracture surfaces particles are observed at the bottom of many of the dimples. Some dimples do not contain any particles, but the particles can have fallen out during preparation or can be present on the opposite fracture surface. Through EDS, both intermetallic constituent particles and pollution particles were found in all investigated fracture surfaces. The observation of constituent particles and the observed dimpled surface supports the assumption that the working fracture mechanism in the tensile specimens is nucleation, growth and coalescence of voids.

Similar observations of constituent particles in the dimples are reported by Chen et al.[6] and Frodal et al.[13]. Cracked particles and partly cracked particles are also observed in a few of the dimples, and these particles probably cracked during the extrusion process. The volume fraction and size distribution of intermetallic constituent particles significantly influence the tensile strain to failure[41, 48]. Thomesen et al.[48] believed the main reason for differences in failure strain of extruded AA6061-T6, AA6063-T6 and AA6110-T6 were caused by differences in the volume fraction and size distribution of the constituent particles. The heat treatment to achieve T6, do not alter the volume fraction or size distribution of the constituent particles. It is therefore reasonable to believe this also holds for AA6063-T4. The different parallels in the tensile testing (water cooled, air cooled, pre stretched and not-stretched) experienced approximately the same σ_{UTS} within each parallel, but the strain at failure experienced a lot more variation with no specific trend. The magnitude and particle distribution of intermetallic constituent particles are difficult to get totally homogeneously in extruded profiles. There will always exist a variation throughout all the tensile specimens tested. A possible cause to some of the variation in area fraction fracture strain can be variation in the volume fraction and size distribution of the constituent particles.

7.4 Improvement of ductility

The main motivation for this report is to improve the ductility of an extruded AA6063 profile. The ductility in this context is controlled by necking during tensile testing, and the aim is to improve the elongation fracture strain. This section is included to discuss the possibility of improvements based on the experimental results and literature. Due to the coronavirus outbreak and closing of NTNU, scheduled experiments to enlighten the areas discussed in this section, were aborted. Literature studies are therefore used to support the discussion of fracture anisotropy in tensile testing and the constituent particles influence on area fraction fracture strain.

The demand of better ductility put on the extruded AA6063 profile in this context is to increase the A_{50} value. The A_{50} value is the engineering fracture strain measured through tensile testing with an 50mm extensometer and a specific "dog bone" type flat tensile specimen. In tensile testing with flat specimens flow instability starts simultaneously with diffuse necking. When diffuse necking is initiated, local necking and failure is inevitable. Failure will occur rather quickly after diffuse necking. In order to improve the elongation to failure, the elongation to diffuse necking has to be improved. By improving the elongation to diffuse necking, the fracture strain also can be improved, as illustrated in Figure 7.2. The elongation to diffuse necking can be increased by increasing the work hardening capacity, which results in increased slope of the stress-strain curve.

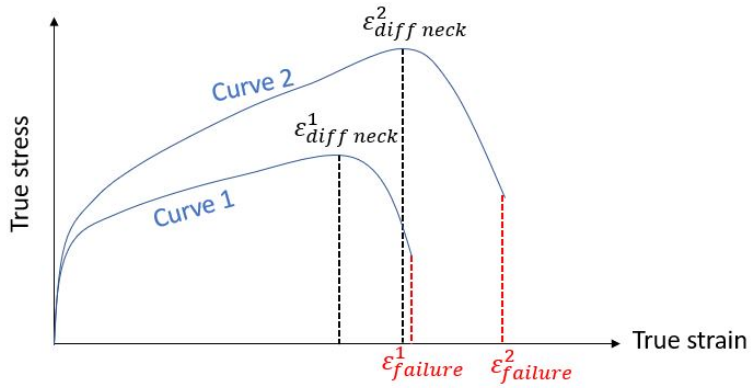

Figure 7.2: Curve 2 has a larger work hardening capacity than curve 1, which results in larger $\epsilon^2_{diffneck}$ than $\epsilon^1_{diffneck}$. This leads to a $\epsilon^2_{failure}$ larger than $\epsilon^1_{failure}$

Both the cooling rate and the storage at room temperature seems to have negligible effect on the elongation fracture strain in T4.

Fracture anisotropy was observed in tensile testing of AA6063[6, 31], where a DIC method measured the strains in the neck area onset of fracture. The highest fracture strain (measured by DIC) was observed in 90°to ED and the lowest was observed in 45°to ED[31]. The fracture strain obtained by measuring the strains by DIC in the neck area onset of fracture, is similar to the area fraction based fracture strain. Khadyko et al.[31] tested flat extruded profiles. The investigated profile in this report is of a more complex shape (shape shown in Figure 4.1a) than the profiles used in Khadyko et al.[31]. The complex shape can give a different metal flow in the material during extrusion than in Khadyko et al.[31]. The different metal flow can result in a different texture, which again can give another anisotropy. However very similar texture is found when comparing EBSD maps of the investigated profile (Figure 6.1) and the profile in Khadyko et al.[31]. Based on this it is reasonably to believe that the fracture anisotropy is the same in both profiles. Improved fracture strain may be expected in 90°to ED.

Both Hannard et al.[17] and Thomesen et al.[48] reported constituent particles to influence the area fraction based strain to fracture. Low particle fraction and small size of the constituent particles were concluded to be the cause of unexpectedly large area fraction fracture strain in AA6061-T6 experienced [48]. The ageing process occurs at low temperatures and the constituent particles will not be affected by the temperature, and thereby have the same effect in T4 as T6. The fracture mechanism in AA6061-T6 is found to be nucleation, growth and coalescence of void[48]. The same fracture mechanism is assumed to be working in AA6063-T4. Based on this it is reasonably to assume the constituent particles will affect the area fraction fracture strain in the AA6063-T4 profile in a similar way as AA6061-T6 in Thomesen et al.[48]. Area fraction fracture strain is then assumed to be improved by lowering the particle fraction and size of the constituent particles in the extruded AA6063-T4 profile.

8. Conclusion

The main objective of this report is to investigate ductility, which can be defined in multiple ways. In this context the main focus is put on elongation in tensile testing and the local fracture. The concluding remarks of the ductility investigation through tensile testing and microscopic investigations are listed below:

- The cooling rate of water is remarkably faster than the rate of air and oil. Water quenching reaches a temperature below the critical temperature of precipitate β-particles at 250°C after approximately 1 second. Oil quenched below 250°C 49 seconds and air quench in 1 minute and 38 seconds.

- Based on stress-strain curves and area fraction fracture strain measurements, neither the cooling rate nor storage at room temperature does affect the elongation to fracture in T4. The cooling rate and storage time seems to only effect the ultimate strength.

- A smaller ultimate stress is observed for the pre stretched specimens in T4 compared to the not-stretched specimens in T4. The pre stretched tensile specimens have a sharp elastic-plastic transition compared to the not-stretched specimens, which gives the stress-strain curve a distinct shape. A potential reason to the shape can be a composite effect introduced by the pre stretching, where gradually more grains become plastic during the elastic-plastic transition.

- All investigated fracture surfaces show dimples and a constituent particle is often found at the bottom of the dimple. EDS results reveal that the particles often contain Al and Fe with a varying amount of Mn, Mg and Si. Some pollution particles are also found, but the particles can descent from both the sample preparation and production. Publications indicate that these constituent particles largely influence the strain to failure.

- The observation of dimples and constituent particles in the tensile specimens indicate that the working fracture mechanism is nucleation, growth and coalescence of voids.

- Published results indicates some existing fracture anisotropy in AA6063-T6. A smaller particle fraction and size of the constituent particles can lead to lower strain to fracture according to recently published results. An increased work hardening capacity give increased elongation to diffuse necking, and this can potential lead to improved elongation to failure.

References

[1] European Aluminium. *Automotive and transport*. URL: https://www.european-aluminium.eu/about-aluminium/aluminium-in-use/automotive-and-transport/ (visited on 01/29/2020).

[2] M. Asano et al. "Effect of copper content on the bendability of Al-Mg-Si alloy sheet". In: *Aluminium Alloys 2006, Pts 1 And 2* 519-521 (2006). Publisher: TRANS TECH PUBLICATIONS LTD, pp. 771–776. ISSN: 0255-5476.

[3] Mineo ASANO, Hidetoshi UCHIDA, and Hideo YOSHIDA. "Effect of second phase particles on the bendability of an Al-Mg-Si alloy". In: *Effect of second phase particles on the bendability of an Al-Mg-Si alloy* 52.10 (2002). Num Pages: 5 Place: Tokyo Publisher: Keikinzoku Gakkai, c/o Hibiya Asahi Seimeikan, Keikinzoku Kyokai, pp. 448–452. ISSN: 0451-5994.

[4] R. J. Asaro and J. R. Rice. "Strain localization in ductile single crystals". In: *Journal of the Mechanics and Physics of Solids* 25.5 (Oct. 1, 1977), pp. 309–338. ISSN: 0022-5096. DOI: 10.1016/0022-5096(77)90001-1. URL: http://www.sciencedirect.com/science/article/pii/0022509677900011 (visited on 04/27/2020).

[5] Onur Cavusoglu, Alan Gordon Leacock, and Hakan Gürün. "Forming-limit diagrams and strain-rate-dependent mechanical properties of AA6019-T4 and AA6061-T4 aluminium sheet materials". In: *Materiali in tehnologije* 50.6 (Dec. 12, 2016), pp. 1005–1010. ISSN: 15802949, 15803414. DOI: 10.17222/mit.2015.259. URL: http://mit.imt.si/Revija/izvodi/mit166/cavusoglu.pdf (visited on 06/11/2020).

[6] Y. Chen et al. "An experimental study on the dynamic fracture of extruded AA6xxx and AA7xxx aluminium alloys". In: *Materials Science and Engineering: A* 523.1 (Oct. 15, 2009), pp. 253–262. ISSN: 0921-5093. DOI: 10.1016/j.msea.2009.06.007. URL: http://www.sciencedirect.com/science/article/pii/S0921509309006467 (visited on 04/28/2020).

[7] Y. Chen et al. "Stress–strain behaviour of aluminium alloys at a wide range of strain rates". In: *International Journal of Solids and Structures* 46.21 (Oct. 15, 2009), pp. 3825–3835. ISSN: 0020-7683. DOI: 10.1016/j.ijsolstr.2009.07.013. URL: http://www.sciencedirect.com/science/article/pii/S0020768309002716 (visited on 03/30/2020).

[8] S. H. Choi, F. Barlat, and J. Liu. "Effect of precipitates on plastic anisotropy for polycrystalline aluminum alloys". In: *Metallurgical and Materials Transactions A* 32.9 (Sept. 1, 2001), p. 2239. ISSN: 1543-1940. DOI: 10.1007/s11661-001-0199-2. URL: https://doi.org/10.1007/s11661-001-0199-2 (visited on 04/29/2020).

[9] L. Djapic Oosterkamp, A. Ivankovic, and G. Venizelos. "High strain rate properties of selected aluminium alloys". In: *Materials Science and Engineering: A* 278.1 (Feb. 15, 2000), pp. 225–235. ISSN: 0921-5093. DOI: 10.1016/S0921-5093(99)00570-5. URL: http://www.sciencedirect.com/science/article/pii/S0921509399005705 (visited on 05/06/2020).

[10] H.-E. Ekström et al. "Mechanical properties, texture and microstructure of flat AA6063 and AA6082 profiles". In: *Aluminium* 78 (2002), pp. 930–937.

[11] D. Eskine, J. Zuidema Jr, and L. Katgerman. "Linear solidification contraction of binary and commercial aluminium alloys". In: *International Journal of Cast Metals Research* 14.4 (Jan. 1, 2002). Publisher: Taylor & Francis _eprint: https://doi.org/10.1080/13640461.2002.11819440, pp. 217–223. ISSN: 1364-0461. DOI: 10.1080/13640461.2002.11819440. URL: https://doi.org/10.1080/13640461.2002.11819440 (visited on 05/27/2020).

[12] European Aluminium. *Aluminium in Cars: Unlocking the lightweighting potential*. URL: https://www.european-aluminium.eu/media/1326/aluminium-in-cars-unlocking-the-lightweighting-potential.pdf (visited on 01/30/2020).

[13] B. H. Frodal et al. "Influence of pre-compression on the ductility of AA6xxx aluminium alloys". In: *International Journal of Fracture* 206.2 (Aug. 1, 2017), pp. 131–149. ISSN: 1573-2673. DOI: 10.1007/s10704-017-0204-4. URL: https://doi.org/10.1007/s10704-017-0204-4 (visited on 05/18/2020).

[14] Guoqing Geng et al. "A modified Johnson-Cook model of 6061-T6 Aluminium profile". In: *Australian Journal of Mechanical Engineering* (Jan. 31, 2020). Place: Abingdon Publisher: Taylor & Francis Ltd WOS:000511985300001. ISSN: 1448-4846. DOI: 10.1080/14484846.2020.1721966.

[15] George E. Dieter. *Mechanical metallurgy*. In collab. with David Bacon. SI metric ed. McGraw-Hill series in materials science and engineering. London: McGraw-Hill, 1988. xxiii+751. ISBN: 978-0-07-084187-1.

[16] Günter Gottstein. *Physical foundations of materials science*. Berlin: Springer, 2004. xiv+502. ISBN: 978-3-540-40139-1.

[17] F. Hannard et al. "Characterization and micromechanical modelling of microstructural heterogeneity effects on ductile fracture of 6xxx aluminium alloys". In: *Acta Materialia* 103 (Jan. 15, 2016), pp. 558–572. ISSN: 1359-6454. DOI: 10.1016/j.actamat.2015.10.008. URL: http://www.sciencedirect.com/science/article/pii/S1359645415300094 (visited on 12/27/2019).

[18] R. Hill. "A general theory of uniqueness and stability in elastic-plastic solids". In: *Journal of the Mechanics and Physics of Solids* 6.3 (May 1, 1958), pp. 236–249. ISSN: 0022-5096. DOI: 10.1016/0022-5096(58)90029-2. URL: http://www.sciencedirect.com/science/article/pii/0022509658900292 (visited on 04/27/2020).

[19] R. Hill and J. W. Hutchinson. "Bifurcation phenomena in the plane tension test". In: *Journal of the Mechanics and Physics of Solids* 23.4 (Aug. 1, 1975), pp. 239–264. ISSN: 0022-5096. DOI: 10.1016/0022-5096(75)90027-7. URL: http://www.sciencedirect.com/science/article/pii/0022509675900277 (visited on 04/27/2020).

[20] J. Hjelen. *Electron BackScatter Diffraction EBSD in SEM*. Trondheim: NTNU, 2007.

[21] J. Hjelen. *Scanning elektron-mikroskopi*. SINTEF, 1986.

[22] Bjørn Holmedal. *Lecture notes TMT4266 Metal Fabrication and Forming - Microstructure and Crystal Plasticity*.

[23] William F. Hosford. *Iron and Steel*. Cambridge: Cambridge University Press, 2012. ISBN: 978-1-107-01798-6. DOI: 10.1017/CBO9781139086233. URL: https://www.cambridge.org/core/books/iron-and-steel/9C6877062E338222979D768E3C647C0F (visited on 05/23/2020).

[24] William F. Hosford and Robert M. Caddell. *Metal forming - mechnics and metallurgy*. Second edition. Upper Saddle River, NJ 07458: PTR Prentice Hall.

[25] Shingo IKAWA et al. "Effect of texture variation through sheet thickness on bendability in aluminum alloy sheet". In: *Effect of texture variation through sheet thickness on bendability in aluminum alloy sheet* 61.2 (2011). Num Pages: 7 Place: Tokyo Publisher: Keikinzoku Gakkai, c/o Hibiya Asahi Seimeikan, Keikinzoku Kyokai, pp. 53–59. ISSN: 0451-5994.

[26] Shingo Ikawa et al. "Effects of crystal orientation on bendability of aluminum alloy sheet". In: *Materials Science and Engineering: A* 528.12 (May 15, 2011), pp. 4050–4054. ISSN: 0921-5093. DOI: 10.1016/j.msea.2011.01.048. URL: http://www.sciencedirect.com/science/article/pii/S0921509311000700 (visited on 03/16/2020).

[27] Terje Iveland. "Anisotropic plasticity of AlZnMg extrusions: an experimental approach". ISBN: 9788279840855 Pages: X, 236, 19 Series: Doktor ingeniøravhandling (Trondheim : trykt utg.) Volume: 2000:60. PhD thesis. Trondheim: Norges teknisk-naturvitenskapelige universitet, Institutt for materialteknologi og elektrokjemi, 2000. URL: http://urn.nb.no/URN:NBN:no-nb_digibok_2009121100028 (visited on 04/30/2020).

[28] J. R Davis. *Tensile testing*. 2nd ed. Materials Park, Ohio: ASM International, 2004. 291 pp. ISBN: 978-1-61503-095-8.

[29] S. M. Keralavarma, A. F. Bower, and W. A. Curtin. "Quantum-to-continuum prediction of ductility loss in aluminium–magnesium alloys due to dynamic strain aging". In: *Nature Communications* 5.1 (Aug. 4, 2014). Number: 1 Publisher: Nature Publishing Group, p. 4604. ISSN: 2041-1723. DOI: 10.1038/ncomms5604. URL: https://www.nature.com/articles/ncomms5604 (visited on 06/12/2020).

[30] M. Khadyko et al. "Effects of heat-treatment on the plastic anisotropy of extruded aluminium alloy AA6063". In: *Materials Science and Engineering a-Structural Materials Properties Microstructure and Processing* 708 (Dec. 21, 2017). WOS:000415770100021, pp. 208–221. ISSN: 0921-5093. DOI: 10.1016/j.msea.2017.09.133.

[31] M. Khadyko et al. "Tensile ductility of extruded aluminium alloy AA6063 in different tempers". In: *Materials Science and Engineering a-Structural Materials Properties Microstructure and Processing* 744 (Jan. 28, 2019). WOS:000457510300053, pp. 500–511. ISSN: 0921-5093. DOI: 10.1016/j.msea.2018.12.048.

[32] U. Kocks. "The relation between polycrystal deformation and single-crystal deformation". In: *Metallurgical and Materials Transactions* 1.5 (1970). Place: New York Publisher: Springer-Verlag, pp. 1121–1143. ISSN: 0360-2133. DOI: 10.1007/BF02900224.

[33] Mitsutoshi Kuroda and Viggo Tvergaard. "Effects of texture on shear band formation in plane strain tension/compression and bending". In: *International Journal of Plasticity* 23.2 (Feb. 1, 2007), pp. 244–272. ISSN: 0749-6419. DOI: 10.1016/j.ijplas.2006.03.014. URL: http://www.sciencedirect.com/science/article/pii/S0749641906000751 (visited on 04/27/2020).

[34] Daoming Li and Amit Ghosh. "Tensile deformation behavior of aluminum alloys at warm forming temperatures". In: *Materials Science and Engineering: A* 352.1 (July 15, 2003), pp. 279–286. ISSN: 0921-5093. DOI: 10.1016/S0921-5093(02)00915-2. URL: http://www.sciencedirect.com/science/article/pii/S0921509302009152 (visited on 06/11/2020).

[35] G. Liu et al. "Coupling effect of primary voids and secondary voids on the ductile fracture of heat-treatable aluminum alloys". In: *Mechanics of Materials* 43.10 (Oct. 1, 2011), pp. 556–566. ISSN: 0167-6636. DOI: 10.1016/j.mechmat.2011.06.014. URL: http://www.sciencedirect.com/science/article/pii/S0167663611001098 (visited on 05/01/2020).

[36] D. J Lloyd. "The scaling of the tensile ductile fracture strain with yield strength in Al alloys". In: *Scripta Materialia* 48.4 (Feb. 1, 2003), pp. 341–344. ISSN: 1359-6462. DOI: 10.1016/S1359-6462(02)00455-4. URL: http://www.sciencedirect.com/science/article/pii/S1359646202004554 (visited on 06/02/2020).

[37] Jeremy K. Mason and Christopher A. Schuh. "Representations of Texture". In: *Electron Backscatter Diffraction in Materials Science*. Ed. by Adam J. Schwartz et al. Boston, MA: Springer US, 2009, pp. 35–51. ISBN: 978-0-387-88136-2. DOI: 10.1007/978-0-387-88136-2_3. URL: https://doi.org/10.1007/978-0-387-88136-2_3 (visited on 03/06/2020).

[38] T. Minoda, M. Asano, and H. Yoshida. "Influence of iron content on the mechanical properties of AA6016 alloy sheet." In: *Materials Science Forum* 519-521 (2006). In collab. with T. Minoda, pp. 859–864. ISSN: 0255-5476.

[39] Waqas Muhammad et al. "A criterion for ductile failure in age-hardenable aluminum alloys". In: *Materials Science and Engineering: A* 759 (June 24, 2019), pp. 613–623. ISSN: 0921-5093. DOI: 10.1016/j.msea.2019.05.055. URL: http://www.sciencedirect.com/science/article/pii/S0921509319306781 (visited on 04/28/2020).

[40] K. O. Pedersen et al. "Strength and ductility of aluminium alloy AA7030". In: *Materials Science and Engineering: A* 473.1 (Jan. 25, 2008), pp. 81–89. ISSN: 0921-5093. DOI: 10.1016/j.msea.2007.03.089. URL: http://www.sciencedirect.com/science/article/pii/S0921509307005837 (visited on 05/19/2020).

[41] Ketill O. Pedersen et al. "Influence of microstructure on work-hardening and ductile fracture of aluminium alloys". In: *Materials & Design* 70 (Apr. 5, 2015), pp. 31–44. ISSN: 0261-3069. DOI: 10.1016/j.matdes.2014.12.035. URL: http://www.sciencedirect.com/science/article/pii/S026130691401019X (visited on 05/28/2020).

[42] A. D. Rollett, Gregory S. Rohrer, and F. J. Humphreys. *Recrystallization and Related Annealing Phenomena*. Third edition. Elsevier, 2017. ISBN: 978-0-08-098235-9.

[43] Øyvind Ryen. *Work Hardening and Mechanical Anisotropy of Aluminium Sheets and Profiles*. Accepted: 2014-12-19T13:10:43Z Publication Title: 191. Fakultet for naturvitenskap og teknologi, 2003. ISBN: 978-82-471-5660-5. URL: https://ntnuopen.ntnu.no/ntnu-xmlui/handle/11250/244466 (visited on 04/28/2020).

[44] Robert A. Schwarzer et al. "Present State of Electron Backscatter Diffraction and Prospective Developments". In: *Electron Backscatter Diffraction in Materials Science*. Ed. by Adam J. Schwartz et al. Boston, MA: Springer US, 2009, pp. 1–20. ISBN: 978-0-387-88136-2. DOI: 10.1007/978-0-387-88136-2_1. URL: https://doi.org/10.1007/978-0-387-88136-2_1 (visited on 03/08/2020).

[45] Knut Erik Snilsberg. "Mikrostruktur og mekaniske egenskaper for 7xxx-legeringer". Master thesis. Trondheim: NTNU, June 17, 2009.

[46] Anders Søreng. "Localized deformation and mechanical anisotropy in aluminium and AlZnMg alloys". ISBN: 9788247101087 Pages: X, 254, 17 Series: Doktor ingeniøravhandling (Trondheim : trykt utg.) Volume: 1997:74. PhD thesis. Trondheim: Norges teknisk-naturvitenskapelige universitet, Metallurgisk institutt, 1997.

[47] G.I Taylor. "Plastic strain in metals". In: *J. Inst. Met.* 62 (1938), pp. 307–324.

[48] Susanne Thomesen et al. "Influence of stress state on plastic flow and ductile fracture of three 6000-series aluminium alloys". In: *Materials Science and Engineering: A* 783 (May 5, 2020), p. 139295. ISSN: 0921-5093. DOI: 10.1016/j.msea.2020.139295. URL: http://www.sciencedirect.com/science/article/pii/S0921509320303774 (visited on 05/28/2020).

[49] Tor A. Fjeldly. "Deformation properties of solution heat treated AlZnMg extruded profiles". ISBN: 9788279840169 Pages: XII, 192 Series: Doktor ingeniøravhandling (Trondheim : trykt utg.) Volume: 1999:134. PhD thesis. Trondheim: Norges teknisk-naturvitenskapelige universitet, Institutt for materialteknologi og elektrokjemi, 1999.

[50] *Transformation of a tensor to a new coordinate system – RockMechs*. Library Catalog: www.rockmechs.com. URL: https://www.rockmechs.com/tensor-transformation-rotation/ (visited on 05/21/2020).

[51] H. E. Vatne, T. Furu, and E. Nes. "Nucleation of recrystallised grains from cube bands in hot deformed commercial purity aluminium". In: *Materials Science and Technology* 12.3 (1996). Publisher: Maney Publishing, pp. 201–210. ISSN: 0267-0836. DOI: 10.1179/mst.1996.12.3.201.

[52] Ida Westermann et al. "Effects of particles and solutes on strength, work-hardening and ductile fracture of aluminium alloys". In: *Mechanics of Materials* 79 (Dec. 1, 2014), pp. 58–72. ISSN: 0167-6636. DOI: 10.1016/j.mechmat.2014.08.006. URL: http://www.sciencedirect.com/science/article/pii/S0167663614001628 (visited on 06/02/2020).

[53] K. Zhang et al. "Assessment of advanced Taylor models, the Taylor factor and yield-surface exponent for FCC metals". In: *International Journal of Plasticity* 114 (Mar. 1, 2019), pp. 144–160. ISSN: 0749-6419. DOI: 10.1016/j.ijplas.2018.10.015. URL: http://www.sciencedirect.com/science/article/pii/S0749641918301980 (visited on 03/24/2020).

[54] Hao Zhong et al. "Effect of pre-ageing on dynamic strain ageing in Al-Mg-Si alloys". In: *Materials Science and Engineering: A* 687 (Feb. 27, 2017), pp. 323–331. ISSN: 0921-5093. DOI: 10.1016/j.msea.2017.01.051. URL: http://www.sciencedirect.com/science/article/pii/S0921509317300722 (visited on 03/24/2020).

Appendix

A. Excerpt from author's project work

A.1 Extensometer

Engineering strain is given by equation A.1

$$e = \frac{l - l_0}{l_0} \tag{A.1}$$

where l is the instantaneous length measured by the extensometer and l_0 is the original length. After necking the strain and ϵ_f is effected by the size of the extensometer. In figure A.1 at necking the tensile specimen obtain an elongation $\Delta l = \Delta L_{neck}$ at extensometer 1 giving rise to $\epsilon_{Extensometer1}$. With a larger extensometer, extensometer 2, there is an area L_x where nothing happens and the same elongation, ΔL_{neck}, is measured, but l_0 increases giving rise to $\epsilon_{Extensometer2}$. $\epsilon_{Extensometer1} > \epsilon_{Extensometer2}$, with a larger extensometer, l_0 in equation A.1 goes to infinity and a shorter ϵ_f is obtained and another tensile curve will appear, see figure A.2.

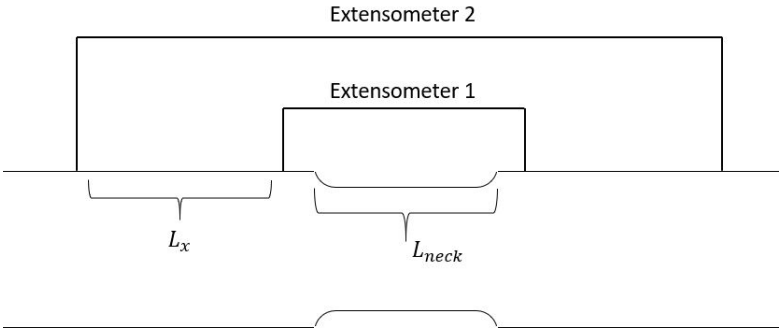

Figure A.1: Sensitivity of the extensometer

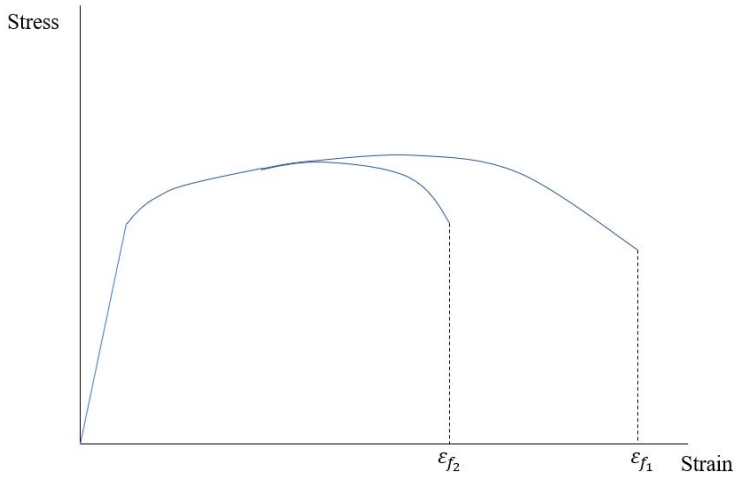

Figure A.2: Difference in ϵ_f values for different extensometer length

B. Matlab script used for measuring and calculation of true fracture strain

The Matlab script is made by Egil Fagerholt in connection to Snilsberg's master thesis[45].

```
clear
close all
clc

mm2_per_pixel = power(2/296,2);
%I = imread('C:\Documents and Settings\egilf\My
%Documents\Areal_strekkstaver\6060-45-1.jpg');

[filename, pathname] = uigetfile('*.jpg', 'Pick a JPG-file');
I = imread([pathname filename]);
figure(1)
subimage(I)
%set(gcf,'Position',[100, 100, 1200, 1000]);
hold on
[x(1),y(1)] = ginput(1);
plot(x,y,'r*')
count = 2
while(1)
 [x(count),y(count)] = ginput(1);
 plot(x,y,'r*-')
 dx = x(count)-x(1);
 dy = y(count)-y(1);
 dr = sqrt(dx*dx + dy*dy);
 if(dr<10),
 break;
 end
 count = count +1;
end
mask = roipoly(I, x, y);
pixCount = 0;
for i=1:length(mask(:,1)),
 for j=1:length(mask(1,:)),
 if(mask(i,j) == 1),
 I(i,j,1) = I(i,j,1);
 I(i,j,2) = ceil(0.5 * I(i,j,2));
 I(i,j,3) = ceil(0.5 * I(i,j,3));
 pixCount = pixCount + 1;
 end
 end
end
area_mm2 = pixCount*mm2_per_pixel;
title(['Nr. of Pixels: ' num2str(pixCount) ', Calulated Area: '
num2str(area_mm2) ' mm2']);
subimage(I)
plot(x,y,'r*-')
```

Figure B.1: Script used for calculation of area in true fracture strain

C. Fracture surface in SEM

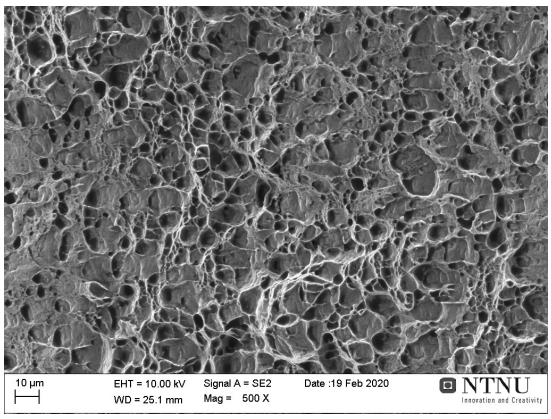

(a) 500x magnification, not-stretched.

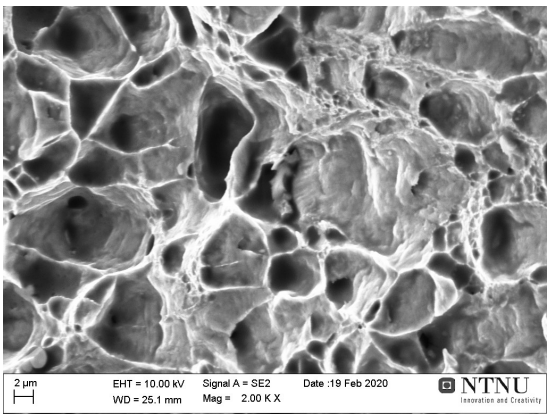

(b) 2000x magnification, not-stretched.

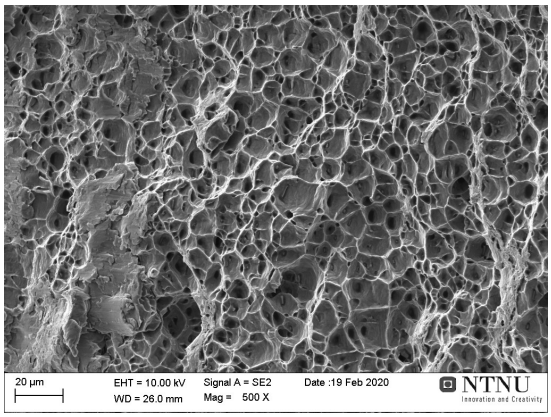

(c) 500x magnification, pre stretched.

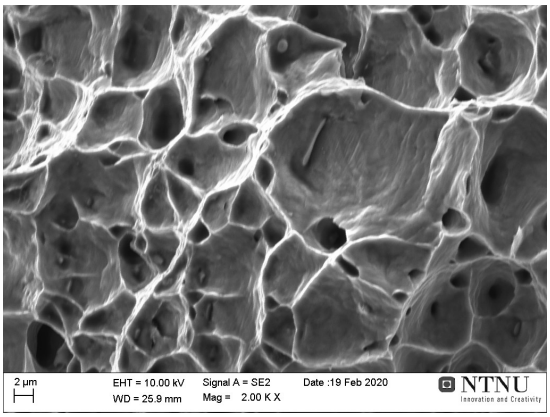

(d) 2000x magnification, pre stretched.

Figure C.1: Fracture surface of air cooled tensile specimens stored for 24 hour at room temperature before testing. Figure C.1a and C.1b are not-stretched and Figure C.1c and C.1d are pre stretched 0.5% after air cooling.

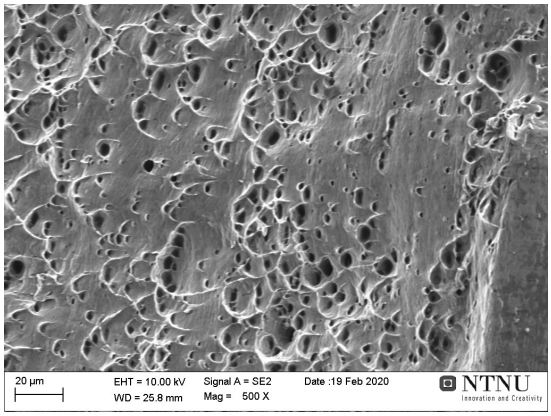

(a) 500x magnification, not-stretched.

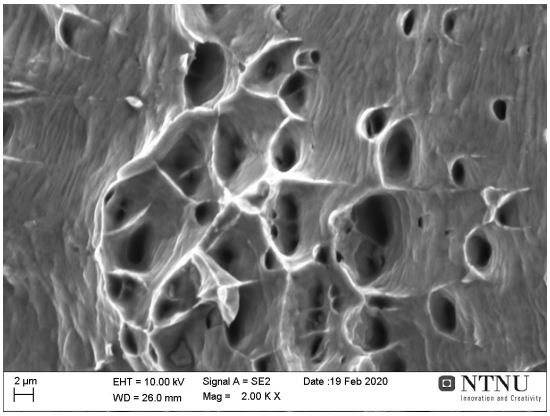

(b) 2000x magnification, not-stretched.

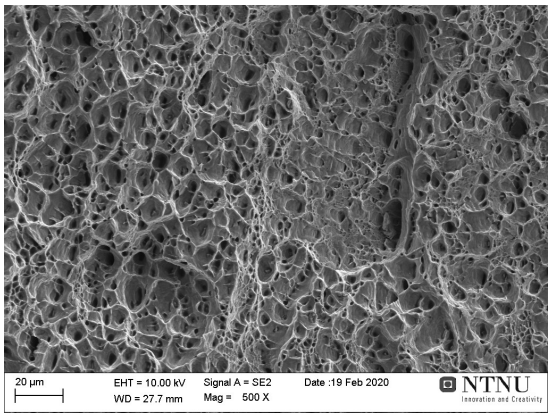

(c) 500x magnification, pre stretched.

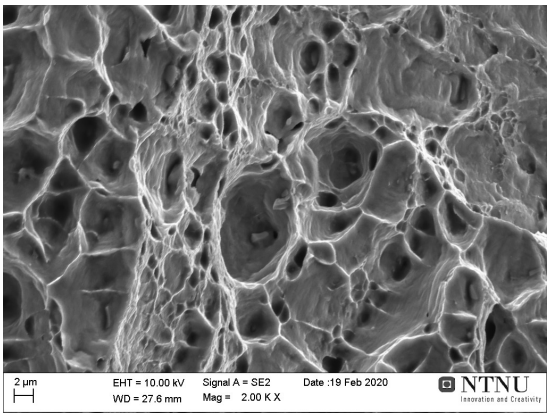

(d) 2000x magnification, pre stretched.

Figure C.2: Fracture surface of water cooled tensile specimens stored for 24 hour at room temperature before testing. Figure C.2a and C.2b are not-stretched and Figure C.2c and C.2d are pre stretched 0.5% after water cooling.

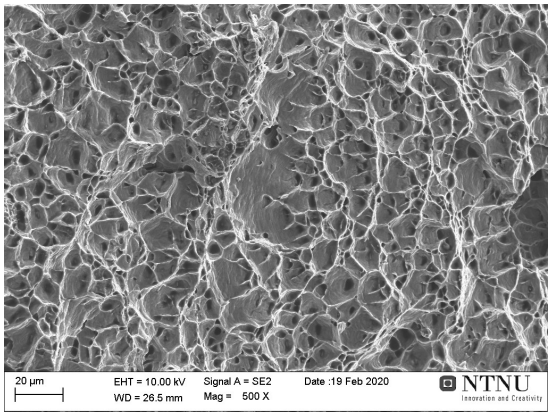

(a) 500x magnification, not-stretched.

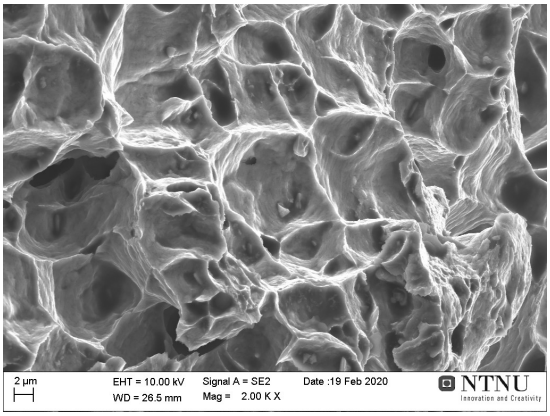

(b) 2000x magnification, not-stretched.

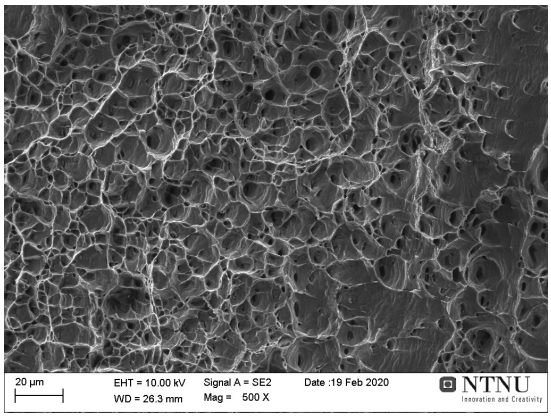

(c) 500x magnification, pre stretched.

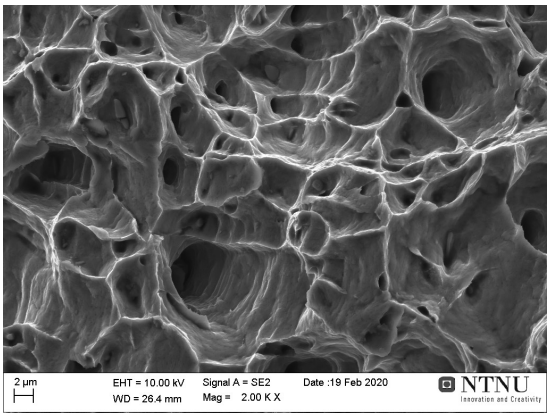

(d) 2000x magnification, pre stretched.

Figure C.3: Fracture surface of air cooled tensile specimens stored for 7 days at room temperature before testing. Figure C.3a and C.3b are not-stretched and Figure C.3c and C.3d are pre stretched 0.5% after air cooling.

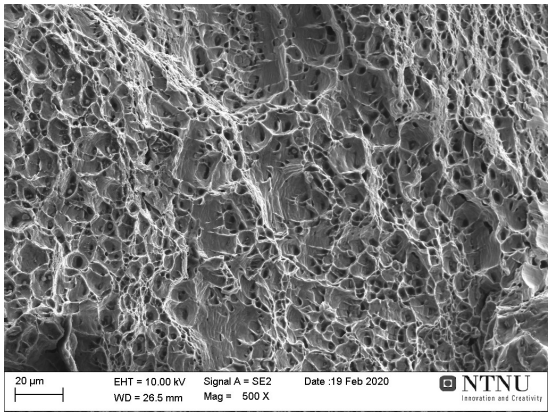

(a) 500x magnification, not-stretched.

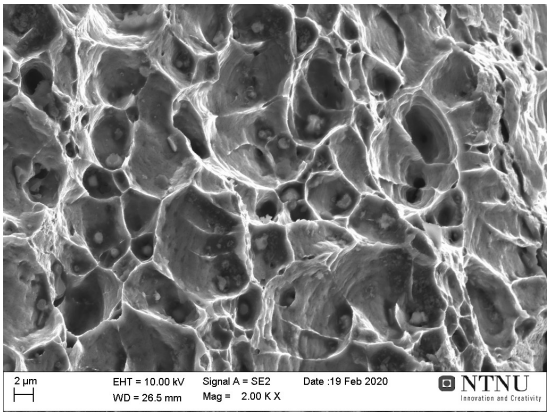

(b) 2000x magnification, not-stretched.

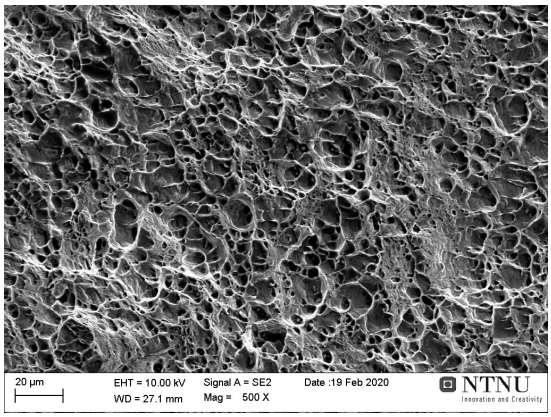

(c) 500x magnification, pre stretched.

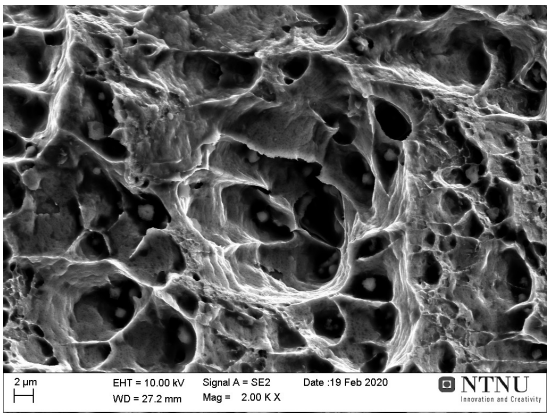

(d) 2000x magnification, pre stretched.

Figure C.4: Fracture surface of water cooled tensile specimens stored for 7 days at room temperature before testing. Figure C.4a and C.4b are not-stretched and Figure C.4c and C.4d are pre stretched 0.5% after water cooling.

D. EDS analysis of fracture surface tensile tests

D.1 Air cooled not-stretched tensile specimen stored for 24hours fracture area 1

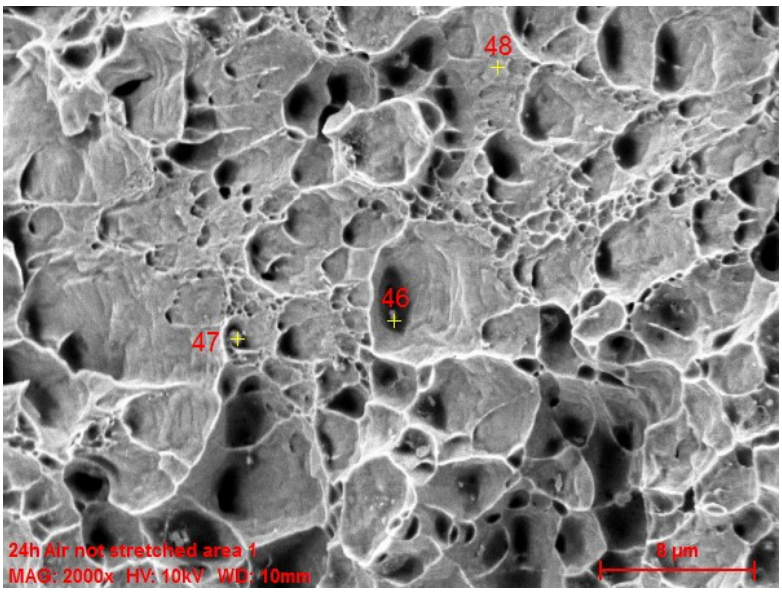

(a) SEM image of fracture area 1 in a not-stretched air cooled tensile specimen stored for 24 hours at room temperature.

Element given in $[wt\%]$	Al	O	Mg	Ti	Fe	Mn	Si	K	S	Ca	Na	C	Cl
46	55.78	0.79	2.35	2.62	7.66	5.14	0	10.88	6.22	5.60	2.75	0	0.20
47	8.87	0.99	0.15	0	1.13	1.43	0	48.69	0.32	-	0.75	0.54	37.23
48	97.66	0.56	1.28	0	0	0	0.32	0	0	0.01	0.15	0	0.02

Figure D.1: SEM image of fracture area 1 in a not-stretched air cooled specimen stored for 24 hours. Chemical analysis as nominative chemical composition of points in the SEM image is given in the table below, obtained by EDS.

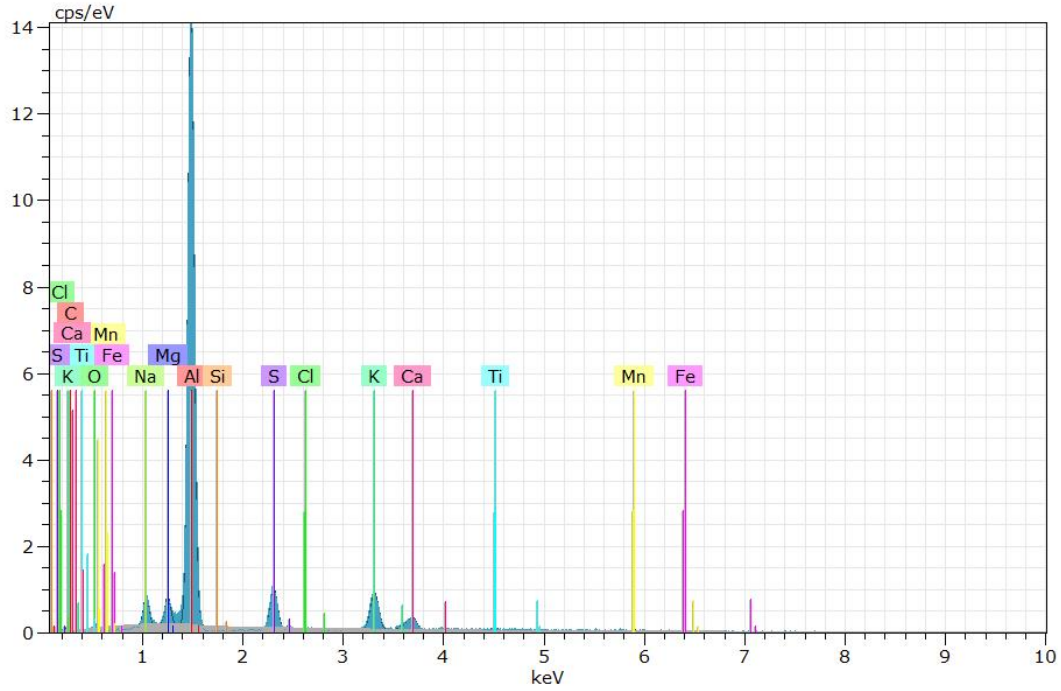

(a) Intensity spectrum of point 46

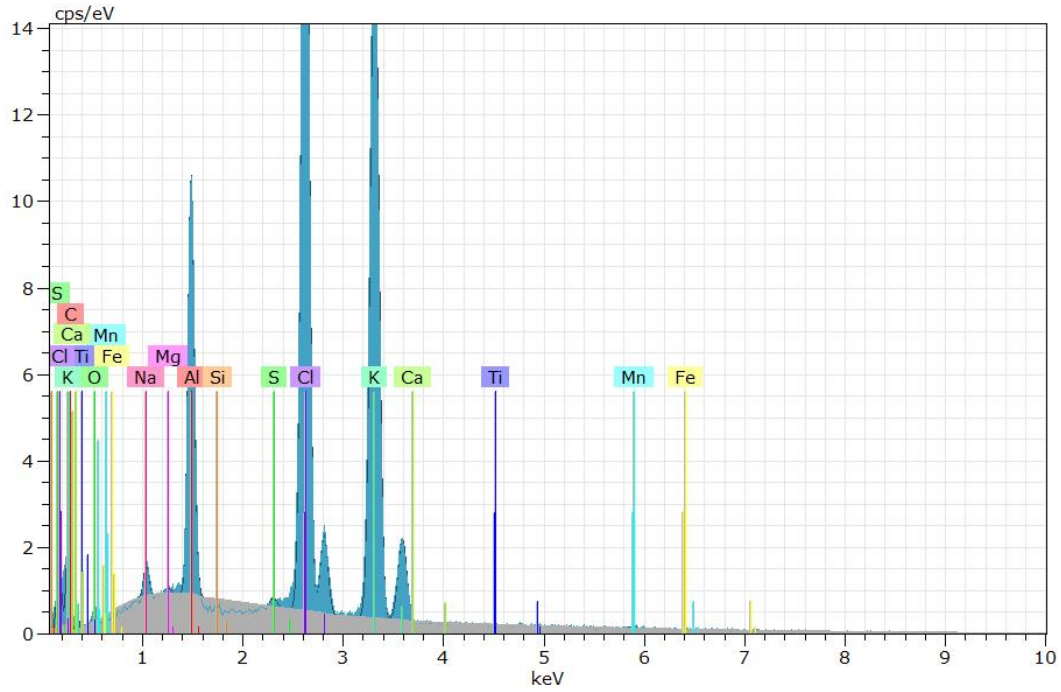

(b) Intensity spectrum of point 47

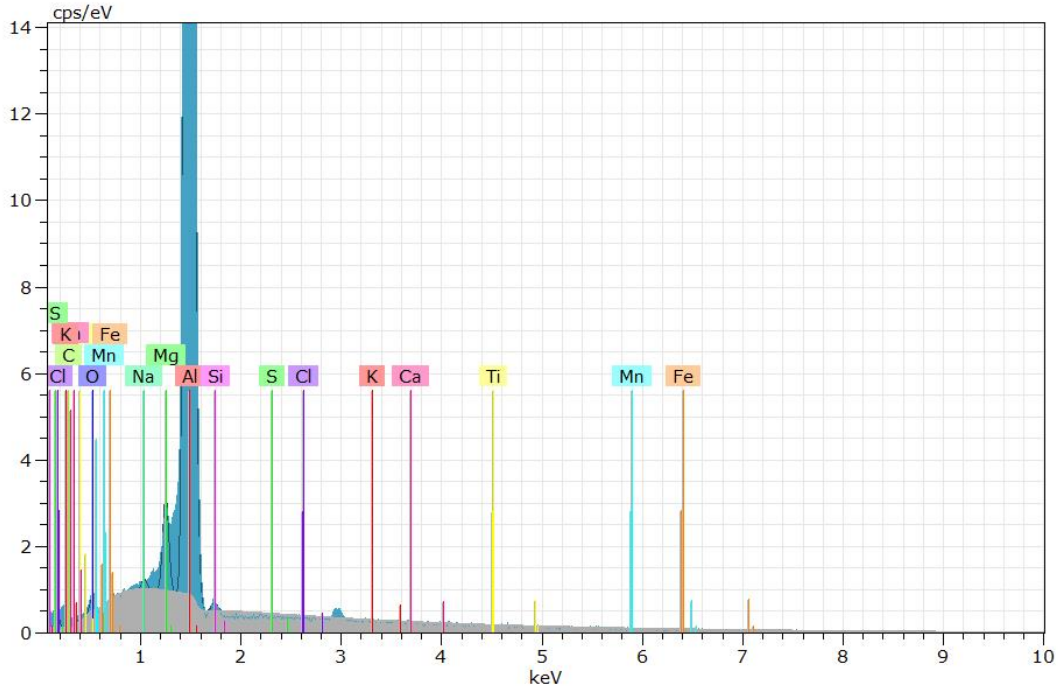

(c) Intensity spectrum of point 48

Figure D.2: Intensity spectrum of the points in Figure D.1a

D.2 Air cooled not-stretched tensile specimen stored for 24hours fracture area 2

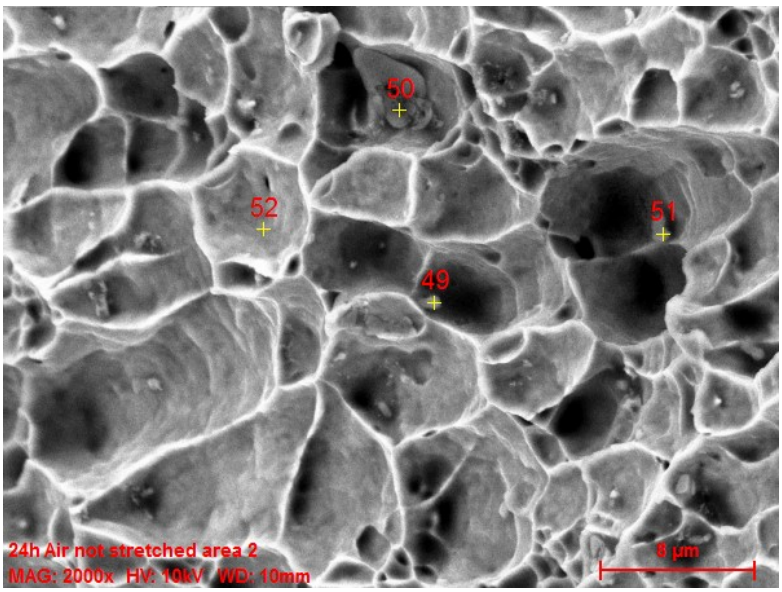

(a) SEM image of fracture area 2 in a not-stretched air cooled tensile specimen stored for 24 hours at room temperature.

Element given in $[wt\%]$	Al	O	Mg	Ti	Fe	Mn	Si	K	S	Ca	Na	C	Cl
49	77.47	0	1.62	2.40	6.04	4.31	0	4.33	0.27	2.74	0.80	0.01	0
50	75.99	0	1.35	1.76	4.86	3.22	0	7.64	0.08	1.40	0.67	0.14	2.88
51	71.66	0	1.20	0.02	11.94	9.14	0	2.32	0.04	3.44	0.24	0	0
52	95.37	1.52	1.43	0.02	0.03	0	0.68	0.08	0.05	0.12	0.38	0.33	0

Figure D.3: SEM image of fracture area 2 in a not-stretched air cooled specimen stored for 24 hours. Chemical analysis as nominative chemical composition of points in the SEM image is given in the table below, obtained by EDS.

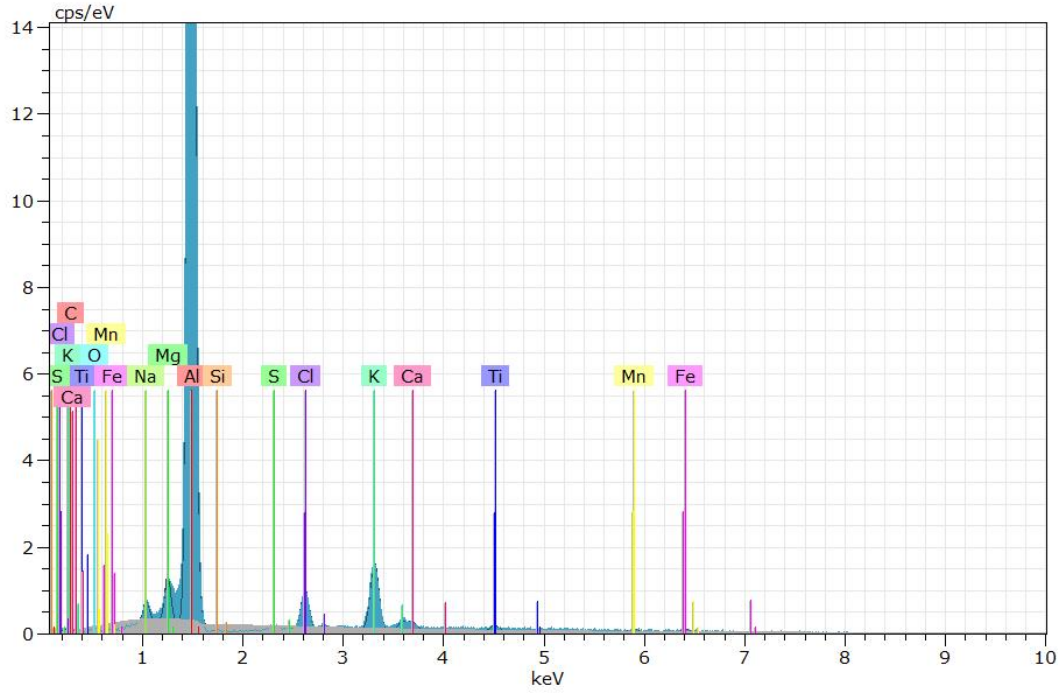

(a) Intensity spectrum of point 50

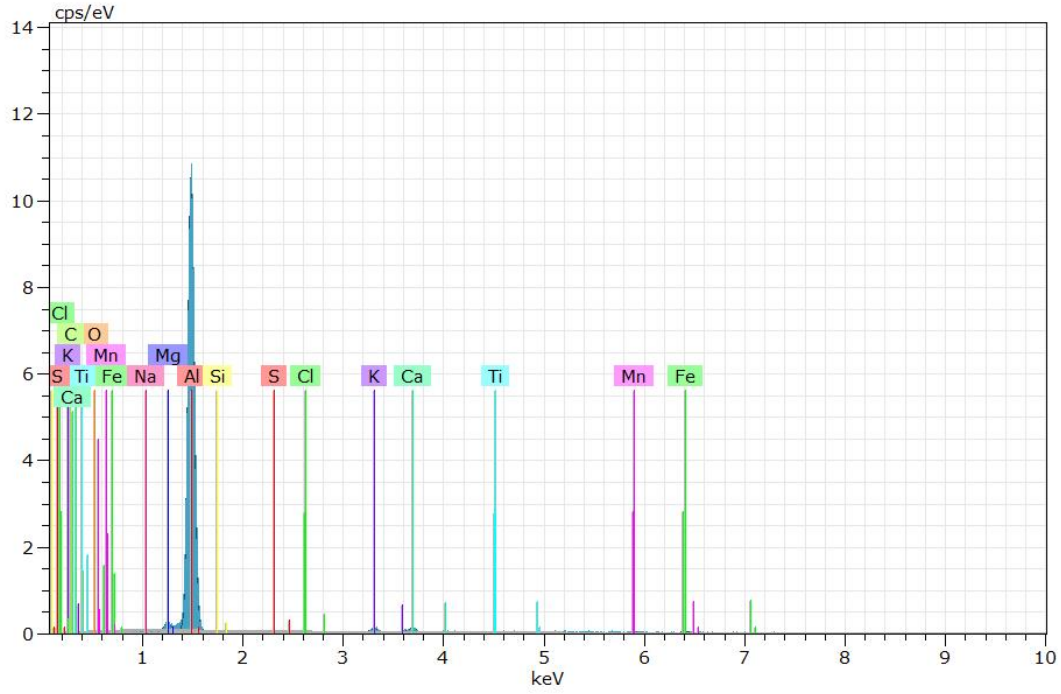

(b) Intensity spectrum of point 51

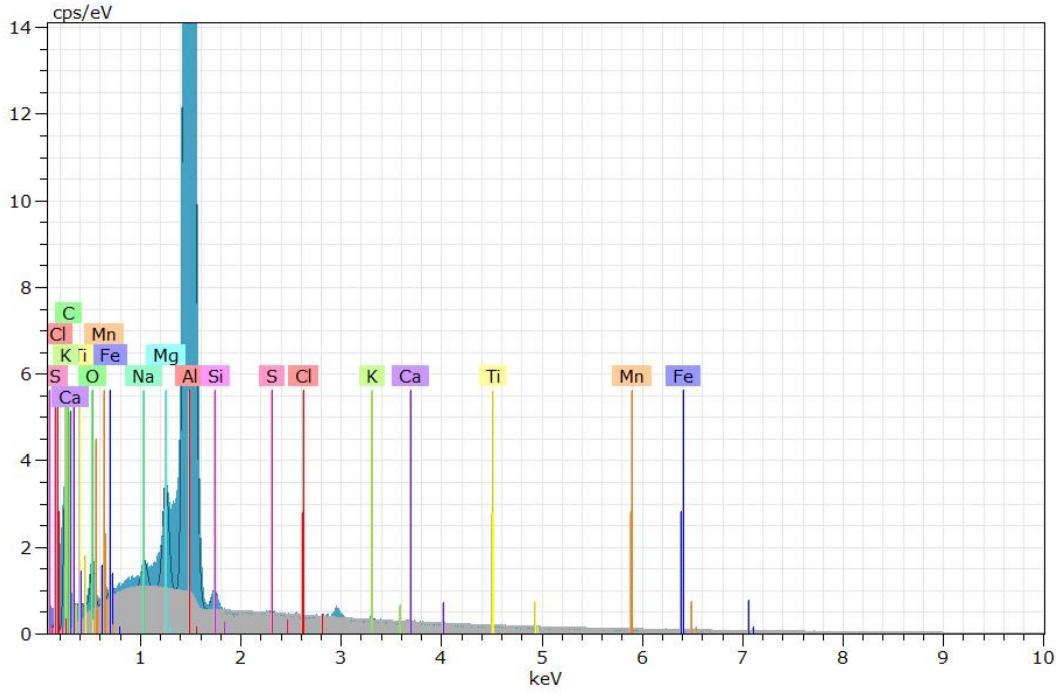

(c) Intensity spectrum of point 52

Figure D.4: Intensity spectrum of points in Figure D.3a

D.3 Air cooled pre stretched tensile specimen stored for 24hours fracture area 1

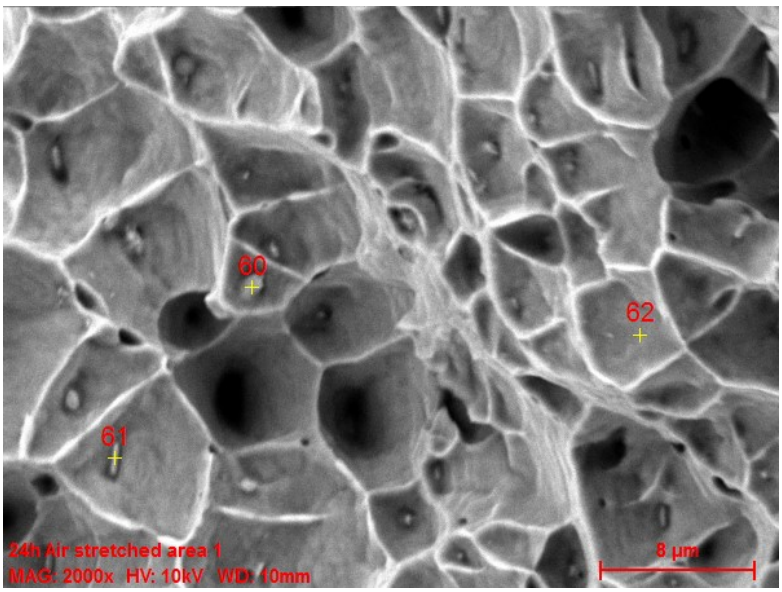

(a) SEM image of fracture area 1 in a pre stretched air cooled tensile specimen stored for 24 hours at room temperature.

Element given in $[wt\%]$	Al	O	Mg	Ti	Fe	Mn	Si	K	S	Ca	Na	C	Cl
60	65.92	0	1.01	0.82	26.01	4.85	0.53	0.14	0	0.41	0.32	0	0
61	75.16	0.40	1.10	0.23	16.84	2.89	3.08	0.04	0	0	0.25	0	0
62	96.96	0.49	1.38	0.03	0.40	0	0.46	0	0	0	0.28	0	0

Figure D.5: SEM image of fracture area 1 in a pre stretched air cooled specimen stored for 24 hours. Chemical analysis as nominative chemical composition of points in the SEM image is given in the table below, obtained by EDS.

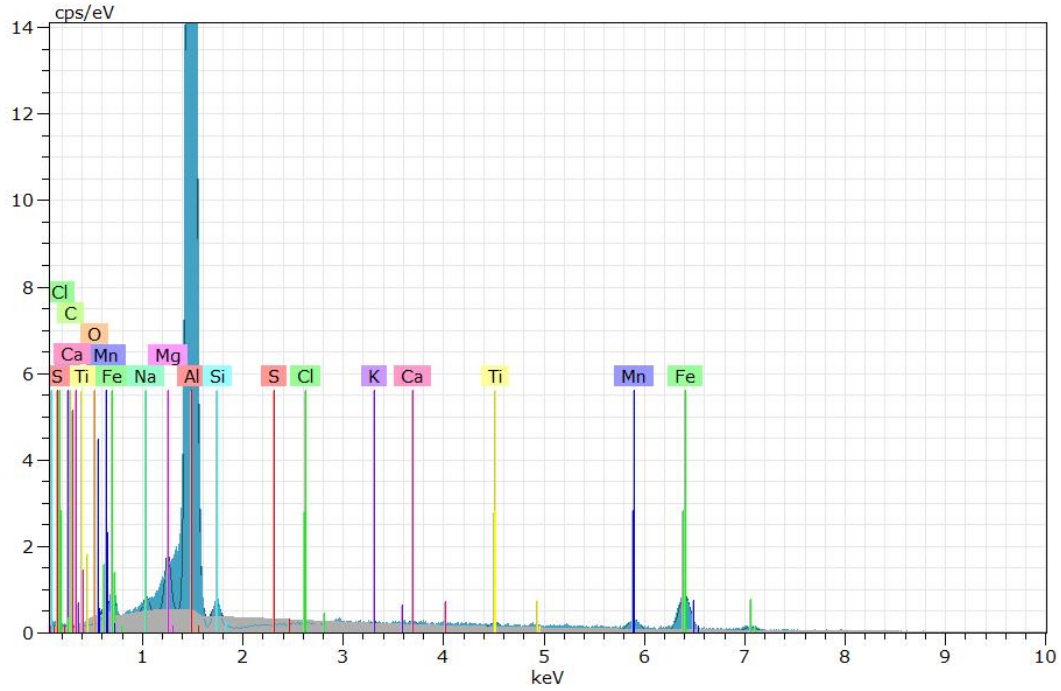

(a) Intensity spectrum of point 60

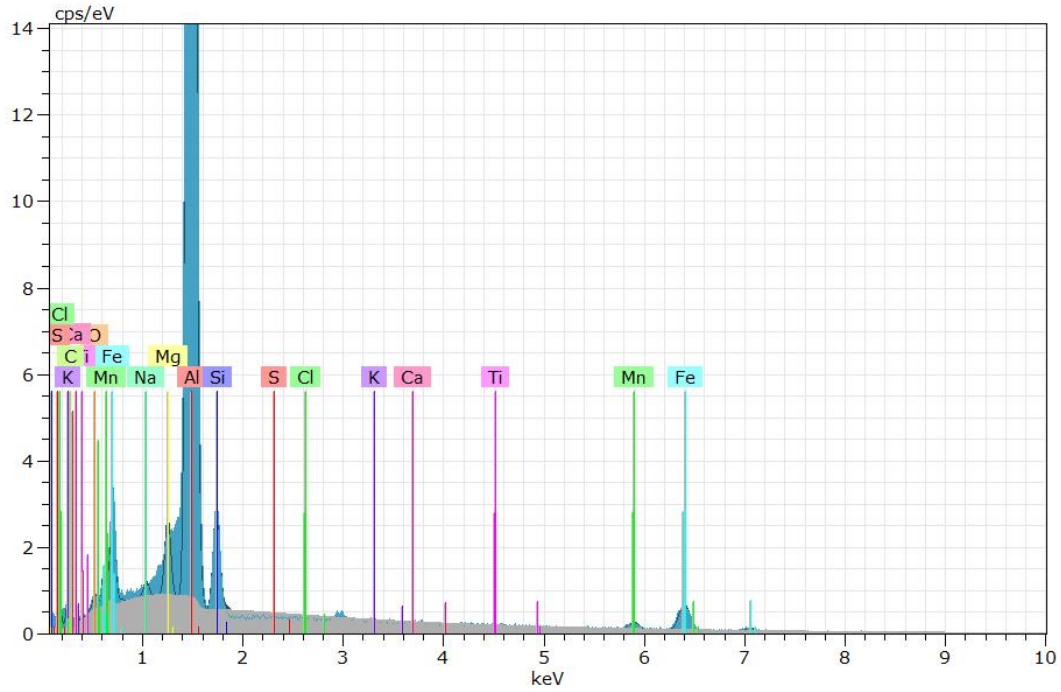

(b) Intensity spectrum of point 61

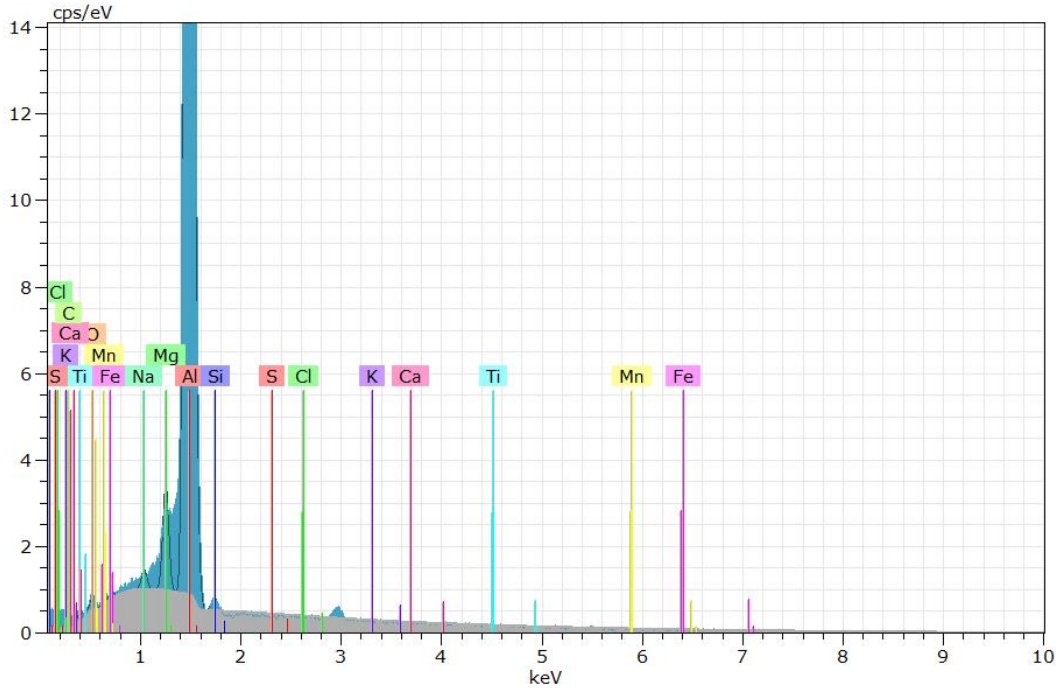

(c) Intensity spectrum of point 62

Figure D.6: Intensity spectrum of the points in Figure D.5a

D.4 Air cooled pre stretched tensile specimen stored for 24 hours fracture area 2

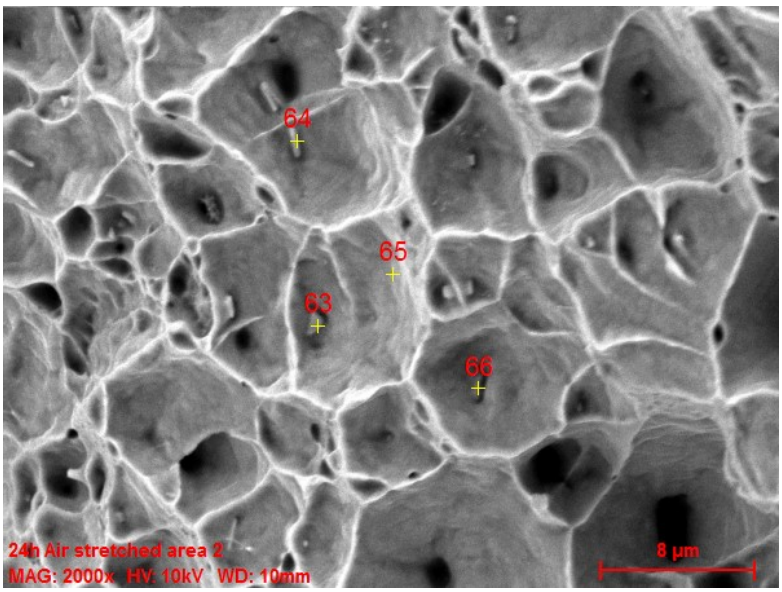

(a) SEM image of fracture area 2 in a pre stretched air cooled tensile specimen stored for 24 hours at room temperature.

Element given in $[wt\%]$	Al	O	Mg	Ti	Fe	Mn	Si	K	S	Ca	Na	C	Cl
63	74.26	0	1.17	0.75	19.36	3.58	0	0.03	0.02	0.49	0.17	0	0.17
64	97.13	0.33	1.33	0.01	0.32	0.13	0.46	0	0	0.08	0.19	0	0.03
65	90.62	0.12	1.23	1.15	3.85	2.55	0	0.03	0.01	0.32	0.12	0	0.01
66	66.64	0	0.91	1.77	22.73	7.05	0	0.05	0.01	0.86	0	0	0

Figure D.7: SEM image of fracture area 2 in a pre stretched air cooled specimen stored for 24 hours. Chemical analysis as nominative chemical composition of points in the SEM image is given in the table below, obtained by EDS.

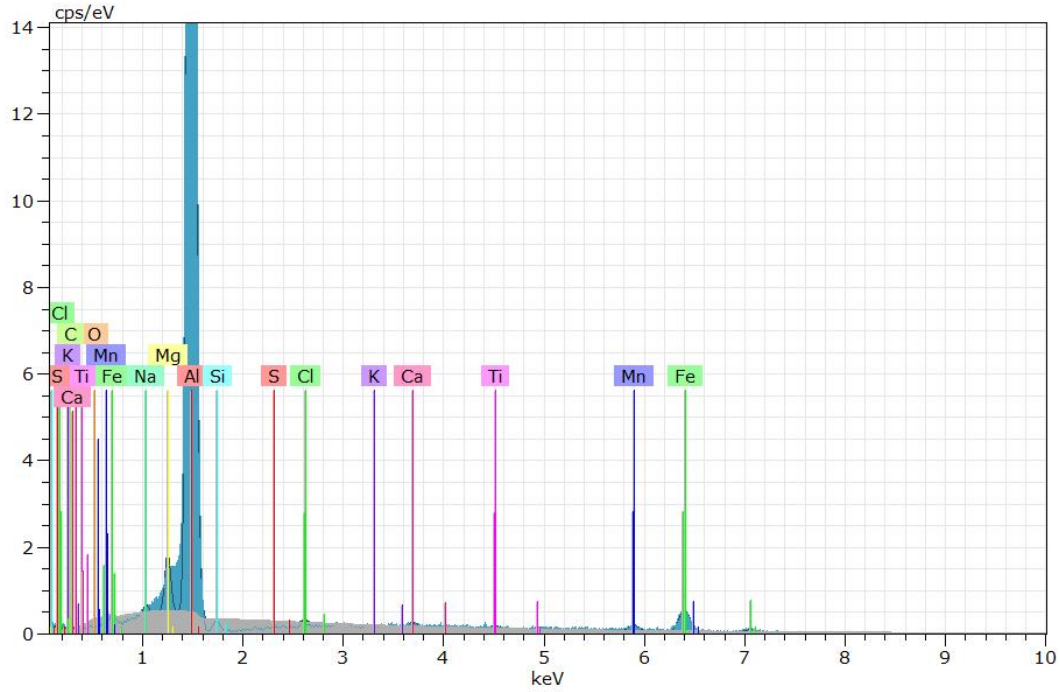

(a) Intensity spectrum of point 63

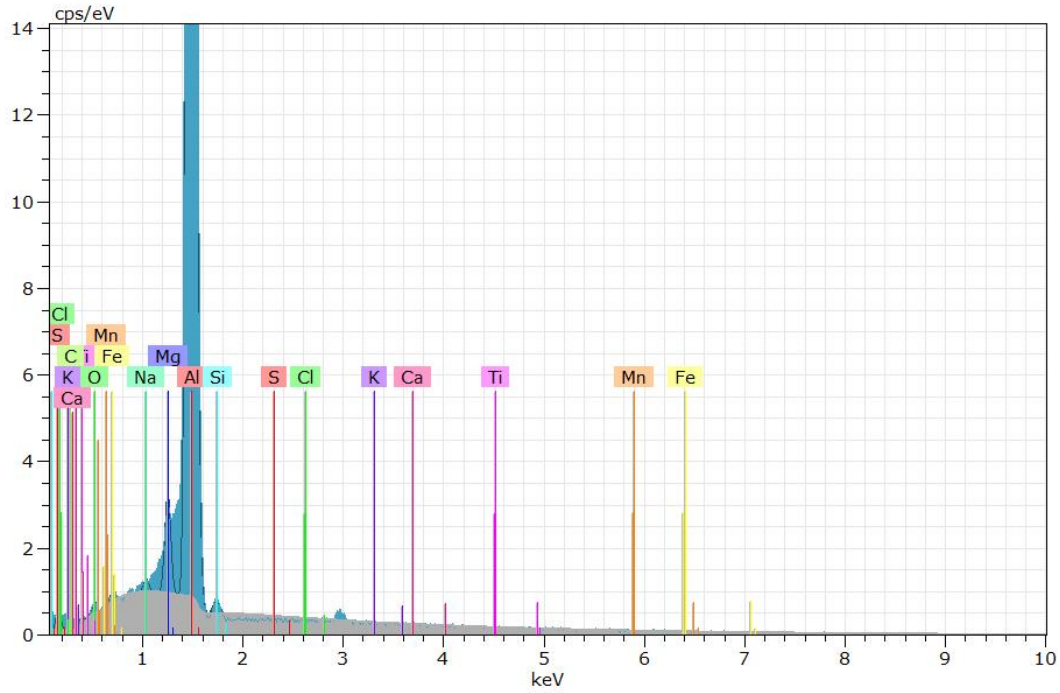

(b) Intensity spectrum of point 64

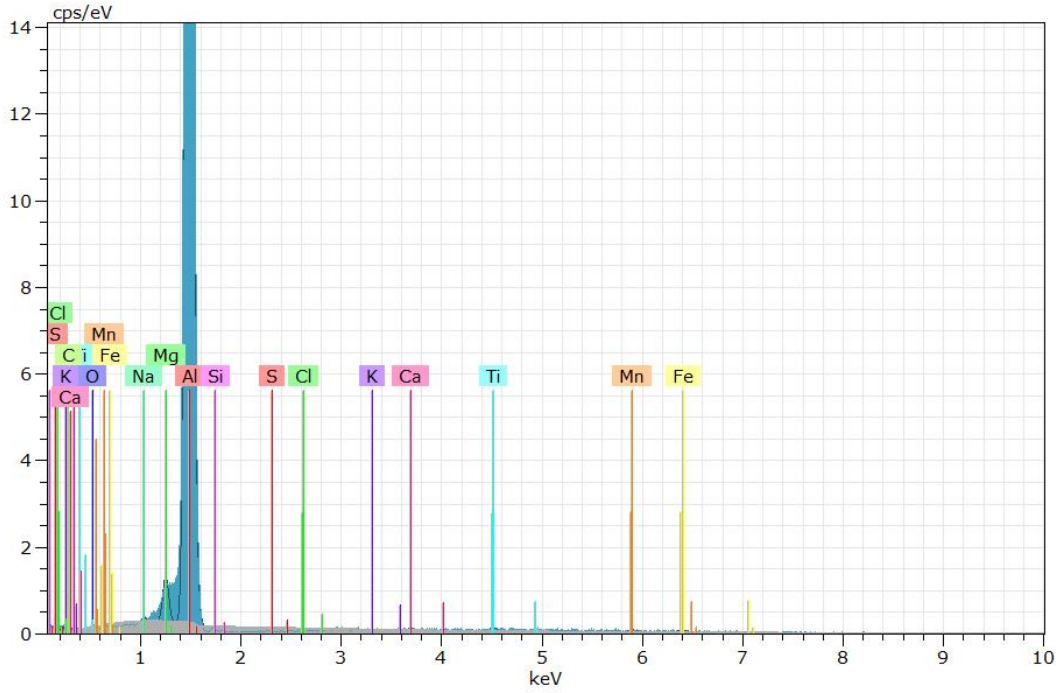

(c) Intensity spectrum of point 65

Figure D.8: Intensity spectrum of the points in figure D.7a

D.5 Air cooled not stretched tensile specimen stored for 7 days storage fracture area 1

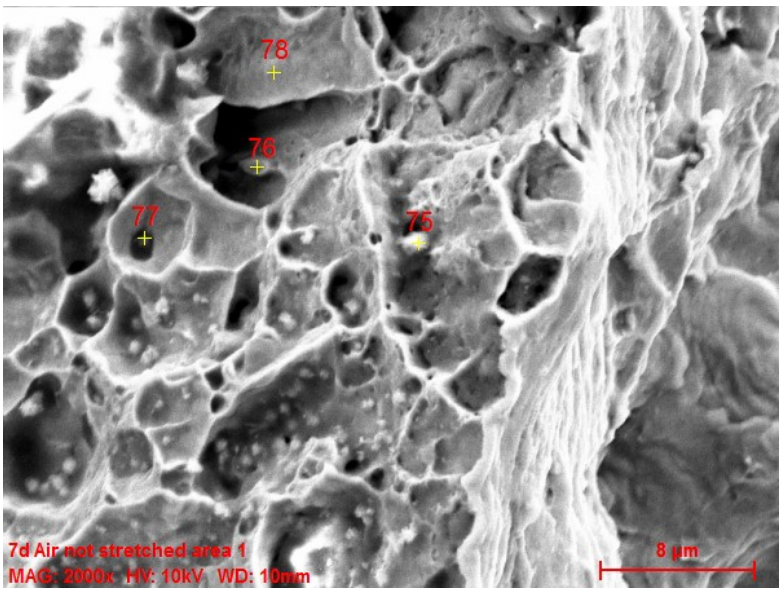

(a) SEM image of fracture area 1 in a not-stretched air cooled tensile specimen stored for 7 days at room temperature.

Element given in $[wt\%]$	Al	O	Mg	Ti	Fe	Mn	Si	K	S	Ca	Na	C	Cl
75	32.41	10.58	0.62	0	0	0	2.84	24.72	0.32	0.60	1.02	12.36	14.54
76	91.93	2.14	1.31	0.04	0.08	0	0.52	1.64	0.49	0.61	0.68	0.40	0.11
77	90.95	0.31	1.37	0.91	2.17	1.96	0	0.70	0.02	0.67	0.36	0.37	0.20
78	91.10	0.14	1.34	1.03	2.99	2.05	0	0.45	0.01	0.54	0.27	0	0.07

Figure D.9: SEM image of fracture area 1 in a not-stretched air cooled specimen stored for 7 days. Chemical analysis as nominative chemical composition of points in the SEM image is given in the table below, obtained by EDS

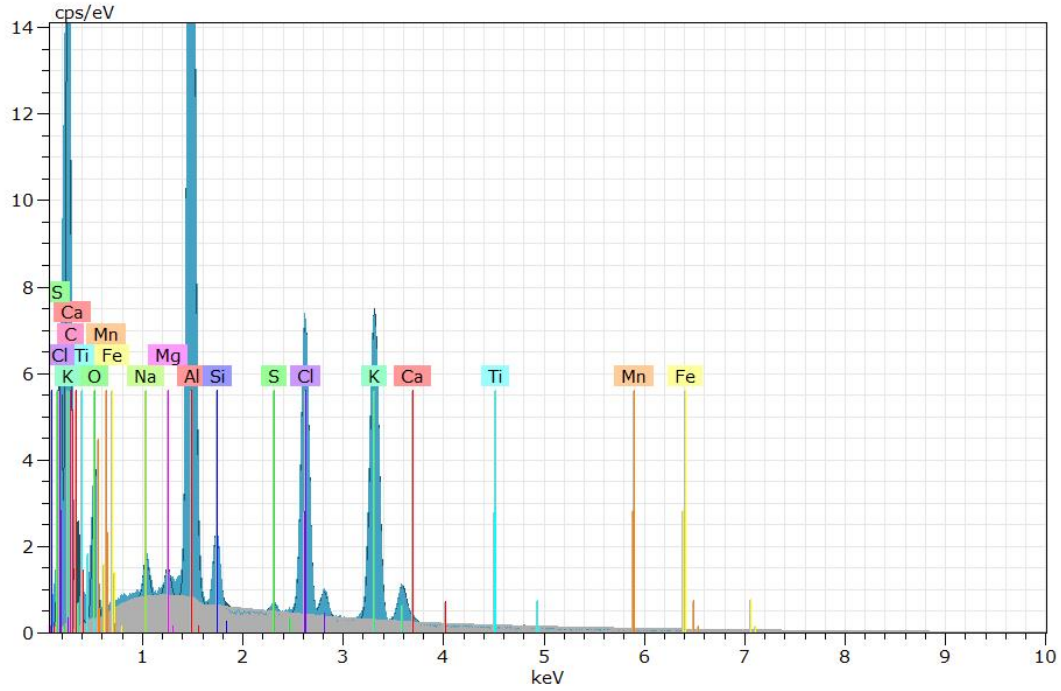

(a) Intensity spectrum of point 77

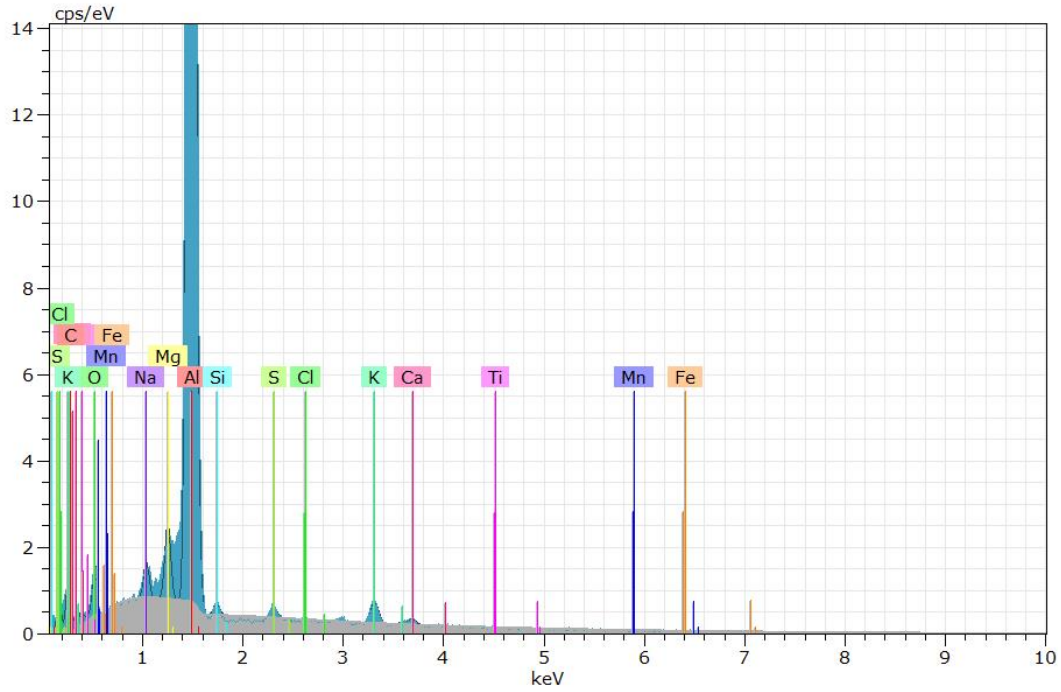

(b) Intensity spectrum of point 76

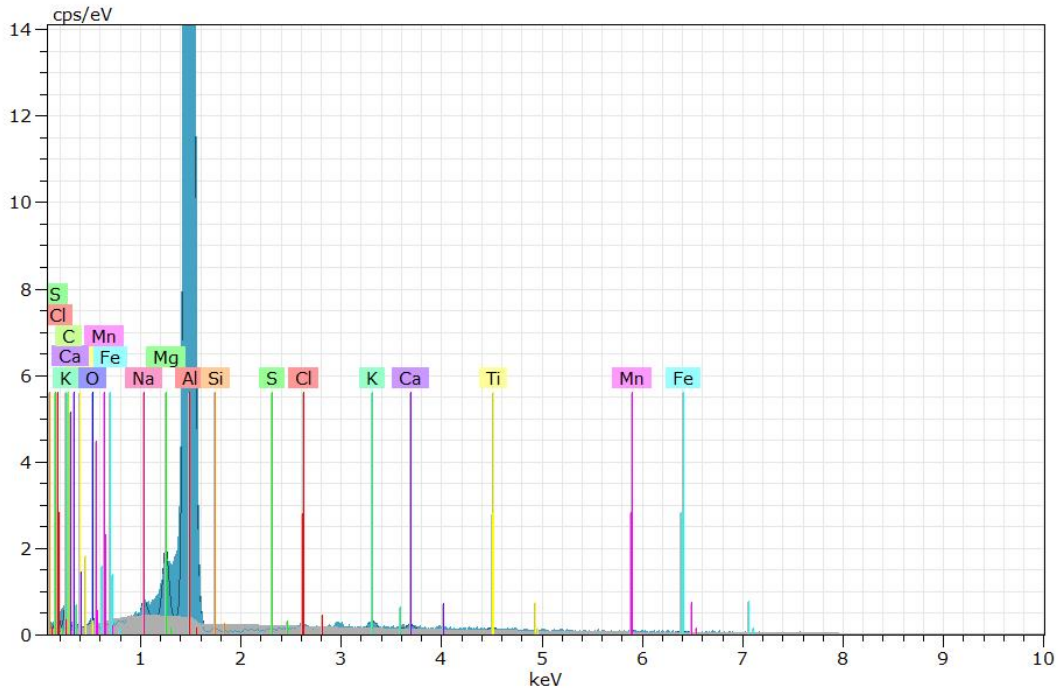

(c) Intensity spectrum of point 77

Figure D.10: Intensity spectrum of the points in figure D.9a

D.6 Air cooled not-stretched tensile specimen stored for 7 days fracture area 2

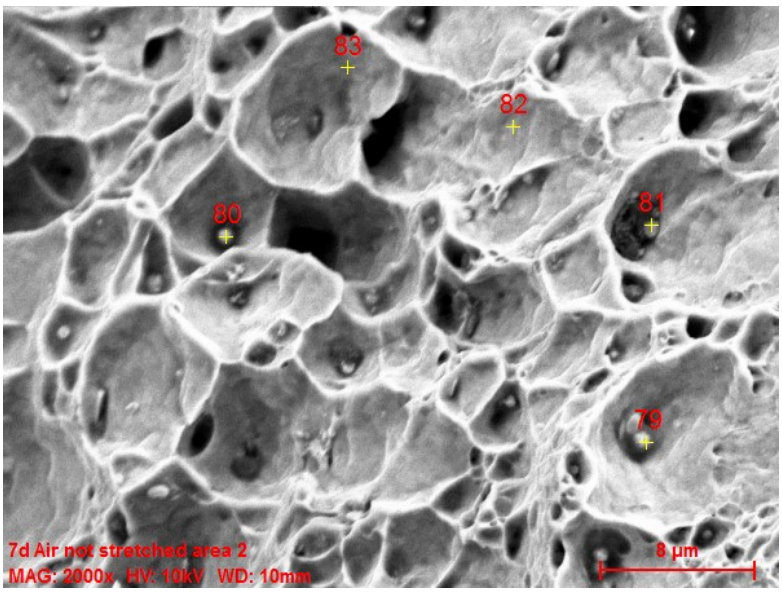

(a) SEM image of fracture area 2 in a not-stretched air cooled tensile specimens stored for 7days at room temperature.

Element given in $[wt\%]$	Al	O	Mg	Ti	Fe	Mn	Si	K	S	Ca	Na	C	Cl
79	38.50	12.45	1.01	0	0.01	0.11	0.62	20.37	0.51	0.84	2.95	6.53	16.10
80	61.38	6.94	1.32	0	0.02	0.41	0	11.17	0.83	3.08	2.16	3.85	8.83
81	62.67	11.68	1.23	0	0.62	0.22	0.57	1.22	0.15	16.34	0.66	3.89	0.74
82	97.64	0.40	1.37	0	0	0	0.30	0	0.01	0.03	0.22	0	0.02
83	94.09	0.06	1.40	0.65	1.56	1.33	0	0.23	0.01	0.31	0.29	0	0.08

Figure D.11: SEM image of fracture area 2 in a not-stretched air cooled tensile specimens stored for 7 days at room temperature. Chemical analysis as nominative chemical composition of points in the SEM image is given in the table below, obtained by EDS.

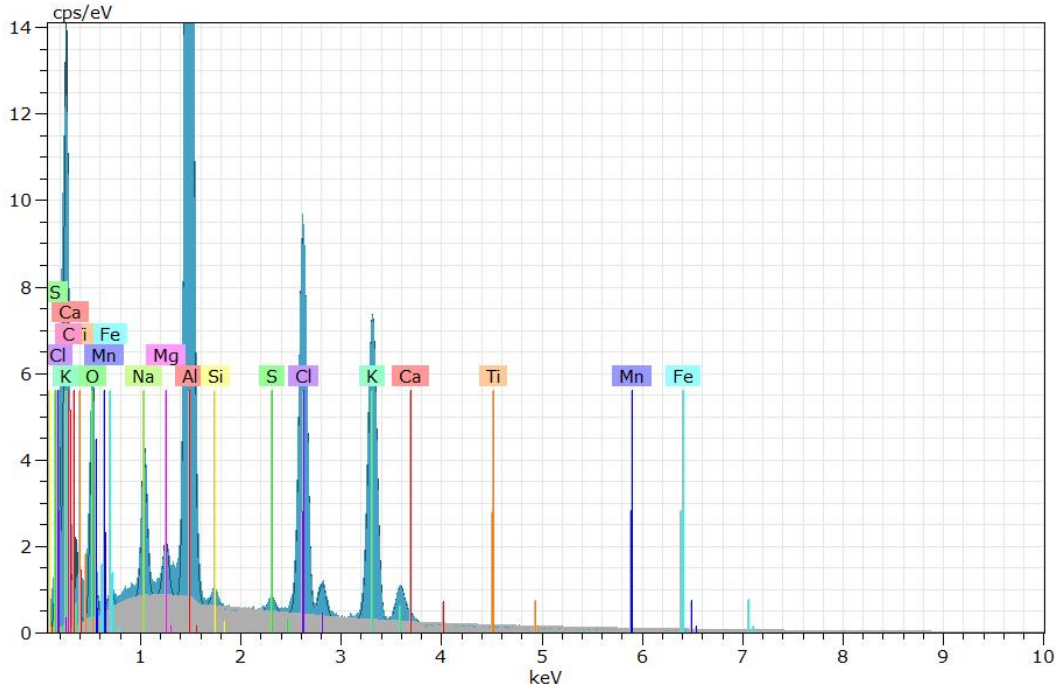

(a) Intensity spectrum of point 79

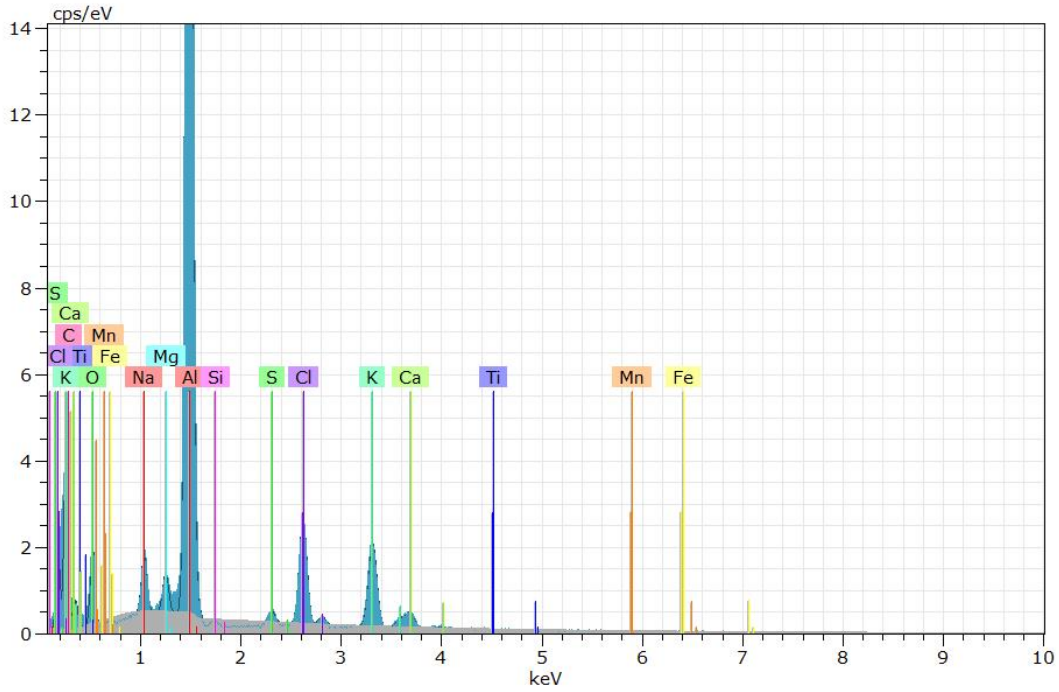

(b) Intensity spectrum of point 80

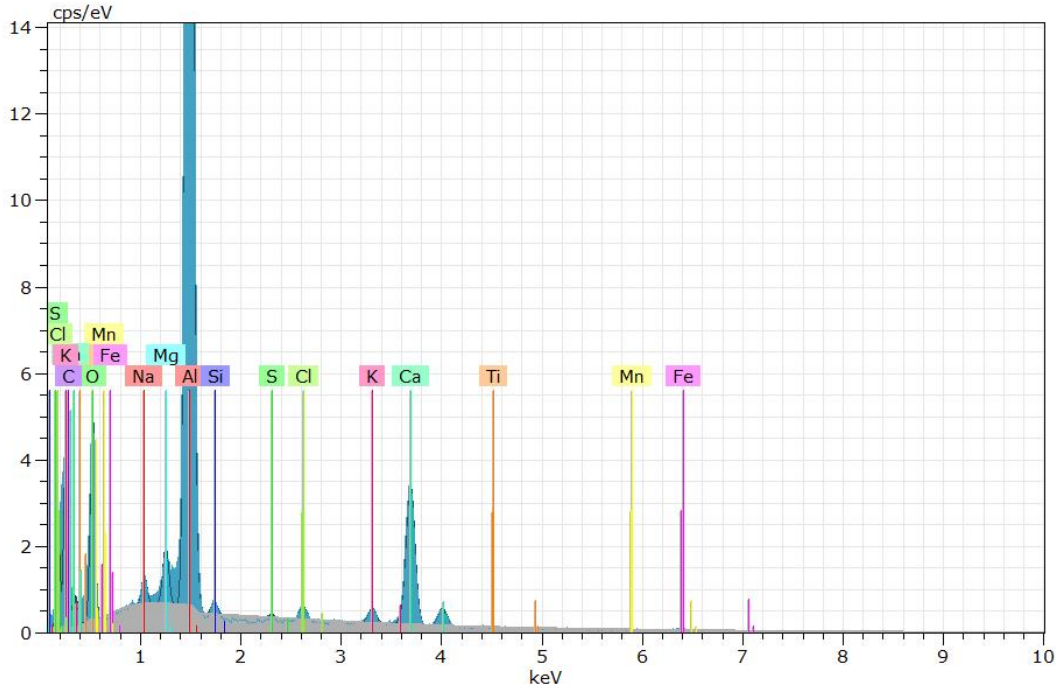

(c) Intensity spectrum of point 81

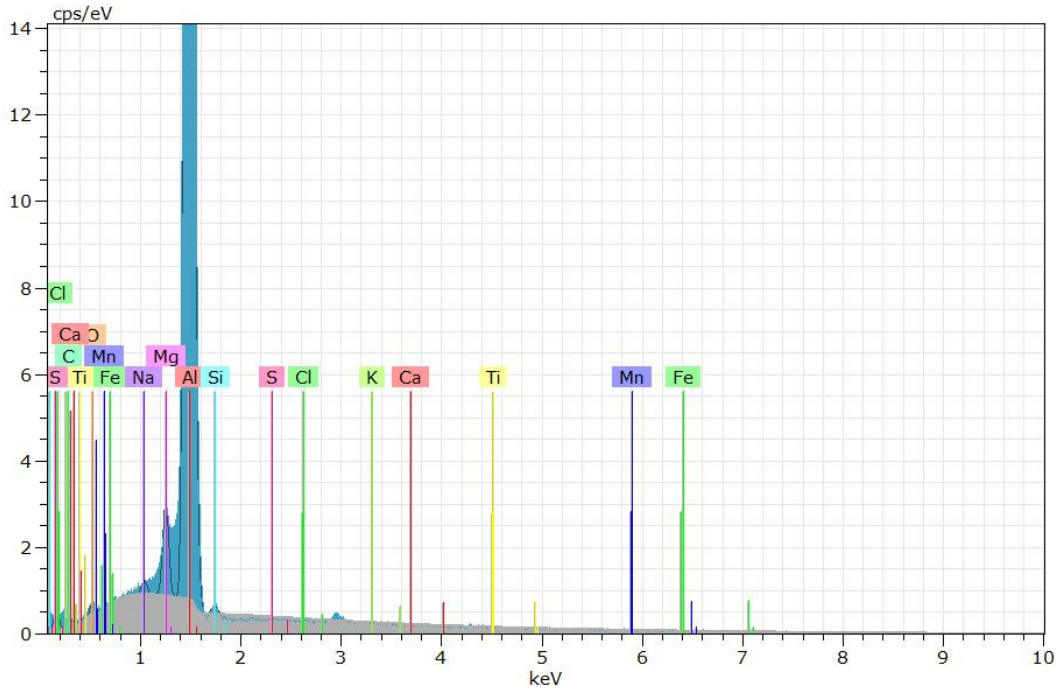

(d) Intensity spectrum of point 82

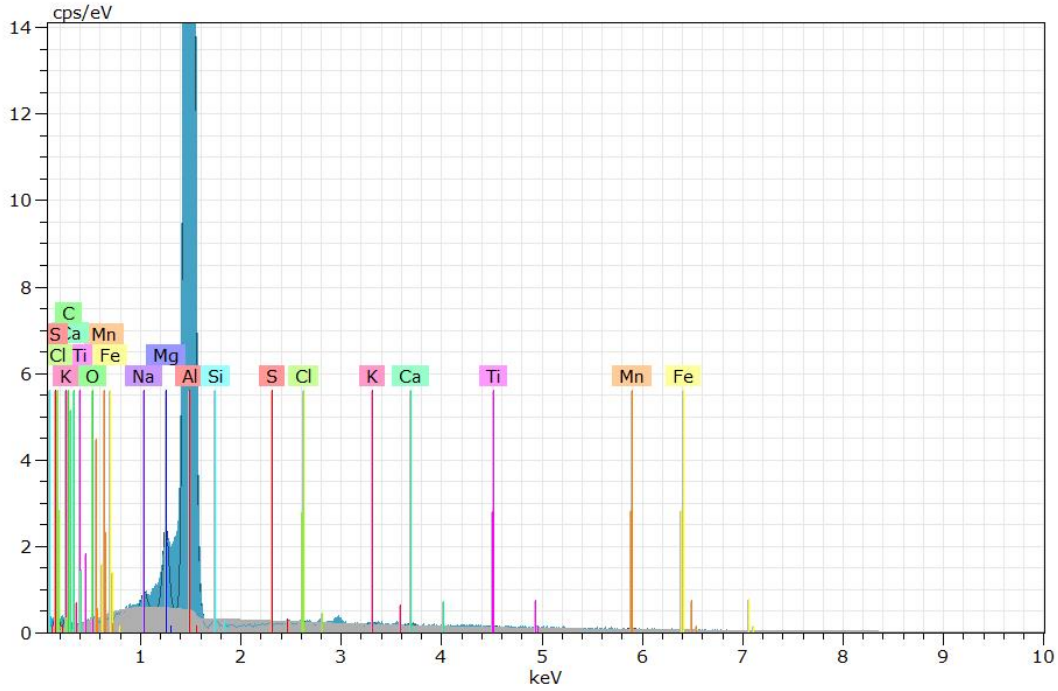

(e) Intensity spectrum of point 83

Figure D.12: Intensity spectrum of the points in figure D.11a

D.7 Air cooled pre stretched tensile specimen stored for 7 days fracture area 1

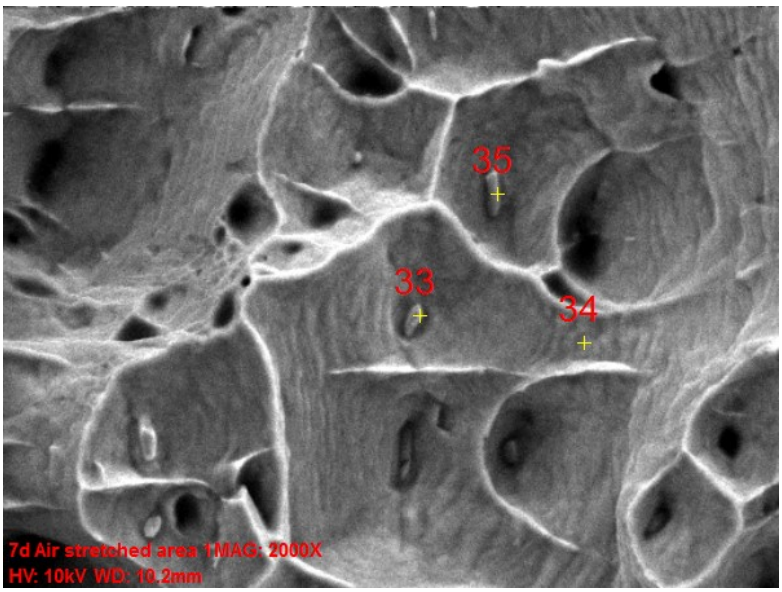

(a) SEM image of fracture area 1 in a pre stretched air cooled tensile specimens stored for 7days at room temperature.

Element given in $[wt\%]$	Al	O	Mg	Ti	Fe	Mn	Si	K	S	Ca	Na	C	Cl
33	73.68	0.84	1.01	0	17.41	2.43	4.22	0.06	0.02	0	0.31	0	0.02
34	97.17	0.46	1.36	0	0.04	0	0.70	0	0.04	0.02	0.22	0	0
35	61.23	0.63	0.76	0	29.88	2.71	4.55	0.01	0.03	0	0.15	0	0.06

Figure D.13: SEM image of fracture area 1 in a pre stretched air cooled tensile specimens stored for 7 days at room temperature. Chemical analysis as nominative chemical composition of points in the SEM image is given in the table below, obtained by EDS.

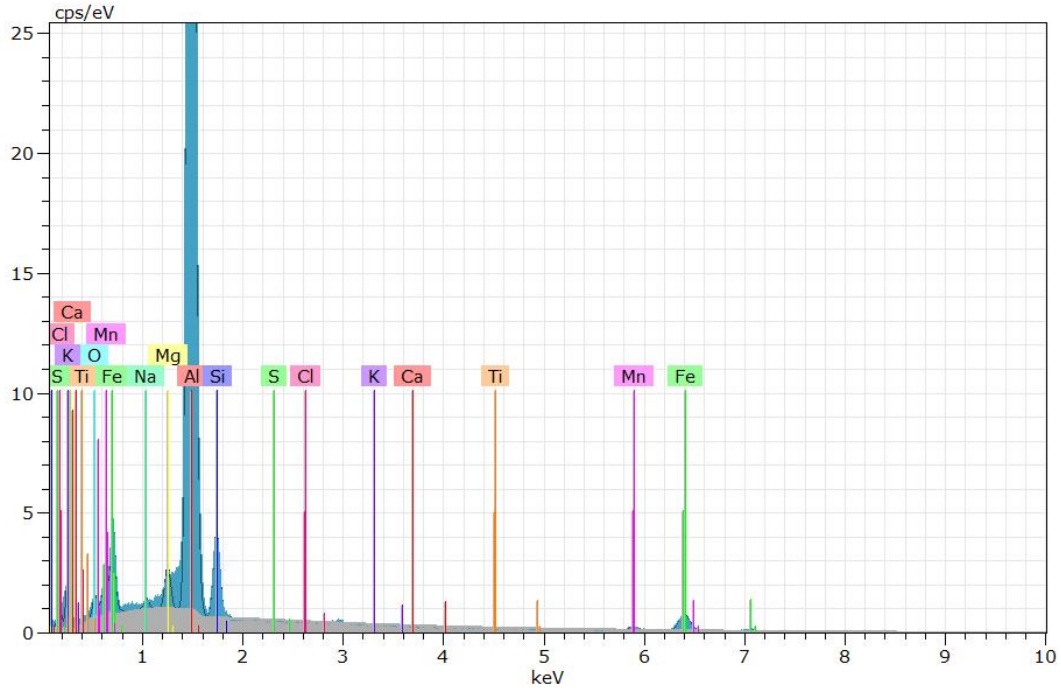

(a) Intensity spectrum of point 33

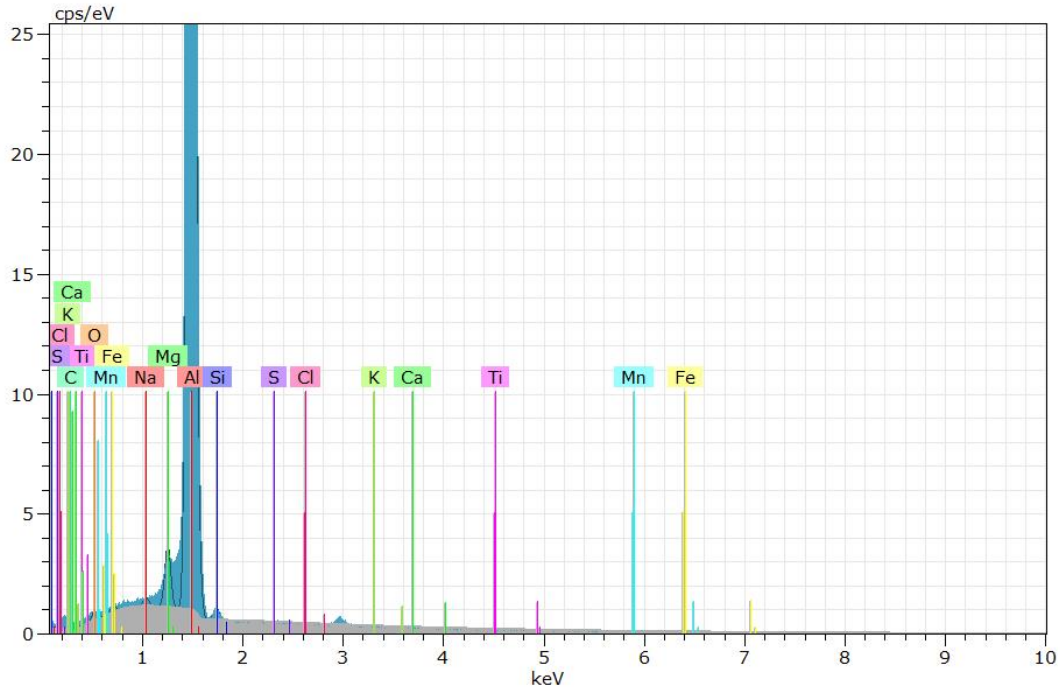

(b) Intensity spectrum of point 34

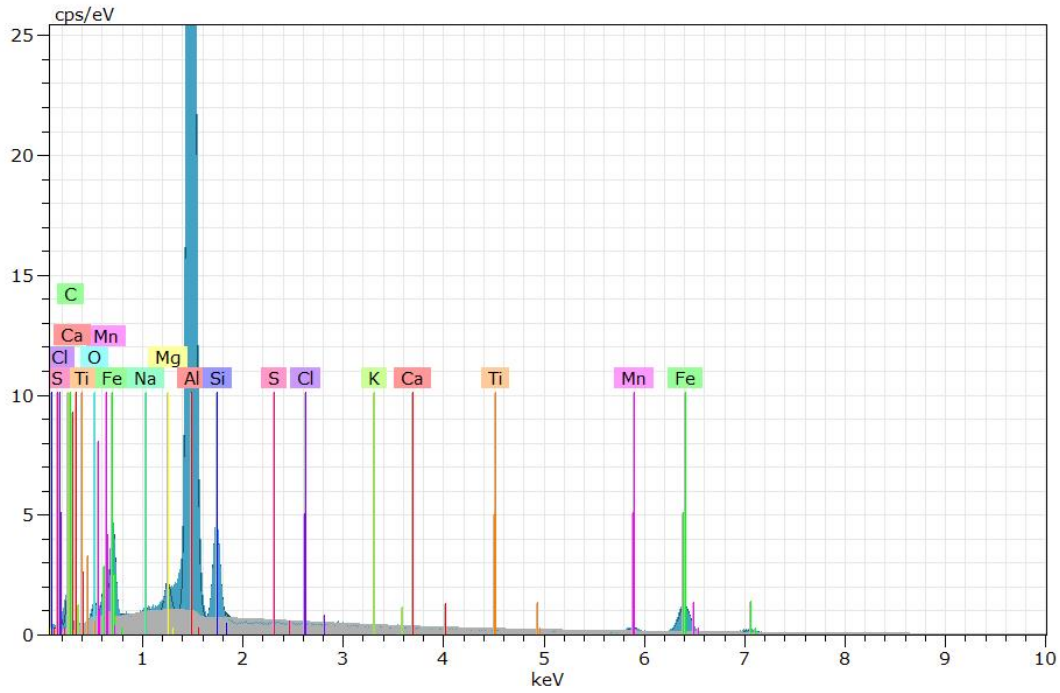

(c) Intensity spectrum of point 35

Figure D.14: Intensity spectrum of the points in figure D.13a

D.8 Air cooled pre stretched tensile specimen stored for 7 days fracture area 2

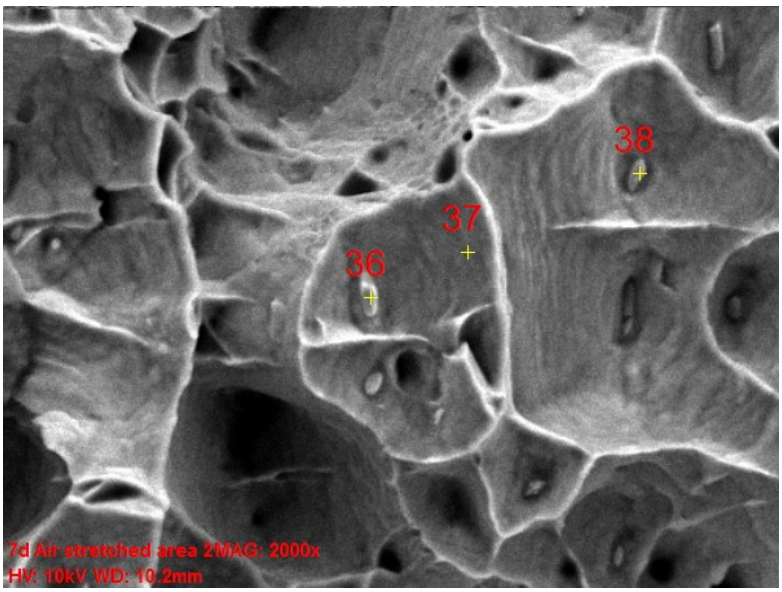

(a) SEM image of fracture area 2 in a pre stretched air cooled tensile specimens stored for 7days at room temperature.

Element given in $[wt\%]$	Al	O	Mg	Ti	Fe	Mn	Si	K	S	Ca	Na	C	Cl
36	56.17	0.55	0.71	0.08	33.50	1.84	6.94	0	0.05	0.04	0.12	0	0
37	97.73	0.26	1.37	0.07	0	0.10	0.26	0	0.01	0	0.20	0	0
38	96.92	0.30	1.25	0.04	0.13	0.21	0.73	0	0	0.04	0.18	0.19	0

Figure D.15: SEM image of fracture area 2 in a pre stretched air cooled tensile specimens stored for 7 days at room temperature. Chemical analysis as nominative chemical composition of points in the SEM image is given in the table below, obtained by EDS.

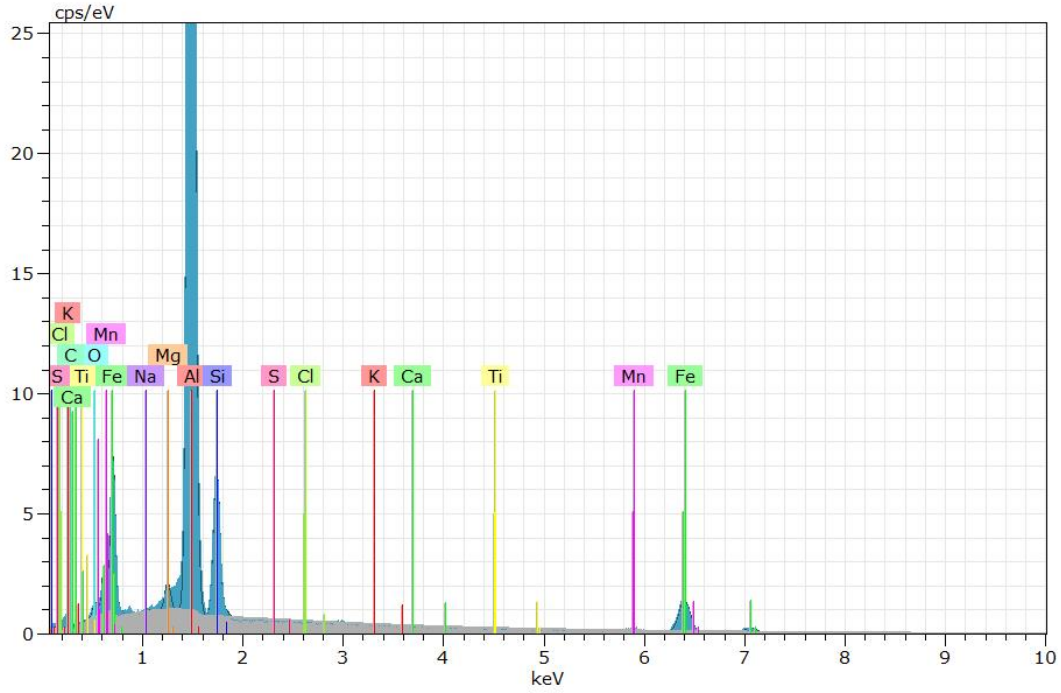

(a) Intensity spectrum of point 36

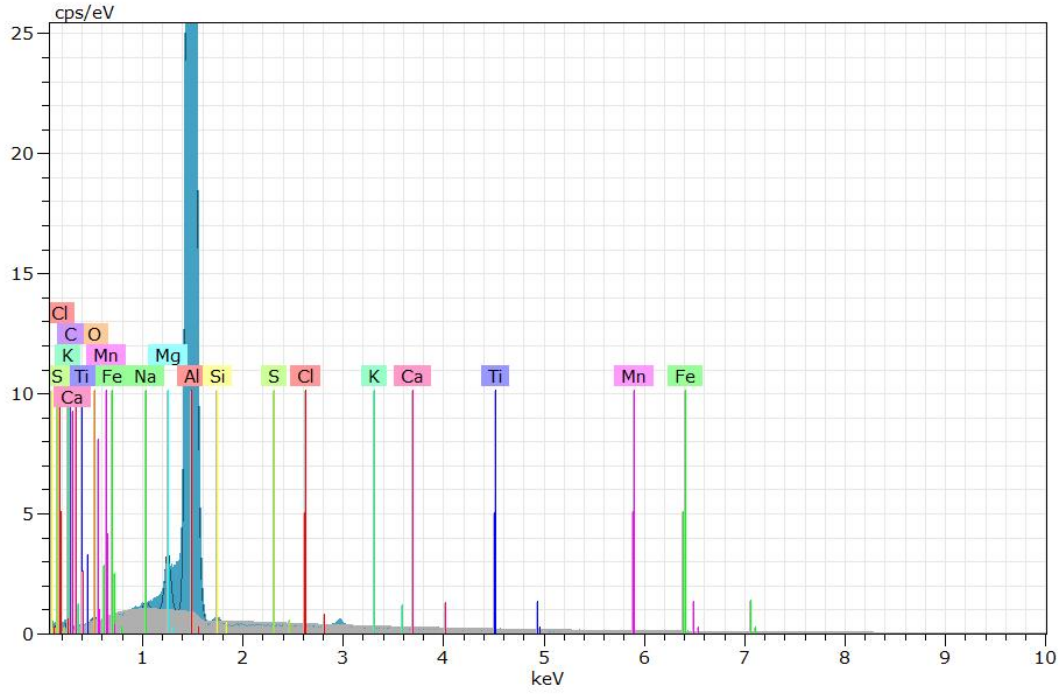

(b) Intensity spectrum of point 37

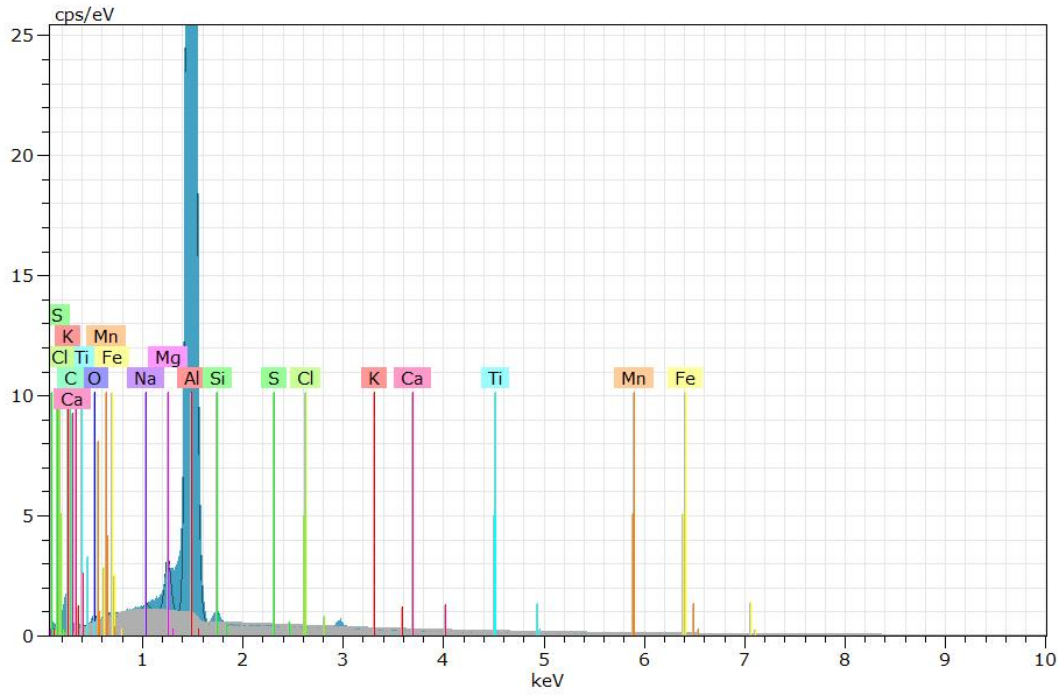

(c) Intensity spectrum of point 38

Figure D.16: Intensity spectrum of the points in figure D.15a

D.9 Water cooled not-stretched tensile specimen stored for 24hours fracture area 1

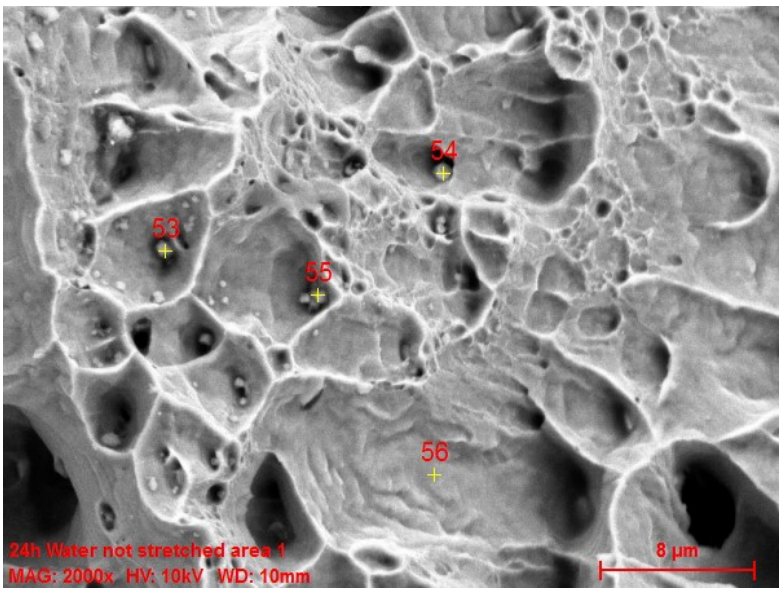

(a) SEM image of fracture area 1 in a not-stretched water cooled tensile specimen stored for 24 hours at room temperature.

Element given in $[wt\%]$	Al	O	Mg	Ti	Fe	Mn	Si	K	S	Ca	Na	C	Cl
53	86.31	0.09	1.43	1.35	3.21	3.07	0	1.81	0.08	1.08	0.46	0	1.12
54	75.93	5.10	1.36	0.01	0	0	0.92	1.91	0.22	0.97	1.07	9.07	3.46
55	71.59	0.10	1.46	1.25	3.15	2.69	0	11.66	0.03	1.57	0.61	0.11	5.77
56	96.79	0.79	1.37	0	0.03	0.15	0.56	0.01	0.05	0	0.25	0	0.01

Figure D.17: SEM image of fracture area 1 in a not-stretched water cooled tensile specimen stored for 24 hours at room temperature. Chemical analysis as as nominative chemical composition of points in the SEM image is given in the table below, obtained by EDS.

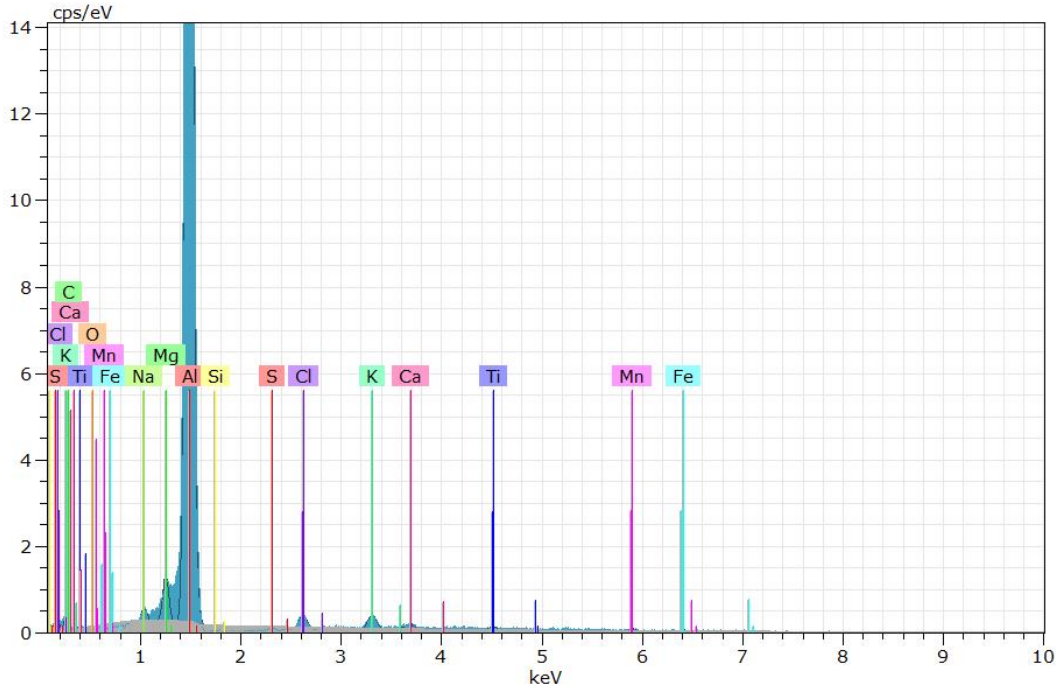

(a) Intensity spectrum of point 53

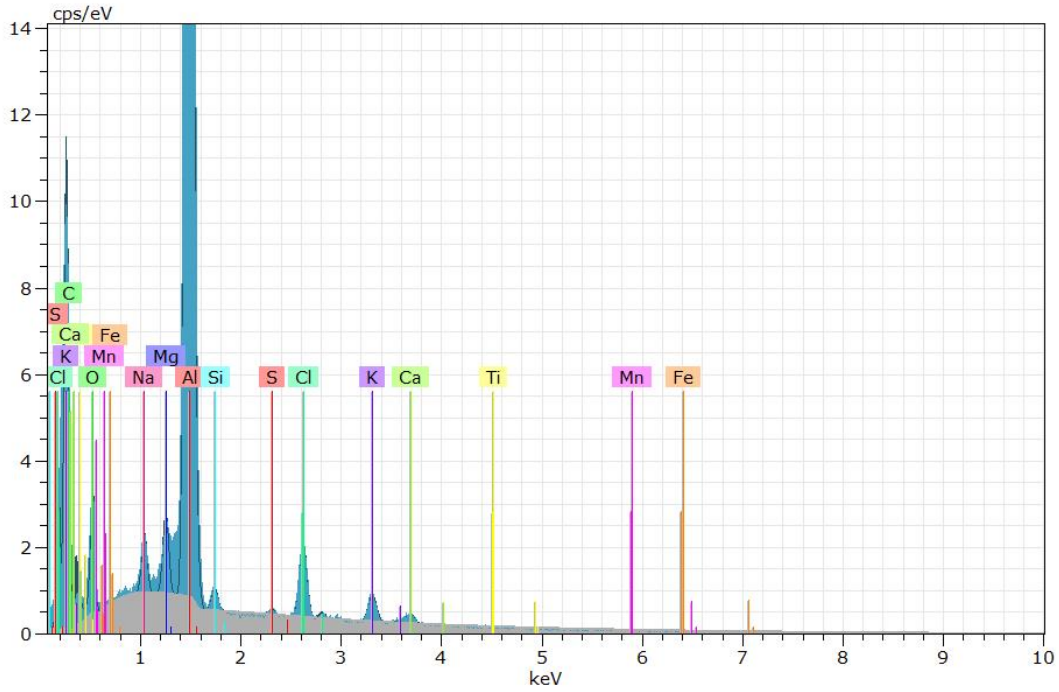

(b) Intensity spectrum of point 54

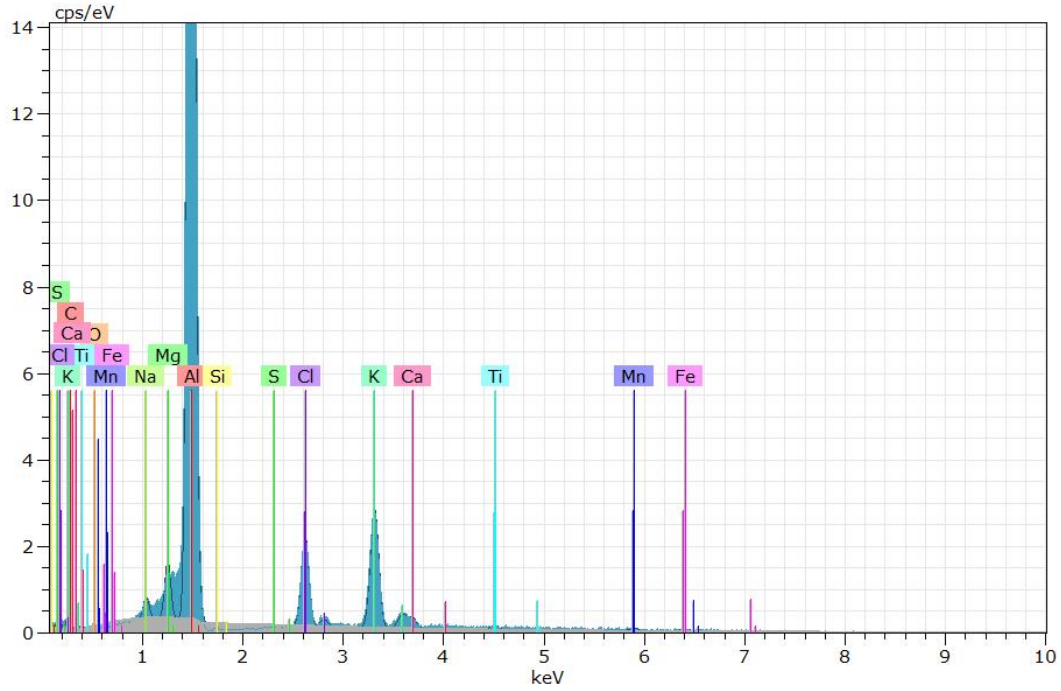

(c) Intensity spectrum of point 55

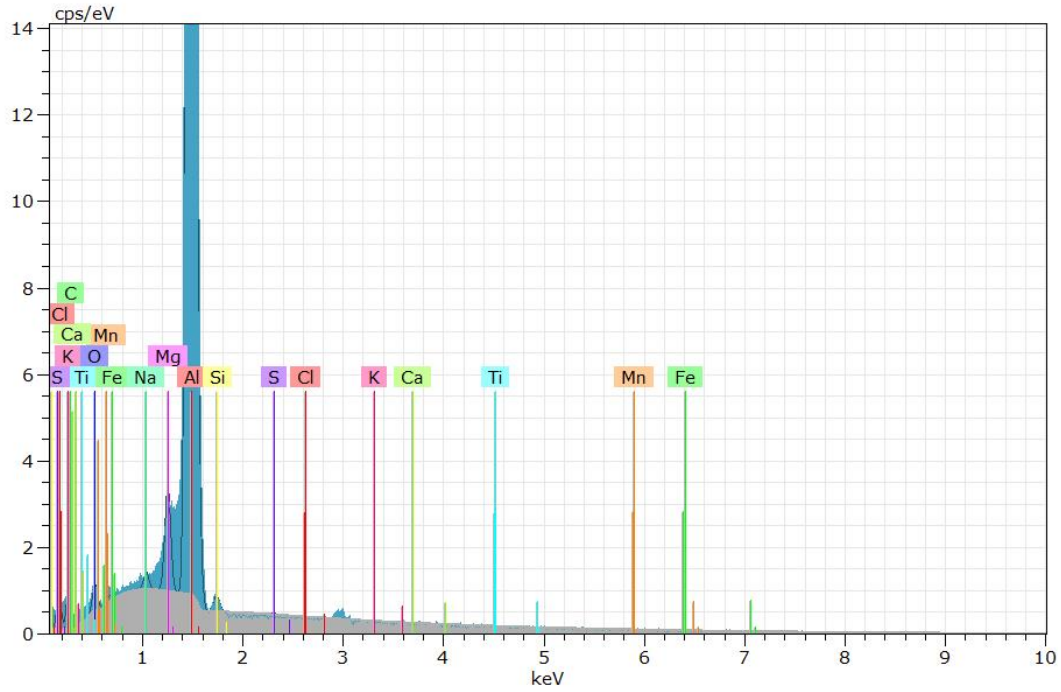

(d) Intensity spectrum of point 56

Figure D.18: Intensity spectrum of the points in figure D.17a

D.10 Water cooled not-stretched tensile specimen stored for 24hours fracture area 2

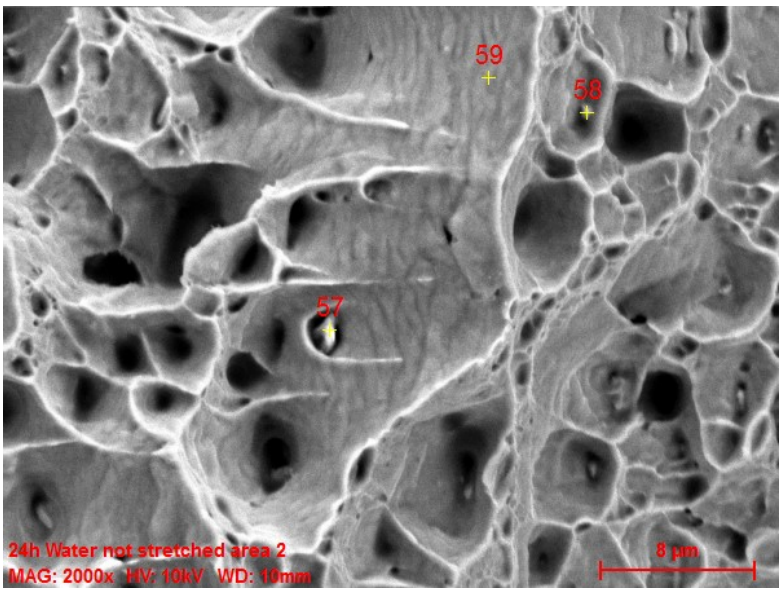

(a) SEM image of fracture area 2 in a not-stretched water cooled tensile specimen stored for 24 hours at room temperature.

Element given in $[wt\%]$	Al	O	Mg	Ti	Fe	Mn	Si	K	S	Ca	Na	C	Cl
57	83.62	0.84	1.33	1.37	4.02	2.52	0	0.42	0.01	5.61	0.24	0.02	0.01
58	73.86	0.84	0.97	0.04	17.73	0.76	5.39	0	0.05	0	0.26	0.10	0
59	96.94	0.64	1.36	0	0	0.04	0.72	0.03	0	0.01	0.26	0	0

Figure D.19: SEM image of fracture area 2 in a not-stretched water cooled tensile specimen stored for 24 hours at room temperature. Chemical analysis as as nominative chemical composition of points in the SEM image is given in the table below, obtained by EDS.

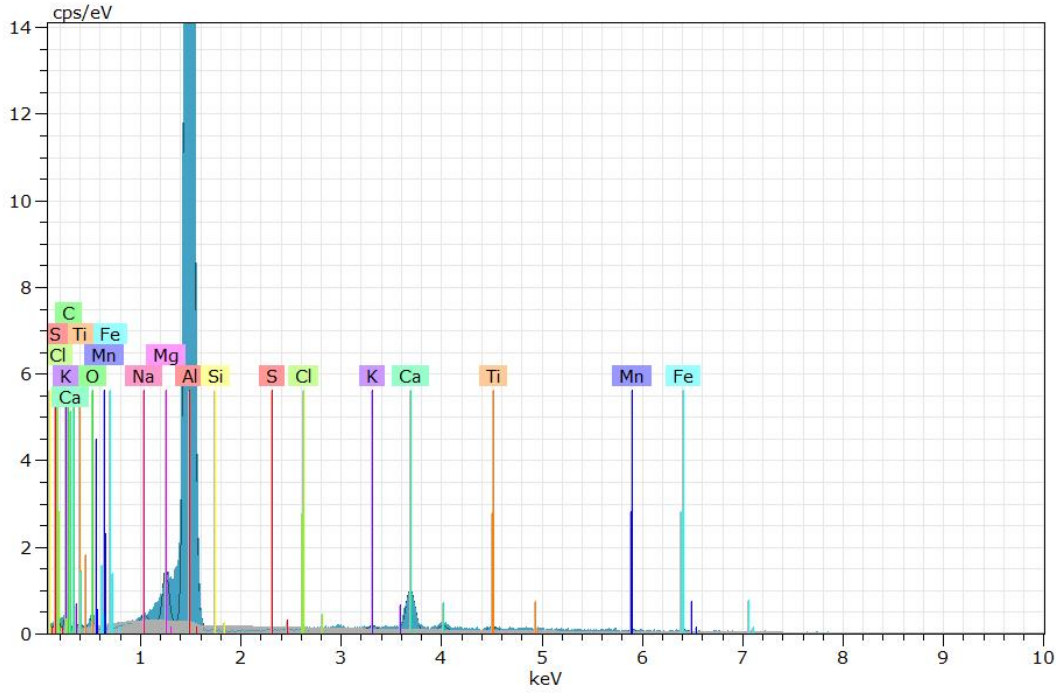

(a) Intensity spectrum of point 57

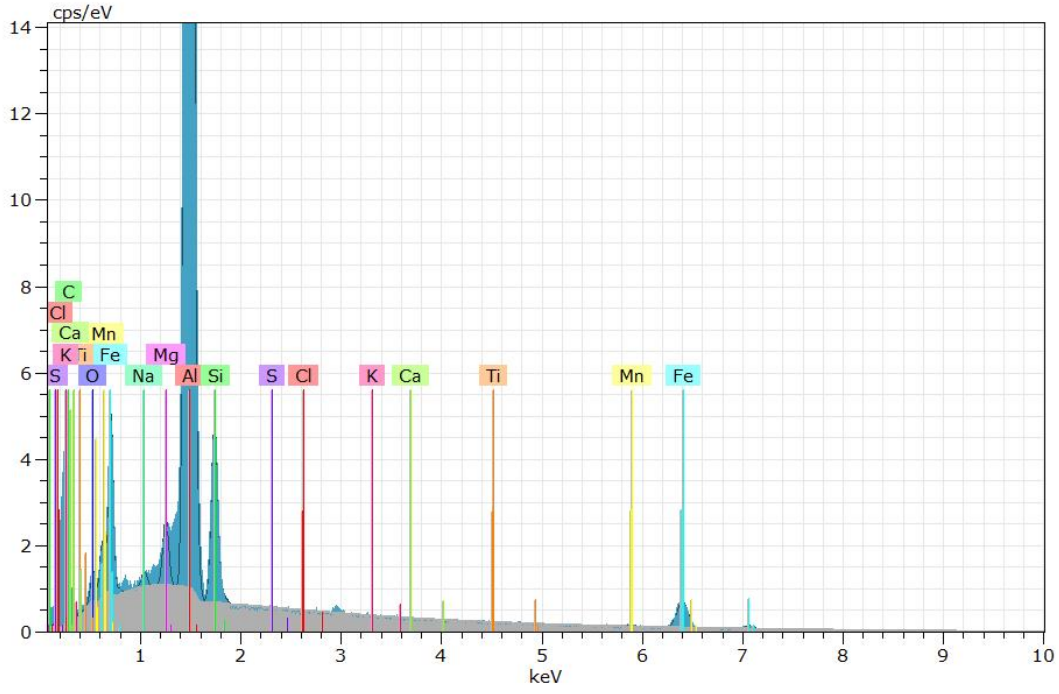

(b) Intensity spectrum of point 58

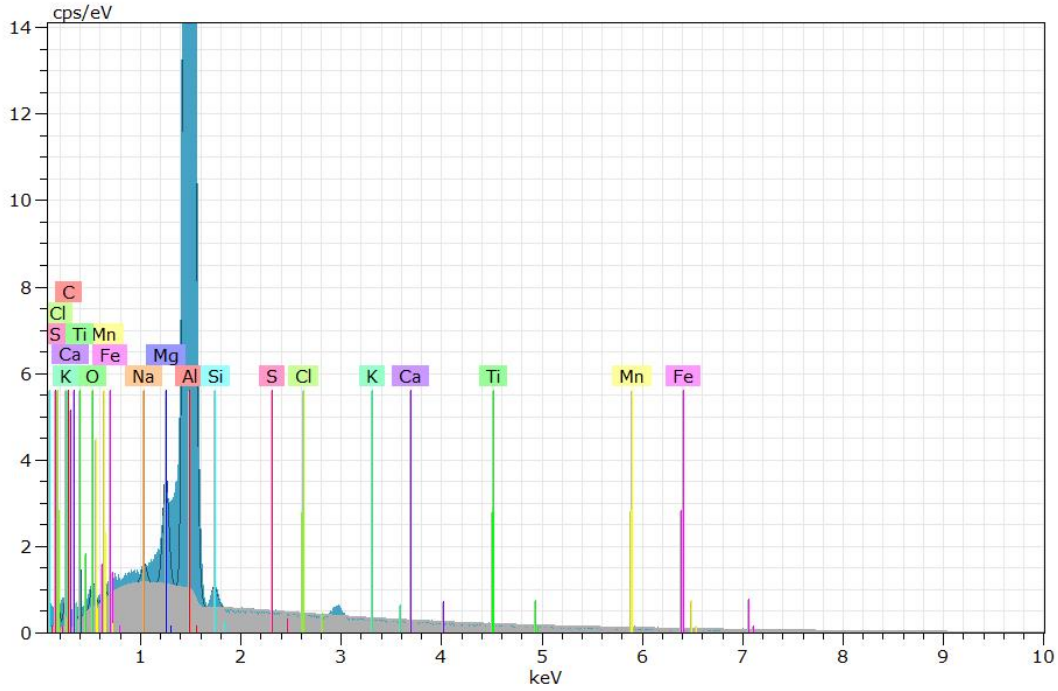

(c) Intensity spectrum of point 59

Figure D.20: Intensity spectrum of the points in figure D.19a

D.11 Water cooled pre stretched tensile specimen stored for 24hours fracture area 1

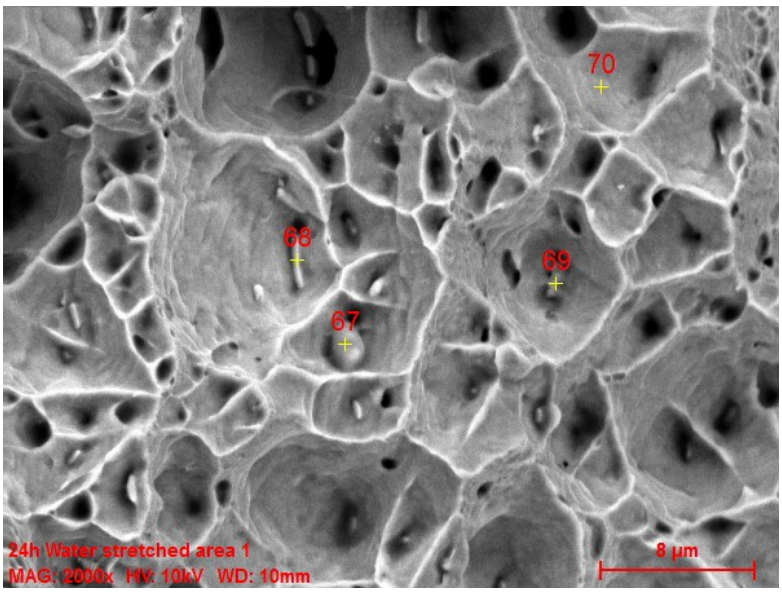

(a) SEM image of fracture area 1 in a pre stretched water cooled tensile specimens stored for 24 hours at room temperature.

Element given in $[wt\%]$	Al	O	Mg	Ti	Fe	Mn	Si	K	S	Ca	Na	C	Cl
67	45.00	17.45	1.02	0	0.50	0	1.16	2.55	0.55	0.23	1.42	26.27	3.86
68	97.24	0.24	1.31	0.01	0.42	0	0.50	0	0.04	0	0.23	0	0
69	95.40	1.86	1.50	0.05	0.01	0	0.28	0.13	0.12	0.23	0.31	0	0.10
70	96.69	0.64	1.43	0.01	0.07	0.11	0.65	0	0.07	0	0.31	0	0.02

Figure D.21: SEM image of fracture area 1 in a pre stretched water cooled tensile specimens stored for 24 hours at room temperature. Chemical analysis as nominative chemical composition of points in the SEM image is given in the table below, obtained by EDS.

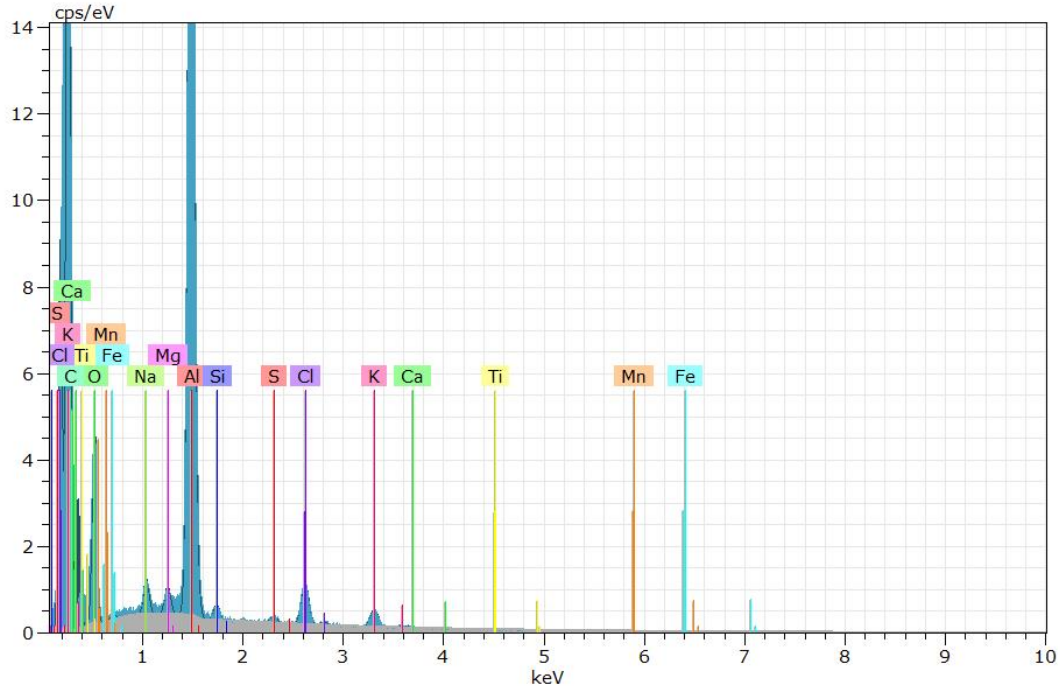

(a) Intensity spectrum of point 67

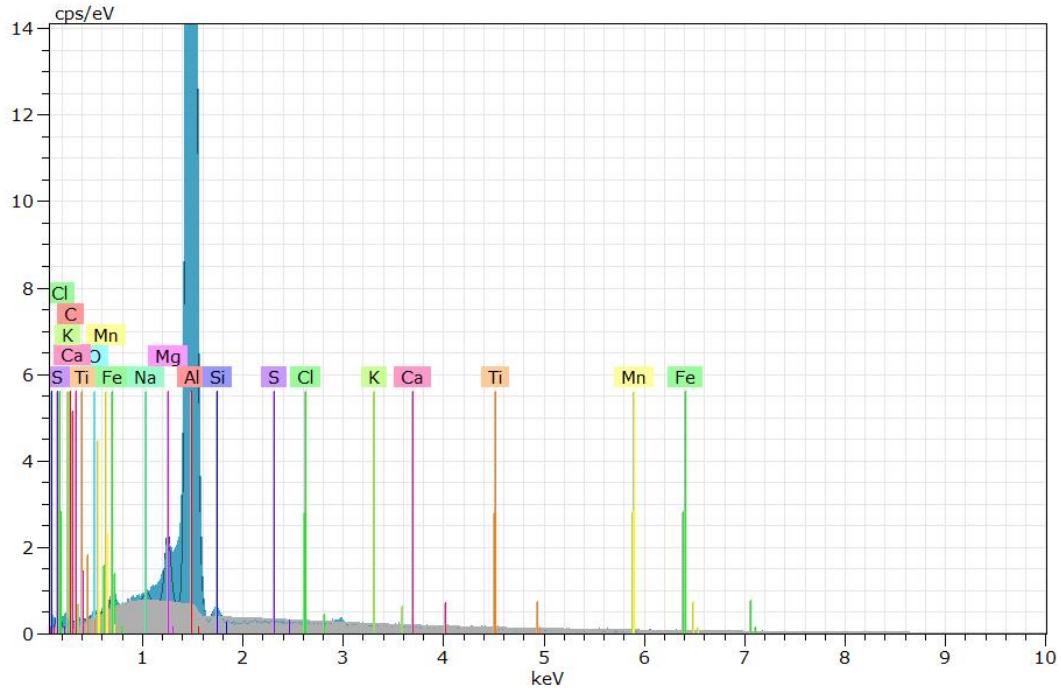

(b) Intensity spectrum of point 68

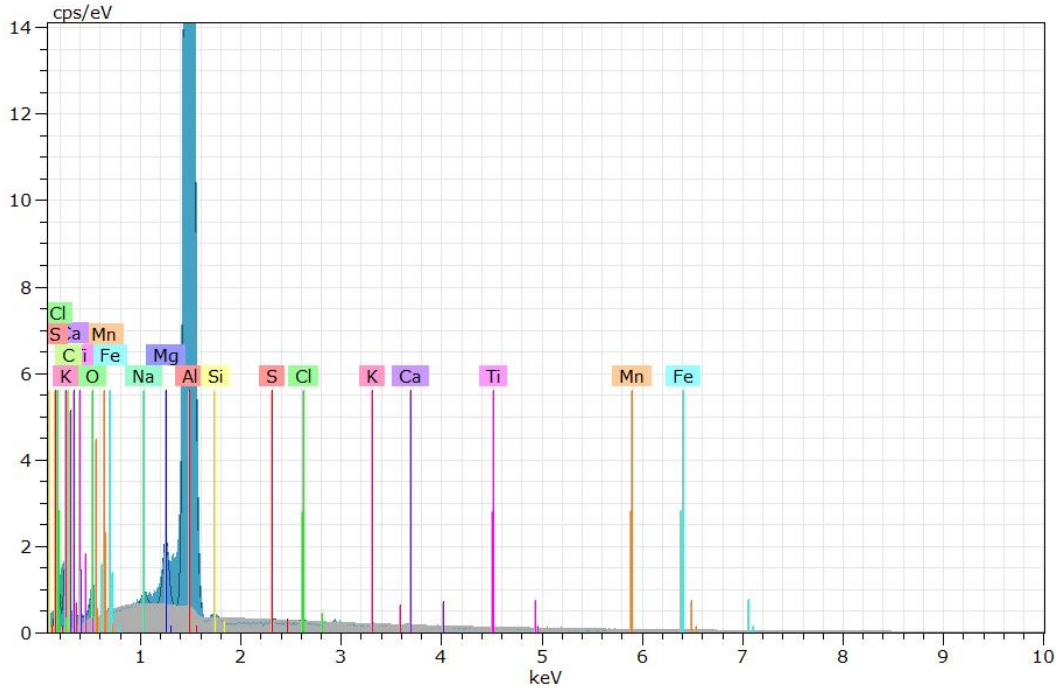

(c) Intensity spectrum of point 69

Figure D.22: Intensity spectrum of the points in figure D.21a

D.12 Water cooled pre stretched tensile specimen stored for 24hours fracture area 2

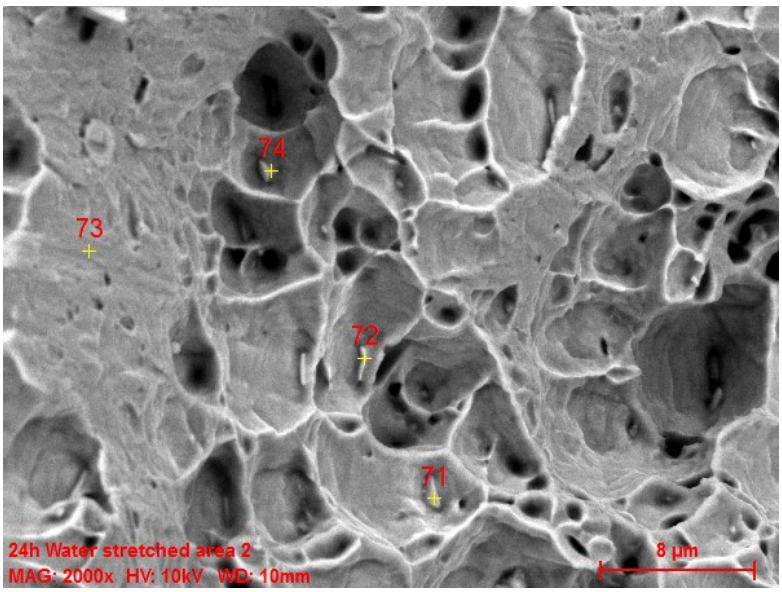

(a) SEM image of fracture area 2 in a pre stretched water cooled tensile specimen sample stored for 24 hours at room temperature.

Element given in $[wt\%]$	Al	O	Mg	Ti	Fe	Mn	Si	K	S	Ca	Na	C	Cl
71	65.96	0.93	0.98	0	22.40	3.02	6.23	0	0	0.07	0.41	0	0
72	83.78	0.47	1.30	0.05	9.36	1.88	2.84	0.03	0	0	0.23	0	0.05
73	95.93	1.23	1.62	0.05	0.27	0	0.52	0.04	0.03	0.02	0.28	0	0
74	61.16	0	0.40	0	27.89	10.29	0	0.04	0	0.18	0	0	0.04

Figure D.23: SEM image of fracture area 2 in a pre stretched water cooled tensile specimen stored for 24 hours at room temperature. Chemical analysis as nominative chemical composition of points in the SEM image is given in the table below, obtained by EDS.

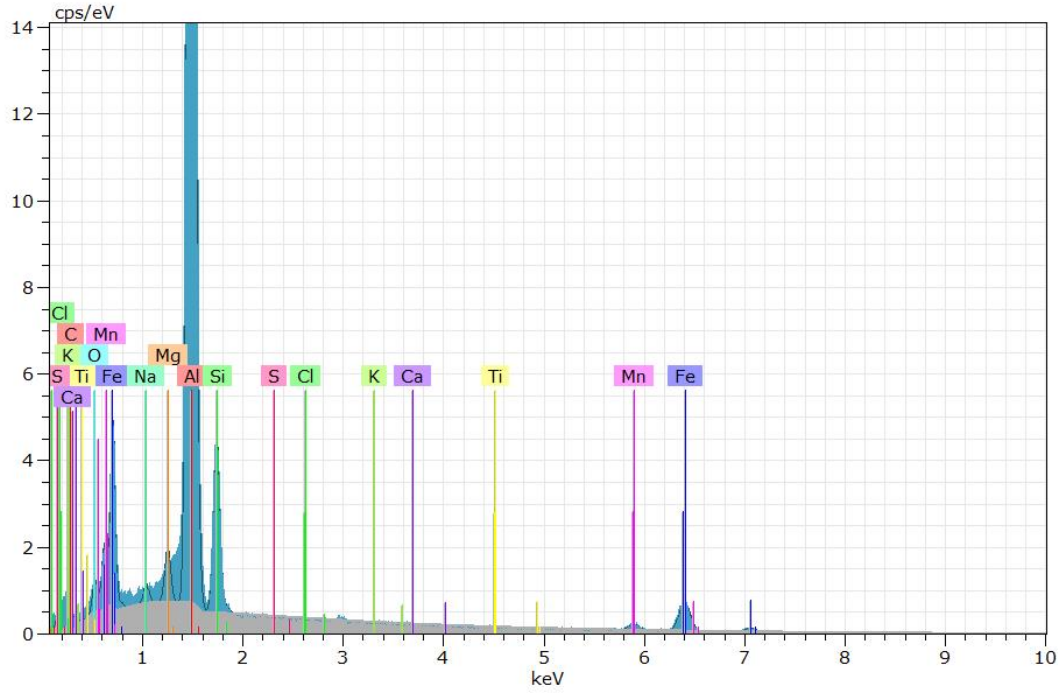

(a) Intensity spectrum of point 71

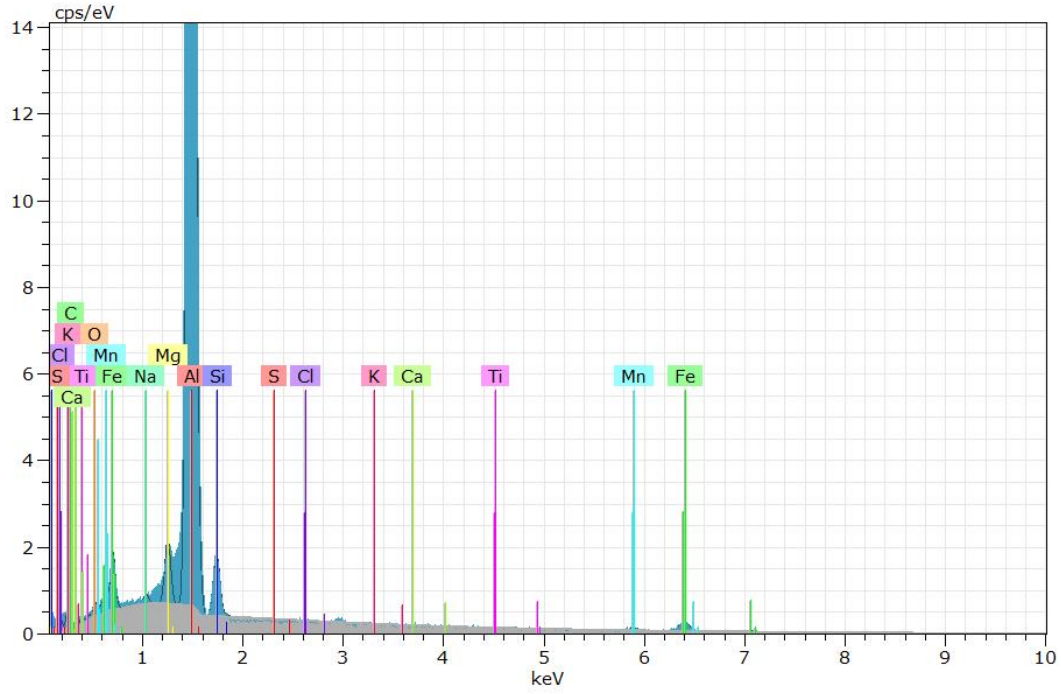

(b) Intensity spectrum of point 72

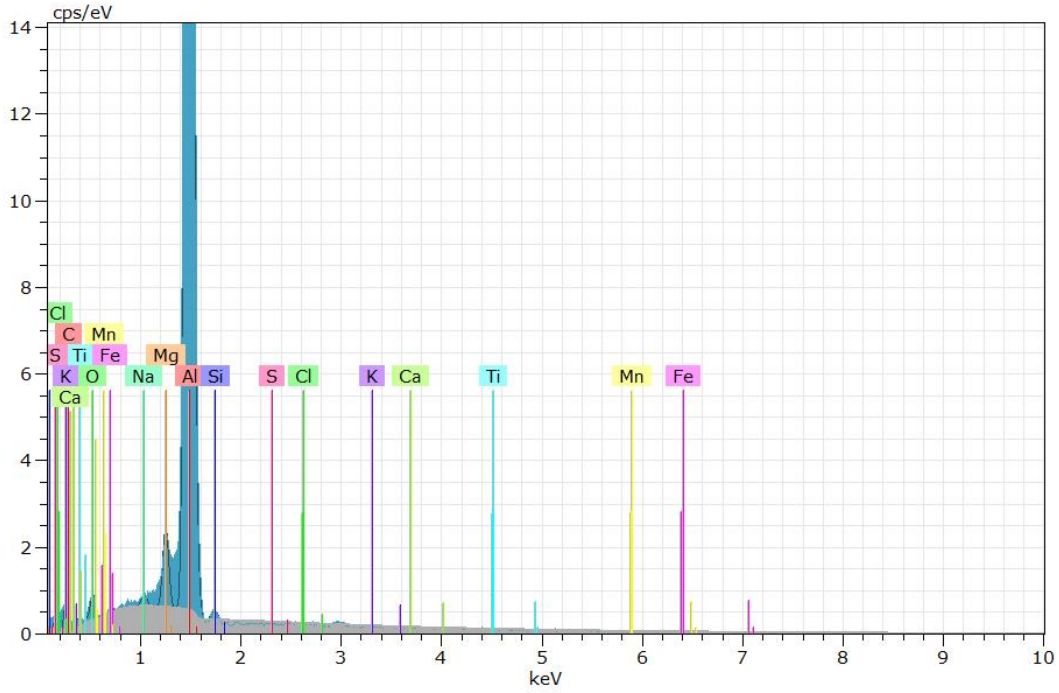

(c) Intensity spectrum of point 73

Figure D.24: Intensity spectrum of the points in figure D.23a

D.13 Water cooled not-stretched tensile specimen stored for 7 days fracture area 1

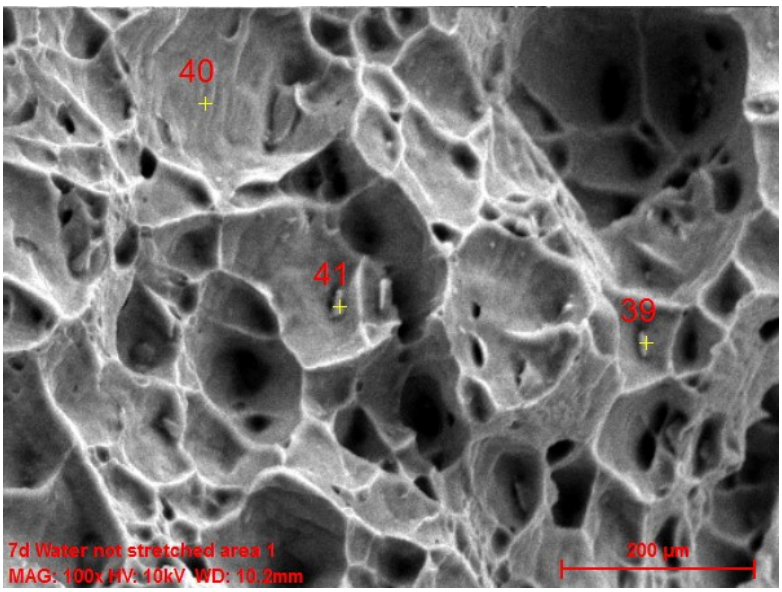

(a) SEM image of fracture area 1 in a not-stretched water cooled tensile specimens stored for 7 days at room temperature.

Element given in $[wt\%]$	Al	O	Mg	Ti	Fe	Mn	Si	K	S	Ca	Na	C	Cl
39	95.46	0.64	1.31	0	0.37	0.01	1.91	0	0	0.03	0.28	0	0
40	97.30	0.65	1.30	0.03	0	0	0.41	0.02	0.01	0.06	0.20	0	0.02
41	96.43	1.05	1.28	0.13	0	0	0.63	0	0	0.24	0.23	0	0

Figure D.25: SEM image of fracture area 1 in a not-stretched water cooled tensile specimen stored for 7 days at room temperature. Chemical analysis as nominative chemical composition of points in the SEM image is given in the table below, obtained by EDS.

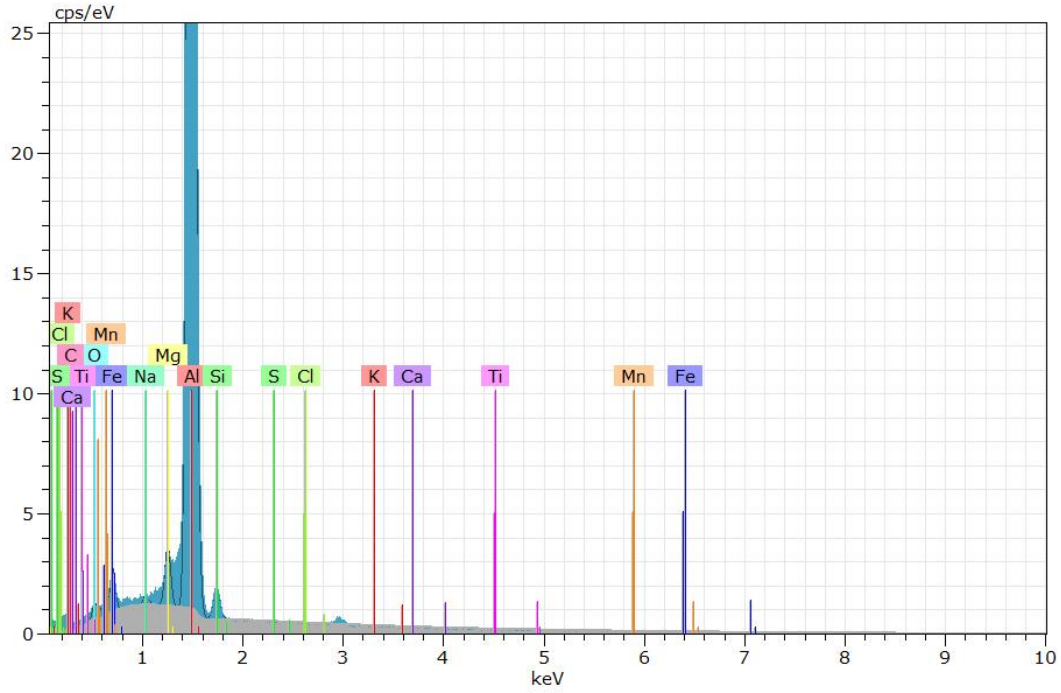

(a) Intensity spectrum of point 39

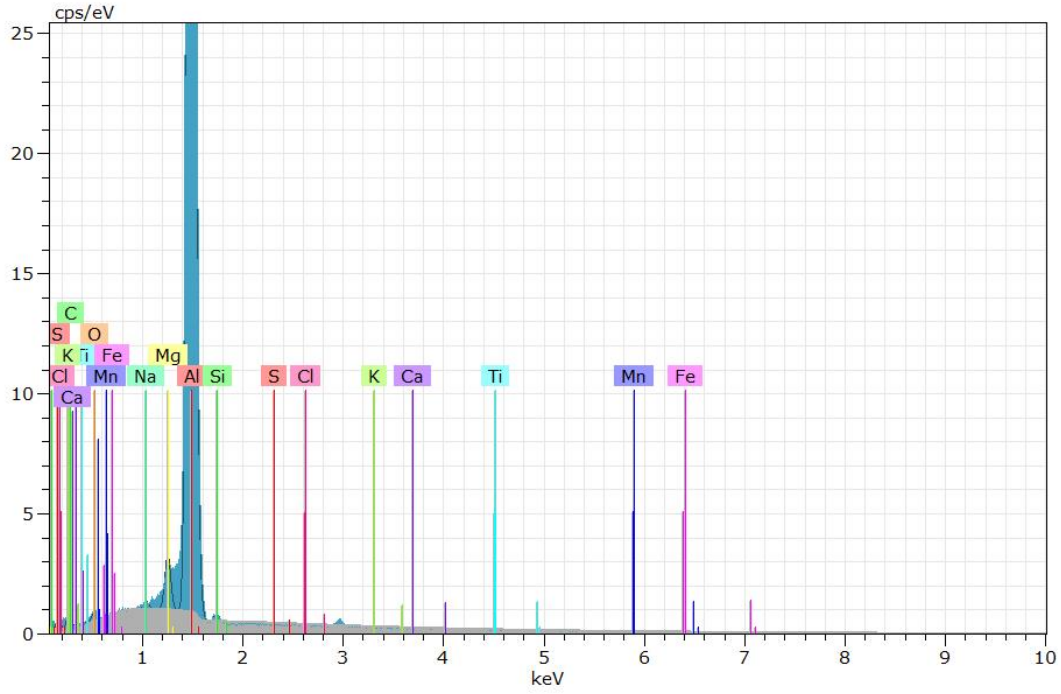

(b) Intensity spectrum of point 40

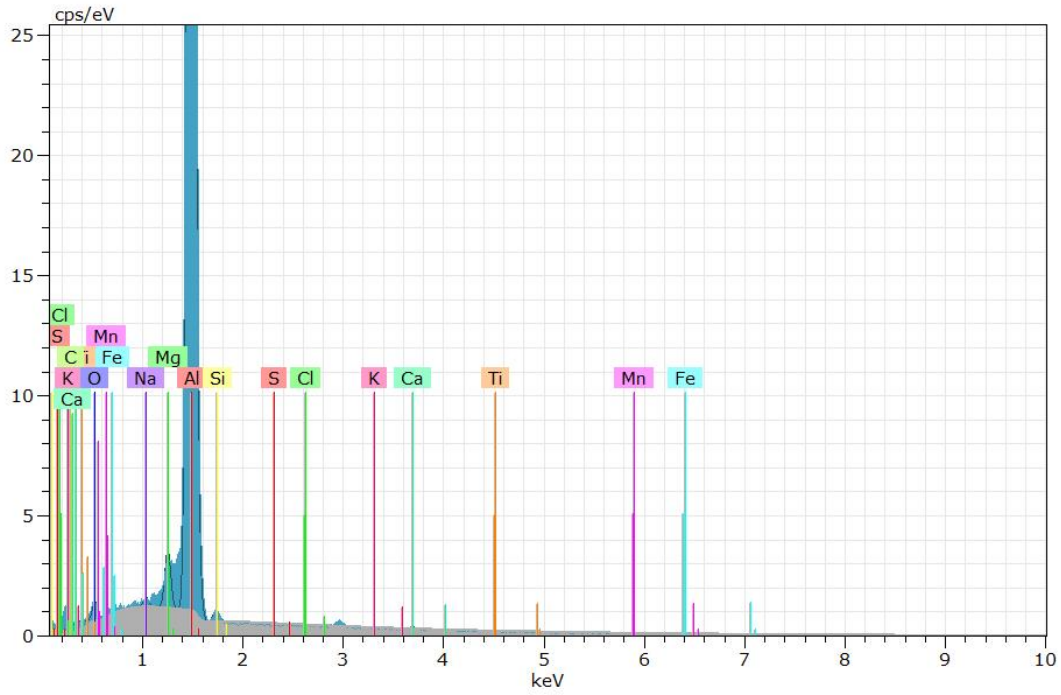

(c) Intensity spectrum of point 41

Figure D.26: Intensity spectrum of the points in figure D.25a

D.14 Water cooled not-stretched tensile specimen stored for 7 days fracture area 2

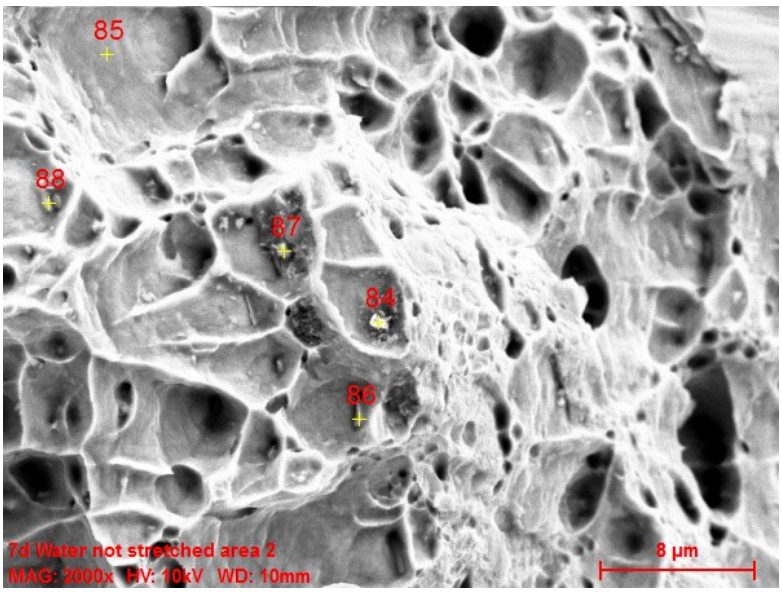

(a) SEM image of fracture area 2 in a not-stretched water cooled tensile specimens stored for 7 days at room temperature.

Element given in $[wt\%]$	Al	O	Mg	Ti	Fe	Mn	Si	K	S	Ca	Na	C	Cl
84	78.45	8.19	1.52	0	0.57	0.05	2.36	0.30	0.84	1.80	0.45	4.17	1.29
85	97.02	0.51	1.38	0.21	0	0	0.55	0.02	0.05	0	0.24	0	0.03
86	94.68	1.86	1.59	0.04	0.35	0	0.84	0.05	0.03	0.32	0.24	0	0.01
87	82.76	2.83	1.91	0	0	0	1.61	0.55	1.18	3.47	5.06	0.48	
88	94.77	1.42	1.50	0	0.27	0.26	1.39	0.08	0.02	0	0.27	0	0.01

Figure D.27: SEM image of fracture area 2 in a not-stretched water cooled tensile specimen stored for 7 days at room temperature. Chemical analysis as nominative chemical composition of points in the SEM image is given in the table below, obtained by EDS.

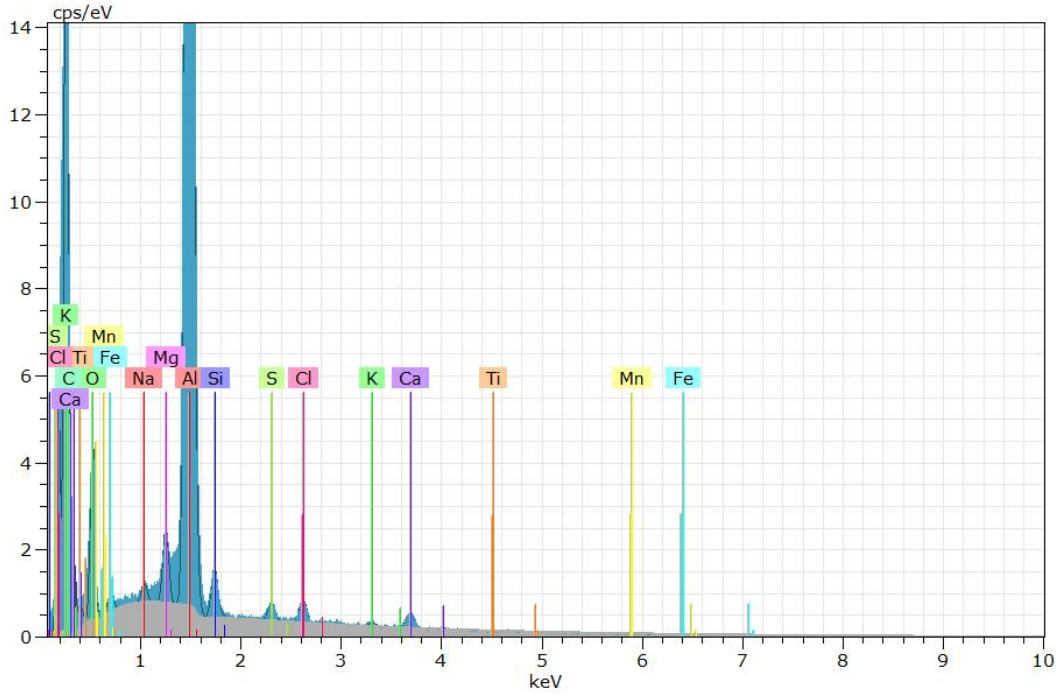

(a) Intensity spectrum of point 84

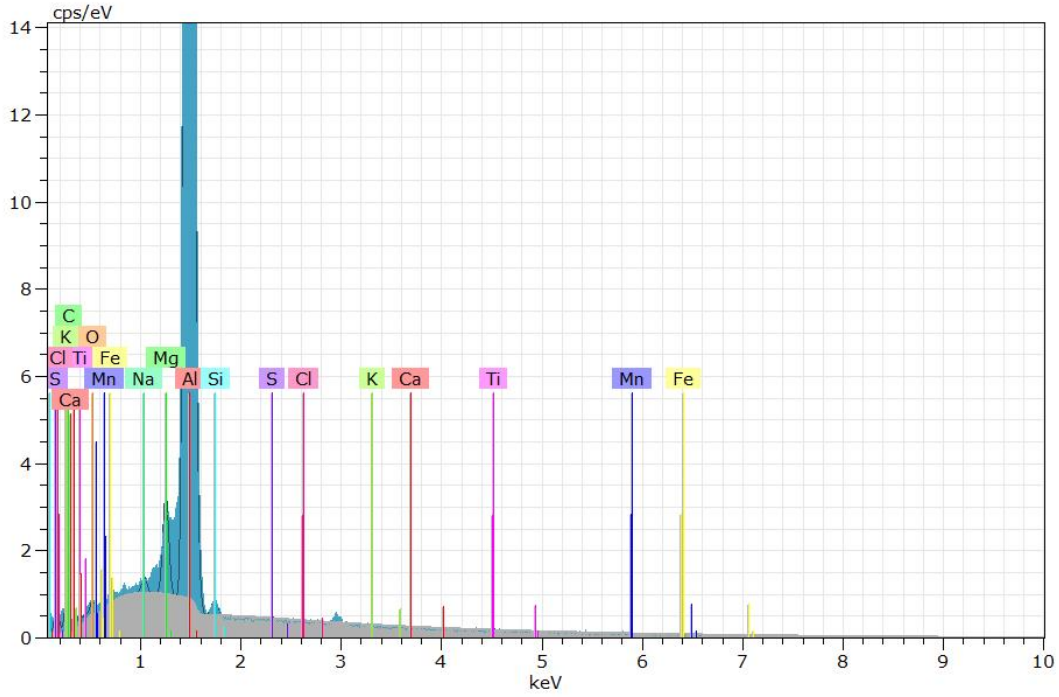

(b) Intensity spectrum of point 85

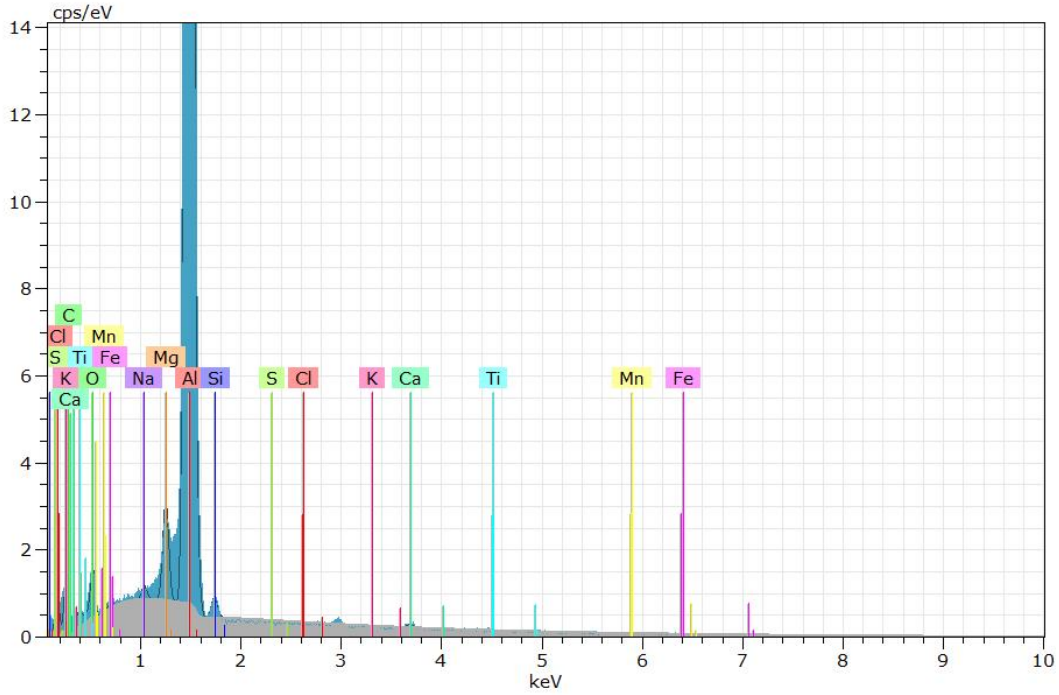

(c) Intensity spectrum of point 86

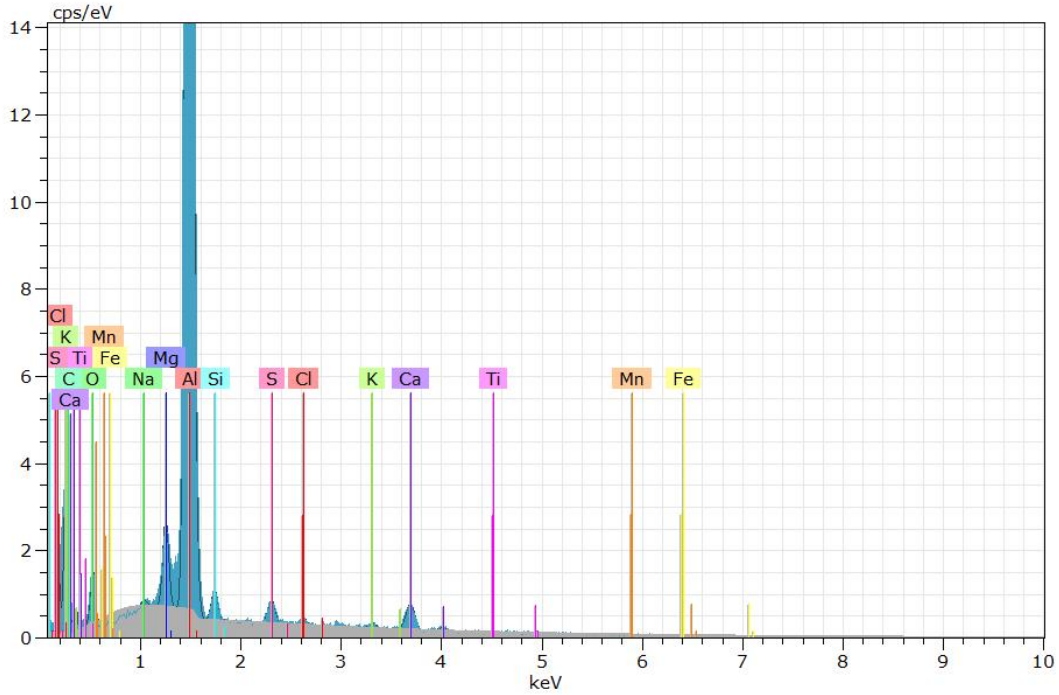

(d) Intensity spectrum of point 87

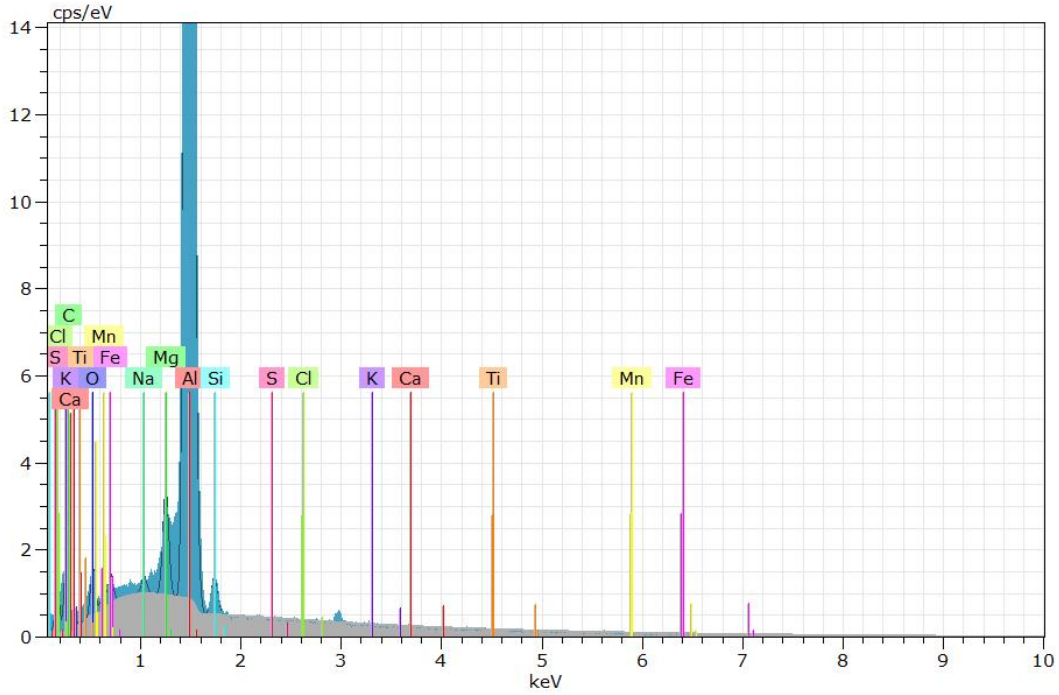

(e) Intensity spectrum of point 88

Figure D.28: Intensity spectrum of the points in figure D.27a

D.15 Water cooled not-stretched tensile specimen stored for 7 days fracture area 3

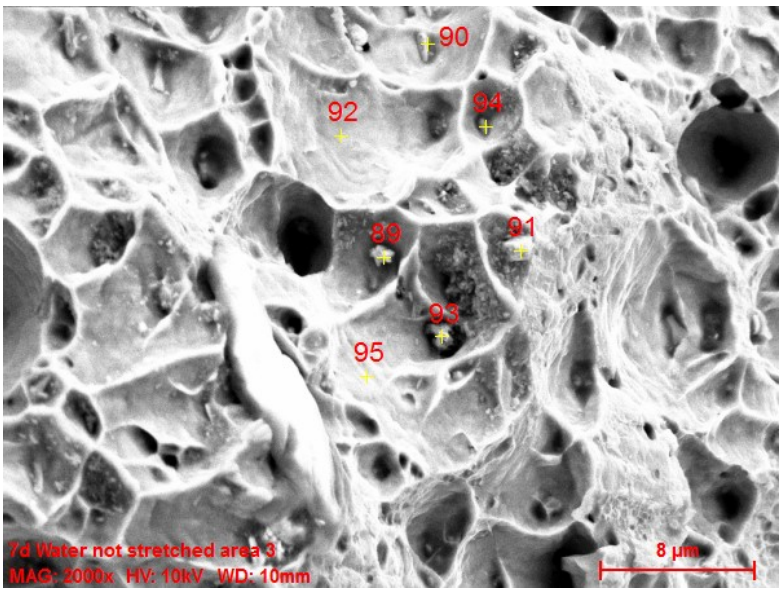

(a) SEM image of fracture area 3 in a not-stretched water cooled tensile specimens stored for 7 days at room temperature.

Element given in $[wt\%]$	Al	O	Mg	Ti	Fe	Mn	Si	K	S	Ca	Na	C	Cl
89	33.18	21.11	0.81	0	0	0	0.52	0.34	0.07	39.50	0.28	3.98	0.20
90	95.23	0.59	1.37	0	0	0.23	1.20	0	0.01	0	0.33	0	0.03
91	82.69	1.27	1.48	0	9.76	0.83	2.91	0.02	0.05	0.18	0.11	0.65	0.06
92	96.80	0.76	1.33	0	0	0	0.78	0	0.03	0.08	0.22	0	0
93	15.66	20.61	59.76	0.05	0	0	0.68	0.15	0.39	1.36	0.84	0.40	0.09
94	90.42	1.09	1.37	0.04	2.73	0.23	3.20	0.06	0.06	0.11	0.33	0.29	0.07
95	95.87	1.17	1.58	0.02	0	0.01	0.95	0	0.05	0.12	0.22	0	0.01

Figure D.29: SEM image of fracture area 3 in a not-stretched water cooled tensile specimen stored for 7 days at room temperature. Chemical analysis as nominative chemical composition of points in the SEM image is given in the table below, obtained by EDS.

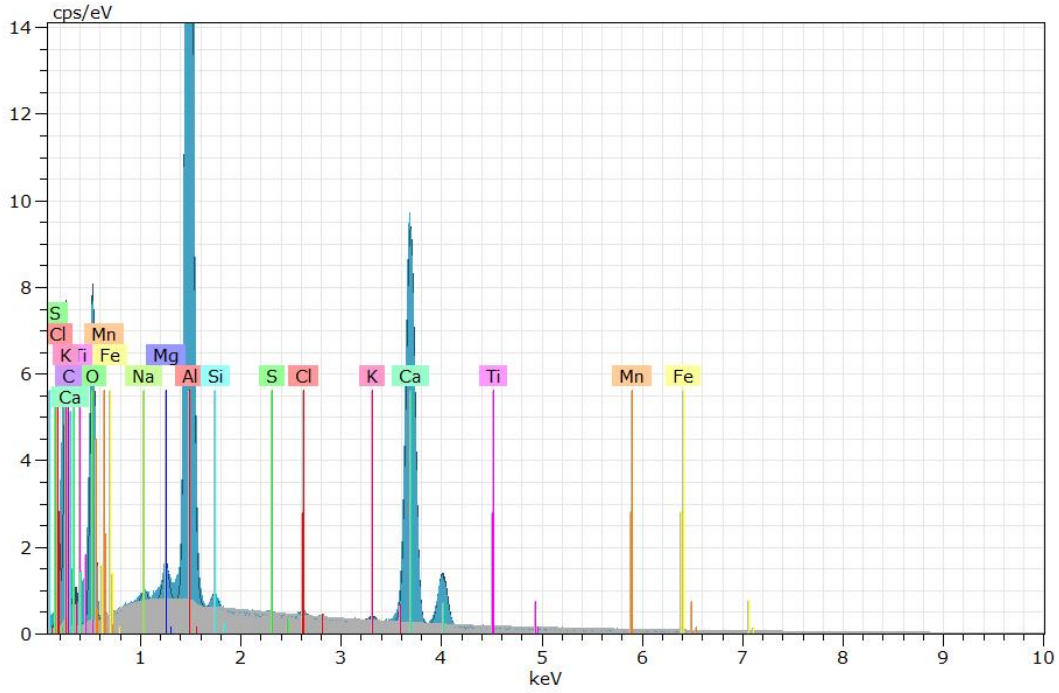

(a) Intensity spectrum of point 89

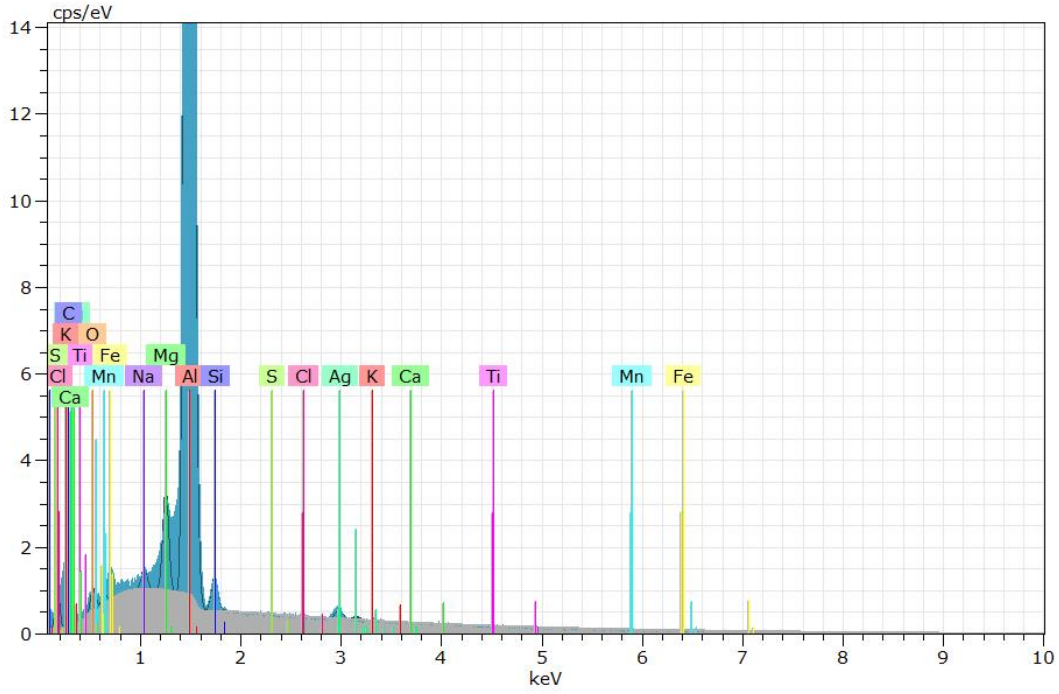

(b) Intensity spectrum of point 90

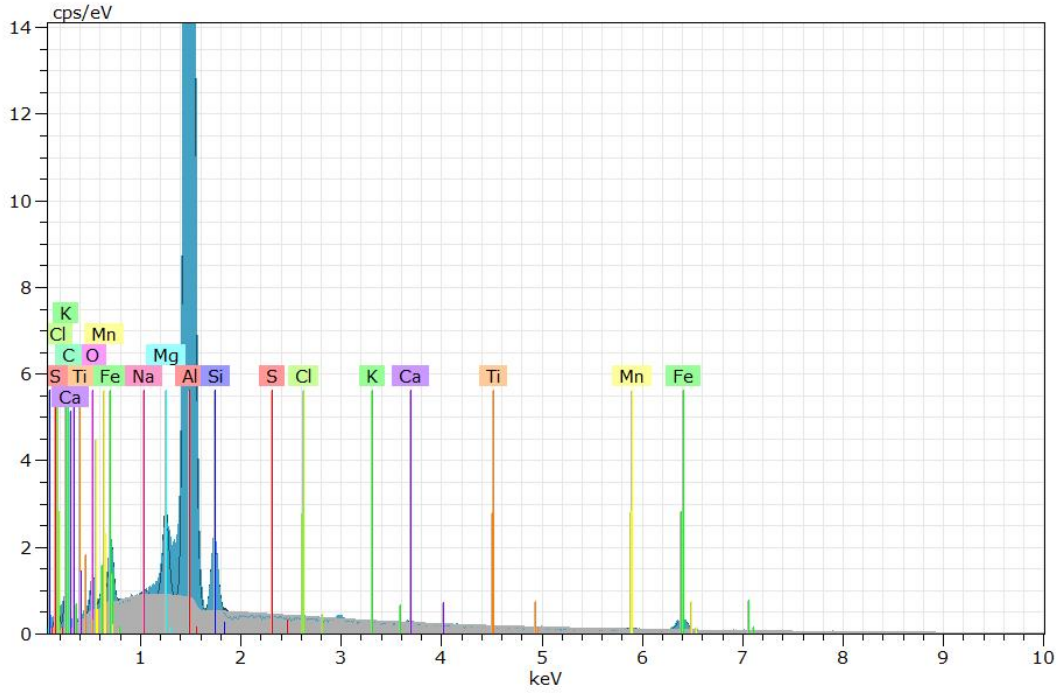

(c) Intensity spectrum of point 91

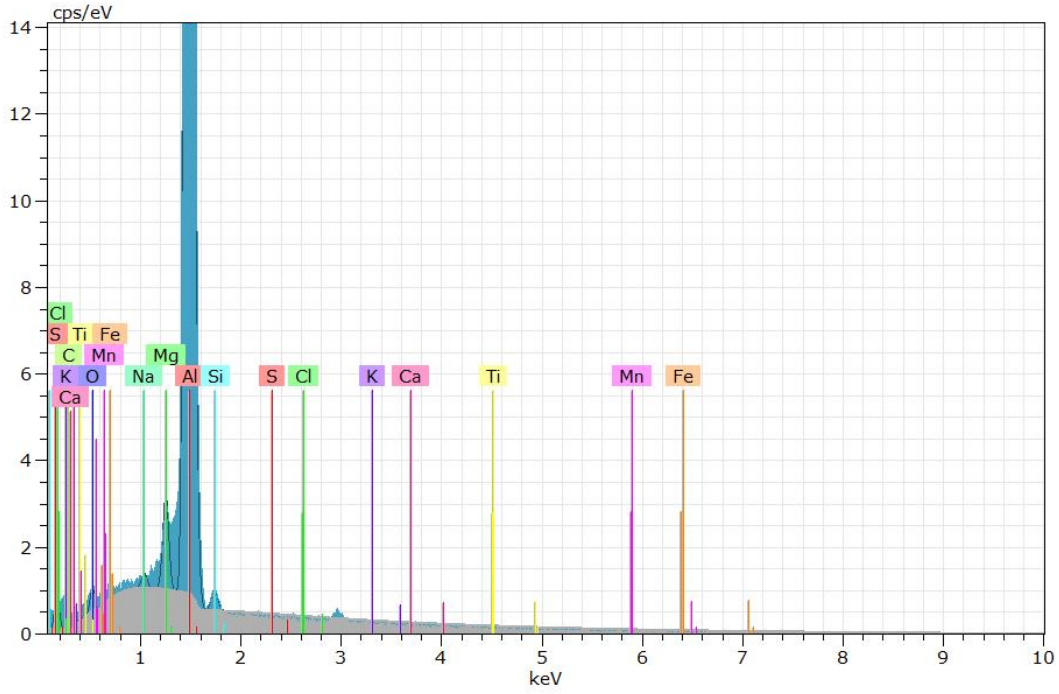

(d) Intensity spectrum of point 92

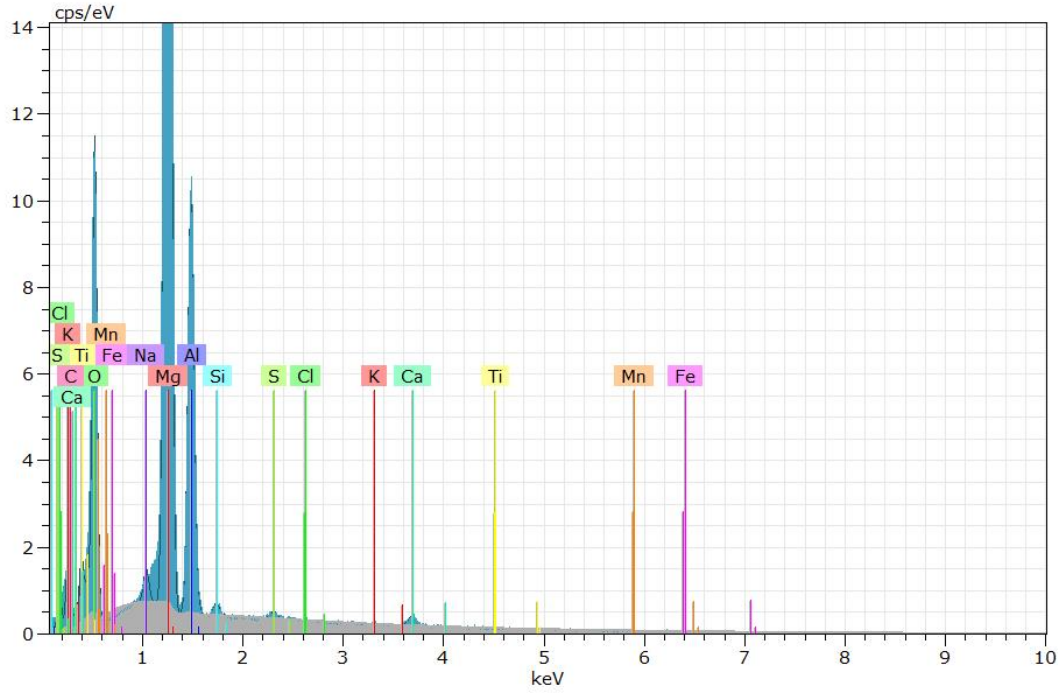

(e) Intensity spectrum of point 93

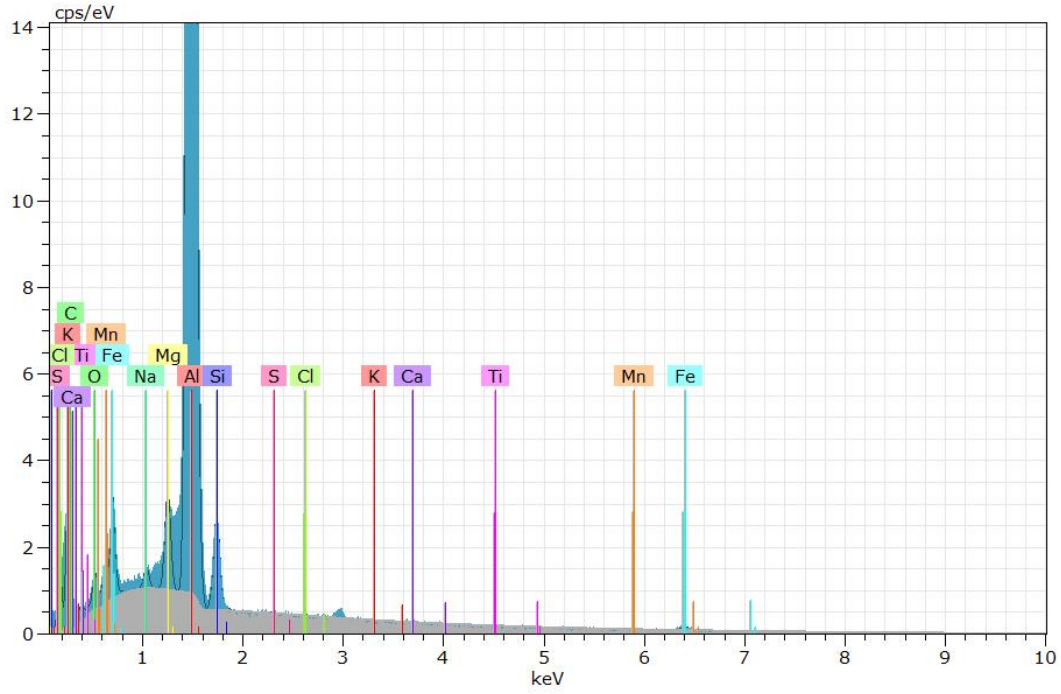

(f) Intensity spectrum of point 94

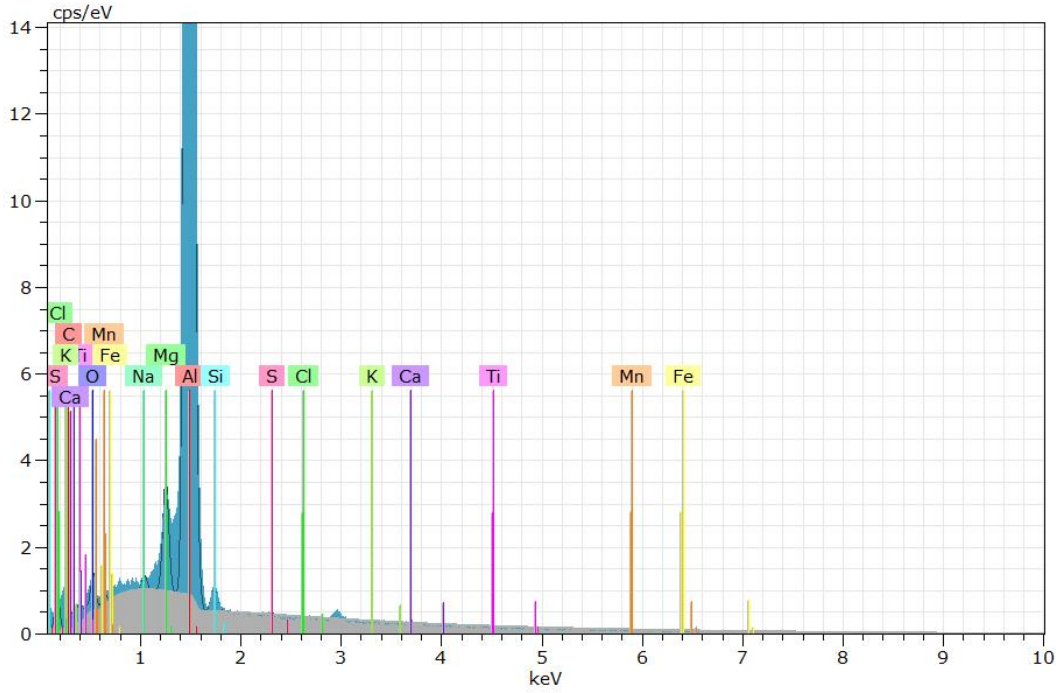

(g) Intensity spectrum of point 95

Figure D.30: Intensity spectrum of the points in figure D.29a

D.16 Water cooled pre stretched tensile specimen stored for 7 days fracture area 1

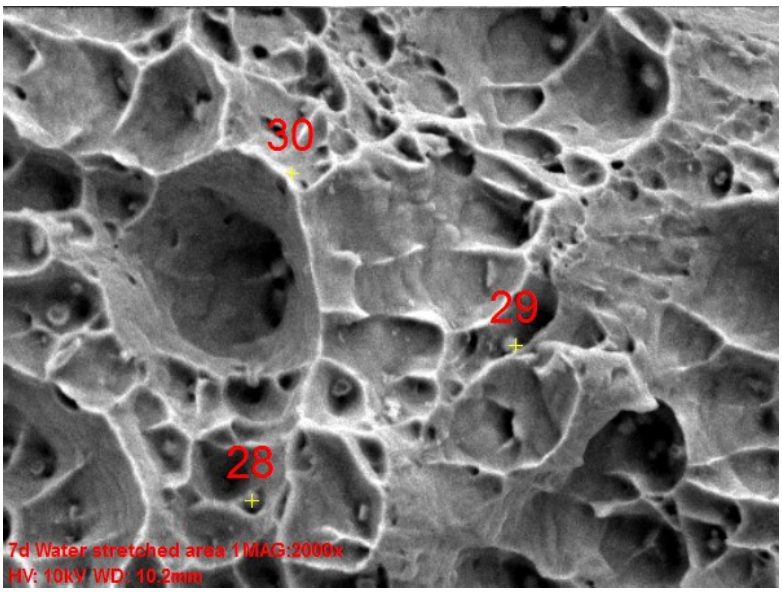

(a) SEM image of fracture area 1 in a pre stretched water cooled tensile specimens stored for 7 days at room temperature.

Element given in $[wt\%]$	Al	O	Mg	Ti	Fe	Mn	Si	K	S	Ca	Na	C	Cl
28	46.08	8.55	0.87	0	0	0.28	0.59	16.84	1.02	3.52	2.73	3.41	16.11
29	36.90	24.92	0.84	0.09	0	0.33	0.42	0.76	0.31	27.88	1.26	5.95	0.33
30	95.22	1.54	1.55	0	0.09	0.03	1.04	0	0.08	0.08	0.35	0	0.03

Figure D.31: SEM image of fracture area 1 in a pre stretched water cooled tensile specimen stored for 7 days at room temperature. Chemical analysis as nominative chemical composition of points in the SEM image is given in the table below, obtained by EDS.

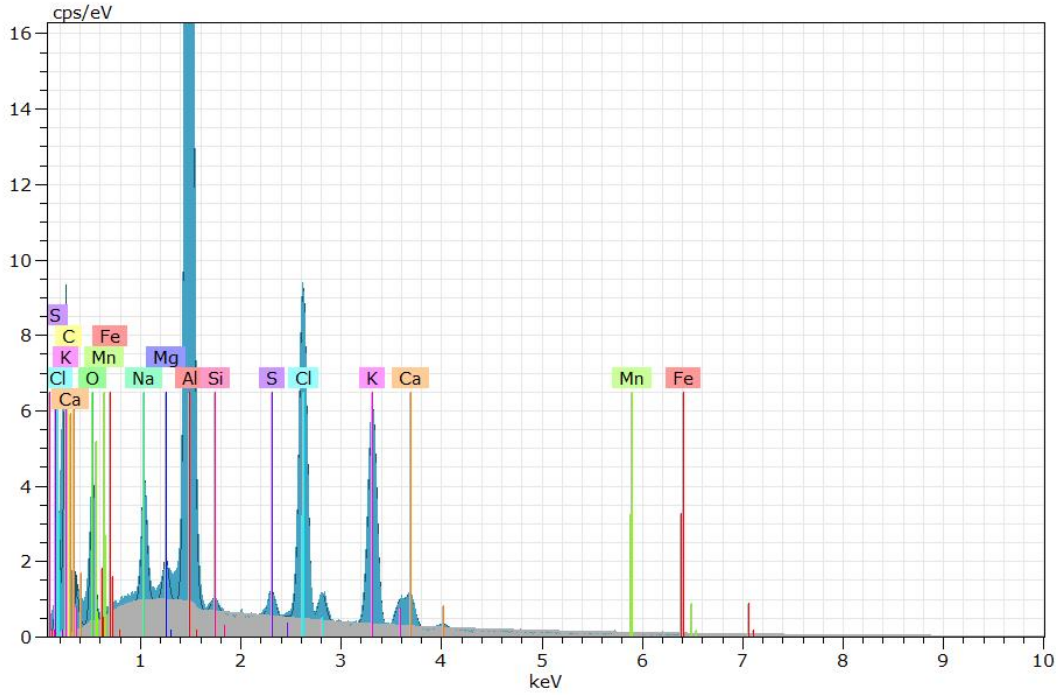

(a) Intensity spectrum of point 28

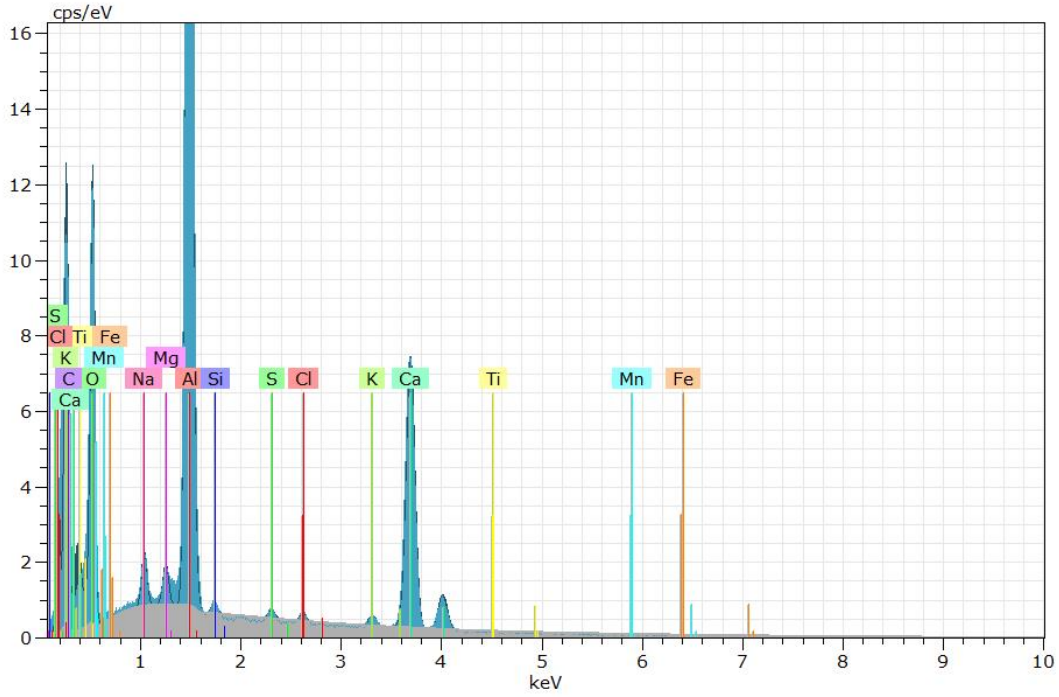

(b) Intensity spectrum of point 29

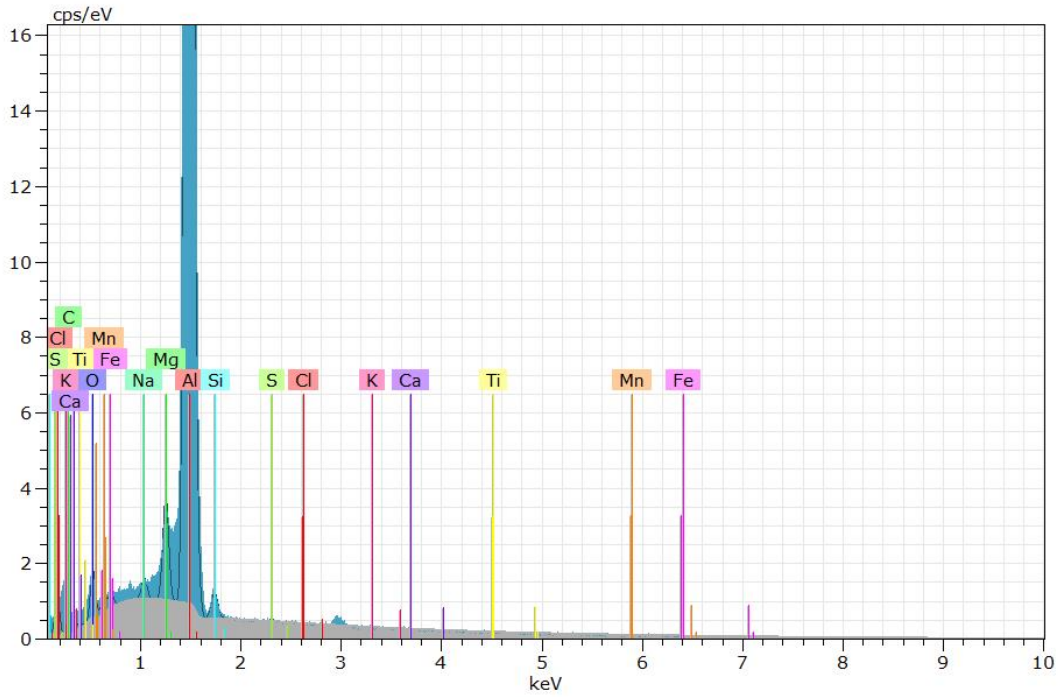

(c) Intensity spectrum of point 30

Figure D.32: Intensity spectrum of the points in figure D.31a